

# **Experimental Investigation of Hydrogen Production from Ammonia Decomposition**

by

**Jonathan Leo Nieminen**

A Thesis Submitted in Partial Fulfillment  
of the Requirements for the Degree of

Master of Applied Science (M.A.Sc)

in

The Faculty of Engineering and Applied Science

Program: Mechanical Engineering

University of Ontario Institute of Technology

August 2011

© Jonathan Leo Nieminen, 2011



## ABSTRACT

This thesis examines the production of hydrogen from ammonia in a continuous flow, packed bed membrane reactor. The experimental study examines the effects of operating temperature, pressure, and residence time on hydrogen production rate, energy and exergy ratios for the reaction, energy and exergy efficiencies of the overall system, ammonia conversion efficiency, transient ammonia concentration, and ammonia decomposition rate. With the exception of transient ammonia conversion, all of the above underwent increases with respect to operating temperature, pressure and residence time. The increases in operating temperature led to increase catalytic activity and further favouring of the reaction thermodynamics due to the Gibb's free energy tending towards zero or increasing negatively. The increases in operating pressure resulted in increased residence times and trans – membrane pressure differences which caused increased hydrogen flux.

The best results were obtained at 20 bar, 500°C and with a residence time of approximately four seconds. The maximum hydrogen production was approximately 287 mL/min. This lightly undershoots the stoichiometric production rate of approximately 300 mL/min. The maximum energy and exergy ratios for the reaction were 6.77:1 and 1.08:1, respectively. Also, the maximum energy and exergy efficiencies of the overall system were 16.9% and 20.3%, respectively. The maximum ammonia conversion efficiency and minimum ammonia concentration was found to be approximately 95.64% and 4.2%, respectively. The system took approximately 50.0 minutes to reach steady state in this particular scenario.

On the results drawn from this experimental work, some technical recommendations to further improve the system's performance and reliability were made. Also, a potential design for the rail industry was proposed and lightly explained based on the results of this thesis work. Overall, the results of this experimental work were insightful and will be useful as an initial benchmark for future work in the area hydrogen production from ammonia decomposition at UOIT.

*Keywords:* Hydrogen production, ammonia, membrane reactor, heat transfer, packed bed, catalytic decomposition, chemical reaction

# Acknowledgements

I wish to thank my supervisor, *Dr. Ibrahim Dincer* for the guidance and advice given over the duration of the production of this thesis work. Also, I wish to thank *Dr. Calin Zamfirescu* for all his help during the production of this thesis work. Furthermore, I am appreciative of the opportunities to work on this challenging research project in order to contribute to the ever expanding pool of knowledge in the area of sustainable energy research.

Secondly, I wish to thank *Dr. Robert Buxbaum* of REB Research & Consulting for providing our group with a reactor and a catalyst to conduct experiments with. Also, the accommodation of the Clean Energy Research Laboratory (CERL) at UOIT is gratefully acknowledged.

Thirdly, I wish to thank the Office of Research Services at UOIT for all their help. Finally, financial support for this project was provided by the Ontario Partnership for Innovation and Commercialization (OPIC) and is gratefully acknowledged.

**August 2011**

**Jonathan Leo Nieminen**

# Table of Contents

List of Tables.....	viii
List of Figures.....	ix
Nomenclature.....	xiii
<b>1 Introduction.....</b>	<b>1</b>
1.1 The “Hydrogen Economy”.....	1
1.2 Overall Plan of Research .....	2
1.3 Motivation and Objectives of Thesis Work.....	4
<b>2 Literature Review.....</b>	<b>5</b>
2.1 Ammonia as a Hydrogen Carrier .....	5
2.2 Chemical Reactor Modeling and Kinetic Considerations .....	9
2.2.1 Comparative Overview of Chemical Reactor Models.....	9
2.2.2 Overview of Ammonia Decomposition Kinetics.....	14
2.3 Heat and Flow Considerations in Packed Beds .....	17
2.4 Palladium as a Hydrogen Selective Membrane .....	21
<b>3 Background Information.....</b>	<b>28</b>
3.1 Current Hydrogen Production Systems from Ammonia Decomposition.....	28
3.1.1 The Micro-Reforming System with Micro-Combustor.....	28
3.1.2 The CMR fed by NH <sub>3</sub> Plant Purge Gases... ..	30
3.1.3 The NH <sub>3</sub> Cracker for H <sub>2</sub> Production .....	32
3.2 Kinetic Models of Ammonia Decomposition.....	34
3.2.1 Power Rate Law Model.....	34
3.2.2 Model of Tymken - Pyzhev.....	34

3.2.3	Comparison of SMR, CH <sub>3</sub> OH, and NH <sub>3</sub> Reactions from First Principles.....	35
3.3	Modeling the Equilibrium Shift Associated with Hydrogen Removal.....	47
3.3.1	Comparison of SMR, CH <sub>3</sub> OH, and NH <sub>3</sub> Reactions from First Principles.....	47
3.4	Characteristics of Solid Catalysts .....	50
<b>4</b>	<b>Experimental Works.....</b>	<b>53</b>
4.1	Design of the Membrane Reactor System for Hydrogen Production.....	53
4.1.1	Charging the Experimental Unit with NH <sub>3</sub> .....	60
4.2	Statistical Design of the NH <sub>3</sub> Decomposition Experiments .....	62
4.3	Experimental Method for Conducting the NH <sub>3</sub> Decomposition Experiments.....	64
4.4	Method for Calculating Transient NH <sub>3</sub> Concentration in the Raffinate Steam.....	64
<b>5</b>	<b>Results and Discussion .....</b>	<b>66</b>
5.1	Results for Hydrogen Production .....	66
5.2	Results for Overall System Performance .....	70
5.3	Results for NH <sub>3</sub> Conversion Efficiency .....	81
5.4	Results for Transient NH <sub>3</sub> Concentration in the Raffinate Stream .....	85
5.5	Results for Transient NH <sub>3</sub> Decomposition Rates.....	89
5.6	Commentary on Transient Behaviour.....	93
5.7	Results for Catalyst Surface Morphology .....	94
5.8	Results of Uncertainty Analysis.....	98
5.9	Commentary on Environmental Impact.....	99
5.10	Potential Applications .....	100
5.11	Potential Design.....	100

<b>6</b>	<b>Conclusions and Recommendations .....</b>	<b>103</b>
6.1	Conclusions.....	103
6.2	Recommendations.....	105
	<b>References .....</b>	<b>106</b>
	<b>Appendices.....</b>	<b>110</b>
	Appendix A.....	111
	Appendix B.....	117
	Appendix C.....	131

# List of Tables

Table 2.1: Applicability of various indirect H <sub>2</sub> storage solutions.....	6
Table 2.2: Comparison of NH <sub>3</sub> decomposition and CH <sub>3</sub> OH reforming reactions.....	7
Table 2.3: Relative permeability of palladium and its alloys.....	22
Table 3.1: Experimental systems reviewed in this thesis work.....	28
Table 3.2: Various chemical reactions for thermal H <sub>2</sub> production .....	36
Table 3.3: Total number of moles (n <sub>tot</sub> ) for the membrane reactor case.....	38
Table 3.4: Sample activation energies and pre – exponential factors.....	39
Table 3.5: Sample Gibb’s free energies for three chemical reactions .....	42
Table 3.6: Maximum H <sub>2</sub> recovery and trans – membrane ΔP for NH <sub>3</sub> decomposition reaction..	45
Table 3.7: Maximum H <sub>2</sub> recovery and trans – membrane ΔP for CH <sub>3</sub> OH reforming reaction....	45
Table 3.8: Maximum H <sub>2</sub> recovery and trans – membrane ΔP for SMR reaction.....	45
Table 4.1: Experimental conditions investigated.....	63
Table 4.2: Experimental run table.....	63

# List of Figures

Figure 3.1: Process diagram of a micro – reforming system .....	29
Figure 3.2: Diagram of shell and tube CMR.....	31
Figure 3.3: Schematic of ammonia cracker system .....	33
Figure 3.4: Batch reactor for an arbitrary chemical reaction .....	37
Figure 3.5: Membrane reactor for an arbitrary chemical reaction.....	37
Figure 3.6: NH <sub>3</sub> decomposition rate vs. H <sub>2</sub> extraction ratio at 20.0 bar.....	39
Figure 3.7: CH <sub>3</sub> OH reforming rate vs. H <sub>2</sub> extraction ratio at 20.0 bar.....	40
Figure 3.8: SMR reaction rate vs. H <sub>2</sub> extraction ratio at 20.0 bar.....	40
Figure 3.9: Trans – membrane $\Delta P$ vs. H <sub>2</sub> extraction ratio for NH <sub>3</sub> decomposition reaction at 20.0 bar.....	43
Figure 3.10: Trans – membrane $\Delta P$ vs. H <sub>2</sub> extraction ratio for CH <sub>3</sub> OH reforming reaction at 20.0 bar.....	44
Figure 3.11: Trans – membrane $\Delta P$ vs. H <sub>2</sub> extraction ratio for SMR reaction at 20.0 bar.....	44
Figure 3.12: Equilibrium concentration vs. H <sub>2</sub> extraction ratio for NH <sub>3</sub> decomposition reaction .....	48
Figure 3.13: Equilibrium concentration vs. H <sub>2</sub> extraction ratio for CH <sub>3</sub> OH reforming reaction...49	49
Figure 3.14: Equilibrium concentration vs. H <sub>2</sub> extraction ratio for SMR reaction.....	49
Figure 3.15: NH <sub>3</sub> decomposition reaction on a Ni <sub>2</sub> O <sub>3</sub> catalyst surface.....	52
Figure 4.1: Process diagram for experimental setup for H <sub>2</sub> production from NH <sub>3</sub> decomposition .....	55

Figure 4.2: Voltage regulator circuit to step 14.0 V DC down to 5.0 V DC.....	56
Figure 4.3: Electrical diagram of furnace control system .....	57
Figure 4.4: Frontal view of main experimental setup.....	58
Figure 4.5: Left hand side view of main experimental setup .....	59
Figure 4.6: Right hand side view of main experimental setup .....	60
Figure 5.1: H <sub>2</sub> production vs. time at 400°C, 5.0 bar and three residence times.....	66
Figure 5.2: H <sub>2</sub> production vs. time at 500°C, 5.0 bar and three residence times.....	67
Figure 5.3: H <sub>2</sub> production vs. time at 400°C, 10.0 bar and two residence times.....	67
Figure 5.4: H <sub>2</sub> production vs. time at 500°C, 10.0 bar and two residence times.....	68
Figure 5.5: H <sub>2</sub> production vs. time at 400°C, 20.0 bar and two residence times.....	68
Figure 5.6: H <sub>2</sub> production vs. time at 500°C, 20.0 bar and two residence times.....	69
Figure 5.7: Energy ratio vs. time for 400°C, 5.0 bar and three residence times.....	72
Figure 5.8: Energy ratio vs. time for 500°C, 5.0 bar and three residence times.....	73
Figure 5.9: Energy ratio vs. time for 400°C, 10.0 bar and two residence times.....	73
Figure 5.10: Energy ratio vs. time for 500°C, 10.0 bar and two residence times.....	74
Figure 5.11: Energy ratio vs. time for 500°C, 20.0 bar and two residence times.....	74
Figure 5.12: Energy ratio vs. time for 500°C, 20.0 bar and two residence times.....	75
Figure 5.13: Exergy ratio vs. time for 400°C, 5.0 bar and three residence times.....	75
Figure 5.14: Exergy ratio vs. time for 500°C, 5.0 bar and three residence times.....	76
Figure 5.15: Exergy ratio vs. time for 400°C, 10.0 bar and two residence times.....	76
Figure 5.16: Exergy ratio vs. time for 500°C, 10.0 bar and two residence times.....	77

Figure 5.17: Exergy ratio vs. time for 400°C, 20.0 bar and two residence times.....	77
Figure 5.18: Exergy ratio vs. time for 500°C, 20.0 bar and two residence times.....	78
Figure 5.19: Maximum steady state energy and exergy efficiencies for 10.0 bar, 400.0°C, 500.0°C and two residence times.....	78
Figure 5.20: Maximum steady state energy and exergy efficiencies for 20.0 bar, 400.0°C, 500.0°C and two residence times.....	79
Figure 5.21: NH <sub>3</sub> concentration vs. time for 400°C, 5.0 bar and three residence times.....	81
Figure 5.22: NH <sub>3</sub> concentration vs. time for 500°C, 5.0 bar and three residence times.....	82
Figure 5.23: NH <sub>3</sub> concentration vs. time for 400°C, 10.0 bar and two residence times.....	82
Figure 5.24: NH <sub>3</sub> concentration vs. time for 500°C, 10.0 bar and two residence times.....	83
Figure 5.25: NH <sub>3</sub> concentration vs. time for 400°C, 20.0 bar and two residence times.....	83
Figure 5.26: NH <sub>3</sub> concentration vs. time for 500°C, 20.0 bar and two residence times.....	84
Figure 5.27: NH <sub>3</sub> conversion vs. time for 400°C and 5.0 bar for three residence times.....	85
Figure 5.28: NH <sub>3</sub> conversion vs. time for 500°C and 5.0 bar for three residence times.....	86
Figure 5.29: NH <sub>3</sub> conversion vs. time for 400°C and 10.0 bar for two residence times.....	86
Figure 5.30: NH <sub>3</sub> conversion vs. time for 500°C and 10.0 bar for two residence times.....	87
Figure 5.31: NH <sub>3</sub> conversion vs. time for 400°C and 20.0 bar for two residence times.....	87
Figure 5.32: NH <sub>3</sub> conversion vs. time for 500°C and 20.0 bar for two residence times.....	88
Figure 5.33: NH <sub>3</sub> decomposition rate vs. time for 400°C and 5.0 bar for three residence times..	89
Figure 5.34: NH <sub>3</sub> decomposition rate vs. time for 500°C and 5.0 bar for three residence times..	90
Figure 5.35: NH <sub>3</sub> decomposition rate vs. time for 400°C and 10.0 bar for two residence times..	90
Figure 5.36: NH <sub>3</sub> decomposition rate vs. time for 500°C and 10.0 bar for two residence times...	91

Figure 5.37: NH <sub>3</sub> decomposition rate vs. time for 400°C and 20.0 bar for two residence times...	91
Figure 5.38: NH <sub>3</sub> decomposition rate vs. time for 500°C and 20.0 bar for two residence times...	92
Figure 5.39: The effect of residence time, pressure and temperature on threshold time.....	93
Figure 5.40: Magnified SEM image of an unexposed Ni <sub>2</sub> O <sub>3</sub> catalyst particle (50 μm).....	94
Figure 5.41: Magnified SEM image of an unexposed Ni <sub>2</sub> O <sub>3</sub> catalyst particle (10μm).....	95
Figure 5.42: Magnified SEM image of an unexposed Ni <sub>2</sub> O <sub>3</sub> catalyst particle (200 nm).....	95
Figure 5.43: Magnified SEM image of an exposed Ni <sub>2</sub> O <sub>3</sub> catalyst particle (50 μm).....	96
Figure 5.44: Magnified SEM image of an exposed Ni <sub>2</sub> O <sub>3</sub> catalyst particle (10 μm).....	97
Figure 5.45: Magnified SEM image of an exposed Ni <sub>2</sub> O <sub>3</sub> catalyst particle (200 nm).....	97
Figure 5.46: Potential design of an H <sub>2</sub> production system via NH <sub>3</sub> decomposition for a rail application.....	101

# Nomenclature

$C_i$	Concentration of the $i$ th component (%)
$E_a$	Activation energy (kJ/mol)
$F(t)$	Function defined in Eq. 4.2
$G$	Gibb's free energy, kJ/kg
$g_{H_2}$	gram of hydrogen
$H$	Enthalpy, kJ/kg
$K_{eq}$	Equilibrium constant, ( - )
$k^+$	Forward reaction rate constant, ( - )
$k^-$	Reverse reaction rate constant, ( - )
$k_o$	Pre-exponential factor
$LHV_{H_2}$	Lower heating value of hydrogen, kJ/kg
$\dot{m}_{H_2}$	Mass flow rate of hydrogen, kg/s
$n_i$	Number of moles of the $i$ th component (mol)
$n_{tot}$	Total number of moles
$P$	Pressure, kPa
$P_i$	Partial pressure of the $i$ th component (kPa)
$P_o$	Reference pressure, kPa
$P_{op}$	Operating pressure, kPa
$P_{tot}$	Function defined in Eq. 4.1

pH	Power of hydrogen
$\dot{Q}_{cool}$	Cooling rate, W
$\dot{Q}_{in}$	Heat input rate, W
R	Rydberg gas constant, kJ/molK
$r_{fwd}$	Forward reaction rate, mol/s
$r_{net}$	Net reaction rate, mol/s
$r_{rev}$	Reverse reaction rate, mol/s
S	Entropy, kJ/kgK
$t_{fill}$	Filling time required for NH <sub>3</sub> tank, s
$t_{res}$	Residence time, s
$w_i$	Uncertainty limits
$W_i$	Magnitude of uncertainty
[X]	Molar concentration or partial pressure of species “X” ( $n_i/n_{tot}$ ) or ( $P_i/P_{tot}$ )

### **Greek Letters**

$\epsilon$	Function defined in Eq. 4.5
$\epsilon_{sys}$	Function defined in Eq. 5.1
$\epsilon_{steady,max}$	Function defined in Eq. 5.6
$\Delta H_{evap.}$	Heat of vapourization, kJ/kg
$\Delta H_{rxn}$	Enthalpy of reaction, kJ/mol
$\eta_{ACFC}$	Efficiency of an acid fuel cell
$\eta_{AFC}$	Efficiency of an alkaline fuel cell

$\eta_{\text{steady,max}}$  Function defined in Eq. 5.5

$\Psi_{\text{steady,max}}$  Function defined in Eq. 5.2

### **Acronyms**

CNT Carbon nano-tube

CO<sub>x</sub> Carbon emissions

DoE Department of Energy

EES Engineering equation solver

FCC Face centered cubic

GC-TCD Gas chromatograph – thermal conductivity detector

IGCC Integrated gasification combined cycle

ICE Internal combustion engine

MCR Multifunctional catalytic reactor

Mto<sub>e</sub> Mega-ton-electrical

Pd-PSS Palladium coated porous stainless steel

SGR Sweep gas ratio

SR Stiffness ratio

# Chapter 1: Introduction

## 1.1 The “Hydrogen Economy”

According to “Key World Energy Statistics” published by the International Energy Agency [1], the world consumed 5646.8 Mto<sub>e</sub> of fossil fuels in 2008. This is an increase of roughly 160% from 1973 and shows an increasing trend for the future. When coupled with increases of 211% and 298% in oil consumption by the transportation industry and fossil fuels for electricity generation there is a 188% increase in CO<sub>2</sub> emissions between 1973 and 2008, respectively. Due to the aforementioned, the current zeitgeist is one favouring the development of sustainable and renewable energy technologies such as wind, solar, geothermal, biomass, and hydrogen. Hydrogen is a promising option because unlike its carbon based counterparts, a hydrogen based economy can reduce harmful greenhouse gas emissions, improve urban air quality, and provide a secure energy supply [2]. According to Haseli [3], the worldwide hydrogen market was valued at over 282 billion dollars per year in 2008 and is projected to reach several trillion per year by 2020. Analogous to electricity, hydrogen is considered to be an energy medium. Therefore it needs to be produced via removing it from compounds which contain it. On those caveats, Dincer [4] gives a list of some hydrogen production technologies and some technical recommendations for each one. Some technologies mentioned were: hydrocarbon gasification, steam-methane reforming, photovoltaic (PV) solar, electrolysis, off – gas cleanup, and thermochemical processes. Given the plethora of technologies available for hydrogen production coupled with the fact that countless compounds contain hydrogen in their makeup, the question that remains is: “What is the ideal reactant that an efficient and economical hydrogen production system can operate?” With that being said, there are a couple design requirements that must be mentioned at this point:

- The ideal reactant should have a large mass percentage of hydrogen to maximize the hydrogen produced per unit mass of reactant supplied.
- The ideal reactant should have a low enthalpy of reaction to further minimize the energy requirements of the system.
- The selected reactant should be sustainable and clean to help minimize CO<sub>2</sub> emissions as much as possible.

- Finally, the ideal reactant should be relatively cheap, plentiful, and easy to distribute and store.

In light of what was previously mentioned, ammonia ( $\text{NH}_3$ ) has been identified decomposition as a potentially favourable path of development and is mentioned by several researchers such as Zamfirescu et al. [5], Christensen et al. [6], and Metkemeijer et al. [7] is the path of an ammonia mediated hydrogen economy. The authors above have written about the problems associated with hydrogen transportation, handling, and storage. The consensus is that the use of ammonia as an efficient hydrogen carrier is a potential solution to the problems mentioned above. Despite its toxicity, the use of ammonia as a hydrogen carrier has several advantages; from both thermodynamic and economic perspectives. Ammonia is plentiful due to its long use as a fertilizer coupled with the development of associated supporting industries. Ammonia could be said to be renewable provided the ammonia is synthesized from agricultural wastes and not from previously produced hydrogen. Also, ammonia is easily stored as a liquid and there is an existing transportation and storage infrastructure. Due to the above and other reasons mentioned in the body of this thesis work, the thermal decomposition of ammonia for the thermochemical production of hydrogen is the focus of this thesis work.

## **1.2 Overall Plan of Research**

In this section, a lightly detailed research plan is presented to clearly and concisely illustrate the layout of this thesis work.

Chapter 2 is a comprehensive literature review that covers relevant aspects of a membrane reactor for the thermal decomposition of ammonia for hydrogen production. Aspects such as the rationale behind choosing ammonia as a hydrogen carrier, the benefits and drawbacks of different chemical reactor systems, kinetic models associated with catalytic decomposition of ammonia, heat transfer in packed beds, and the unique characteristics of palladium as a hydrogen selective membrane.

In Chapter 3, a detailed comparison of various experimental systems which thermally crack ammonia to produce hydrogen is presented to offer some background on what technologies are currently under development. Furthermore, two competing kinetic models will be mentioned with their individual equations and unique features. Based on some of the models available in the

literature, preliminary calculations to compare the effect of hydrogen removal on equilibrium and reaction rate were made.

Experimental works are discussed in Chapter 4. The main experimental apparatus of the overall system is the first item discussed. Process diagrams and schematics are presented along with a parts list. The rationale behind all design decisions will be presented and defended. The experimental methods for determining ammonia concentration in the raffinate stream will also be presented and compared to other methods. The rationale behind the choice of the method will be explained as well.

The experimental results are presented in Chapter 5. Several experimental results will be presented and discussed along with a comprehensive analysis. Items that will be presented are:

- Hydrogen production rates as a function of time for all combinations of pressure, temperature and flow rate.
- Concentration of ammonia in the raffinate stream as a function of time for all combinations of pressure, temperature and residence time.
- Ammonia conversion efficiency as a function of time for all combinations of pressure, temperature and flow rate.
- System efficiency as a function of time for all combinations of pressure, temperature and flow rate.
- Any changes in catalytic surface morphology due exposure to reacting ammonia in the temperature and pressure range of 400°C – 500.0°C and 5.0 – 20.0 bar, respectively. This will be done by a comparative qualitative analysis of images from a SEM.

The discussion in Chapter 5 is a reflective analysis on the results obtained from experimentation. Explanations will be offered from the literature and graphical results will be displayed in this section of this current thesis work. Lengthy data tables will be put in the appendix for reference.

Conclusions and Recommendations are the topics of the sixth and final chapter of this thesis work. The conclusions will be based on the results of the experiments whereas the potential developments will be a light extrapolation of the experimental results to be a

commentary on the potential employment of an ammonia decomposition membrane reactor system for hydrogen production for automotive and power generation industries.

### **1.3 Objectives and Motivation of Thesis Work**

As it currently stands, Dr. Dincer's research group at UOIT is exploring the development of various renewable energy technologies via ammonia. As was previously discussed, ammonia is a fantastic hydrogen carrier. The aim of the research group is to definitively understand the thermodynamic aspects of a thorough ammonia decomposition system for hydrogen production via experimentation and to hypothesize an application. The general objectives of this research are as follows:

- To construct a hydrogen production system from the thermal decomposition of ammonia in a membrane reactor.
- To determine energy and exergy efficiencies of said membrane reactor system in order to investigate parameters.
- To compare both energy and exergy performance parameters of the membrane reactor system with the performance of other contemporary works.
- To investigate transient and steady state behaviour of said membrane reactor and determine various transient – to - steady state “tipping” points in reactor performance.
- To investigate the effect of reacting ammonia at 5.0 – 20.0 bar and 400.0 – 500.0°C on catalyst surface morphology by a comparative analysis of samples in a scanning electron microscope (SEM).
- To propose a comprehensive system design centered around an ammonia fed membrane reactor which produces hydrogen as a fuel on demand.

The group feels that there is inadequate positive experimental work in the area of hydrogen production from ammonia decomposition to develop a hydrogen fuelled internal combustion engine for automotive or power generation purposes. Factors such as ammonia conversion efficiency, percentage of ammonia in the raffinate stream, system efficiency, potential catalyst damage, and concrete relations for transient behaviour are all required knowledge before any conclusions can be drawn and any further technical decisions can be made. It was concluded that the best method was experimentation.

## Chapter 2: Literature Review

Several systems for both large and small scale hydrogen production exist. They have been divided into two categories [3 - 6]:

- carbon based systems;
- non - carbon based systems.

The primary difference between the former and latter hydrogen production systems is the emission of  $\text{CO}_x$  from the reforming of carbon based substances such as fossil fuels, methanol, and off-gases from chemical processing plants [3, 4, 8]. Some examples of carbon based systems are: steam reforming of fossil fuels (e.g: SMR), methanol reforming and off-gas reforming. Conversely, the non- carbon based systems do not emit  $\text{CO}_x$  by using carbonless substances or sequestering any  $\text{CO}_x$  emissions as mentioned by [6, 9]. Thermodynamically speaking, the most efficient method of decomposing ammonia would be to design the system to act as a bottoming cycle for a cogeneration plant. Waste heat produced from any thermodynamic cycle could be used to meet the energy requirement for such a system. Finally, several factors are critical for an efficient and cost effective hydrogen production system from the decomposition of ammonia. Factors such as: choice of reactants and catalysts, chemical thermodynamics and the influence of chemical equilibrium, thermal-hydraulic design to enhance heat transfer characteristics, and proper membrane material selection are all critical towards the development of an efficient hydrogen production system from ammonia decomposition.

### 2.1 Ammonia as a Hydrogen Carrier

Christensen et al. [6] discussed the ideas and principles of the hydrogen economy. It was mentioned that unlike the fossil fuel based economy, the hydrogen economy is based on sustainability, versatility, improved energy efficiency, and reduced negative environmental impacts. To eliminate the potential safety risks and high infrastructure costs associated with pure hydrogen transportation in pipes, it was stated that a hydrogen economy requires a different means of transportation and storage from the fossil fuel economy. Moreover, storing gaseous or liquefied hydrogen presents several limitations. Liquefied hydrogen requires large, perfectly insulated storage containers maintained at approximately  $-253.0^\circ\text{C}$  to mitigate the constant boil-off due to heat transfer from the ambient atmosphere to the container. Finally, liquefied hydrogen

only has a 1/3 the volumetric energy content of gasoline which makes onboard storage cumbersome and costly. On those caveats, the idea of a hydrogen carrier is introduced. Some requirements that a “perfect” hydrogen carrier should possess are mentioned below. They are the following:

- The ideal hydrogen carrier should not be more expensive per unit volume than the hydrogen it carries.
- The ideal hydrogen carrier should be safe to store and transport.
- The ideal hydrogen carrier should be renewable and readily available in practically inexhaustible amounts.

In Ref. [6], the potential hydrogen storage technologies are divided into two categories: Direct and Indirect technologies. Direct storage technologies release hydrogen when they are heated and/or the pressure is lowered whereas indirect storage technologies involve removal of hydrogen from a hydrogenous compound via heat addition to sustain a chemical reaction. Upon inspection, direct hydrogen storage technologies seem to be the best due to the simplicity and the hydrogen production rate is limited by only adsorption/desorption processes. Currently, all known direct hydrogen storage technologies fail to meet U.S. DoE benchmarks for acceptable hydrogen production rates due to low desorption rates. Due to this, catalysts have been employed to attempt to increase the hydrogen production rate. It was reported that the addition of catalysts into the storage material introduced a void space which decreased its volumetric hydrogen storage density below the practical limits. Finally, most metal hydrides ignite when left in ambient air and/or explode when put into contact with water. For indirect hydrogen storage methods, the following table of candidates was made.

Table 2.1: Applicability of various indirect H<sub>2</sub> storage solutions

<b>Compound</b>	<b>Cost</b>	<b>Reforming Temperature</b>	<b>Purification Needed</b>
Hydrocarbons	Low	High	Moderate
Methanol	Moderate	Low	Moderate
Ethanol	High	Moderate	Moderate
Ammonia	Moderate	Low	Low

The former processes, save ammonia decomposition are well known as energy intensive, non-sustainable processes which emit CO<sub>x</sub> as a byproduct. Since ammonia is produced at a cost equal to that of hydrogen, is more plentiful than any other pure chemical, and is distributed through an already existing world-wide infrastructure; it was proposed that ammonia should be used as the “perfect” hydrogen carrier. In an indirect hydrogen storage scenario, it was suggested that metal amines such as hexa-amine-magnesium chloride (Mg(NH<sub>3</sub>)<sub>6</sub>Cl<sub>2</sub>) and hexa-amine-nickel chloride (Ni(NH<sub>3</sub>)<sub>6</sub>Cl<sub>2</sub>) as a safe, energy dense, cost effective, and CO<sub>2</sub> neutral method of hydrogen storage and production from ammonia while simultaneously minimizing the safety hazards and risks associated with anhydrous ammonia.

Metkemeijer and Achard [7] compared the indirect use of both methanol (CH<sub>3</sub>OH) and ammonia (NH<sub>3</sub>) for the production of hydrogen to use in a fuel cell. The following chemical reactions were considered and compared from both economical and thermodynamic perspectives:

Table 2.2: Comparison of NH<sub>3</sub> decomposition and CH<sub>3</sub>OH reforming reactions

Reaction	Enthalpy of Reaction (kJ/mol)
$\text{NH}_3 \rightarrow 1.5\text{H}_2 + 0.5\text{N}_2$	$\Delta H_{\text{rxn}} = 46.4$
$\text{CH}_3\text{OH} + \text{H}_2\text{O} \rightarrow 3\text{H}_2 + \text{CO}_2$	$\Delta H_{\text{rxn}} = 132.0$

The findings extensively showed that the decomposition of ammonia was more attractive than methanol reforming from both thermodynamic and economic perspectives. A comprehensive list of their findings is offered below:

- The maximum specific energy produced from ammonia decomposition is 2.68 kWh<sub>e</sub>/kg<sub>f</sub> which is approximately 229% more than the 1.17 kWh<sub>e</sub>/kg<sub>f</sub> obtained from the reforming of methanol.
- It was assumed that both ammonia and methanol had been both synthesized out of methane (CH<sub>4</sub>) with a specific energy requirement of 8.05 kWh/kg<sub>CH<sub>4</sub></sub>. It was concluded that the overall efficiency with respect to the lower heating value of methane of the indirect ammonia and methanol approaches were 33.3% and 22.9%, respectively.

Since water does not have a calorific value in the same respect as any fuel but is a requirement for the methanol reforming reaction, it serves as an “energy sink” that increases the required enthalpy of reaction further than that of pure methanol. Due to this, the maximum specific work from the methanol reforming reaction was lower than ammonia decomposition reaction. Secondly, the indirect methanol approach required use of a less efficient acid fuel cell ( $\eta_{\text{ACFC}} \sim 40\%$ ) due to  $\text{CO}_2$  production that destroys the electrolytes in an alkaline fuel cell. Conversely, the indirect ammonia approach can use a more efficient alkaline fuel cell ( $\eta_{\text{AFC}} \sim 60\%$ ) which allows for greater specific energy outputs and higher efficiencies. Finally, reverse scenario for hydrogen storage was considered. It was anticipated that since ammonia is easier to produce due to low energy requirements (see Table 2.2), the abundance of atmospheric nitrogen (79.0% of Earth’s atmosphere is diatomic nitrogen compared to 0.03%  $\text{CO}_2$ ) and an evolved fertilizer industry and infrastructure; therefore ammonia could serve as a relatively cheap and easy means of storing hydrogen.

Vitse et al. [10] introduces the concept of an electrochemical cell which can produce hydrogen from the electrolysis of ammonia. It was thoroughly proved that the decomposition of ammonia is a far more efficient thermodynamic and electrochemical process than the decomposition of water. In a comparison between only the electrolysis of water and the electrolysis of ammonia, the theoretical specific energy consumptions were 1.55 Wh/g $\text{H}_2$  and 33.0 Wh/g $\text{H}_2$ , respectively. Also, the theoretical cell voltages for both water and ammonia electrolysis were reported to be 1.223 V and 0.06 V, respectively. When both factors are considered, it shows that the decomposition of ammonia via electrolysis requires 95.0% less energy than the electrolysis of water. Due to the energy requirements associated with the decomposition of ammonia in an alkaline electrolyzer being much lower than that of water, therefore it would be viable to couple an ammonia fueled alkaline electrolyzer to a wind turbine and/or solar cell to produce hydrogen in a sustainable and  $\text{CO}_x$  free way. However, due to the fact that ammonia is not a primary feedstock in the same sense that water is, the energy required to produce the ammonia initially is not considered factored in. Therefore, in order to compare these more fairly, a life cycle assessment on the ammonia production must be conducted. Finally, the effect of various catalysts on reaction behavior was studied. It was found that ruthenium based catalysts performed well but required a greater cell voltage than iridium based catalysts for equivalent current densities. While unrelated to thermal decomposition of ammonia, this paper

comes to the same conclusion as the others previously mentioned. That conclusion is that ammonia serves as a clean and efficient hydrogen carrier that can easily be decomposed for the environmentally friendly production of hydrogen.

## **2.2 Chemical Reactor Modeling and Kinetic Considerations**

In this section, the relevant aspects of chemical reactor design and ammonia decomposition kinetics will be discussed. Firstly, a comparative overview of some experimental and analytical studies of the performance of both membrane and plug flow reactors. Secondly, an overview of selected experimental studies in the areas of both ammonia decomposition kinetics and the performance of various catalysts are reviewed.

### **2.2.1 Comparative Overview of Chemical Reactor Models**

The membrane reactor has been extensively studied since the late 1960's to further understand the equilibrium shift associated with the removal of products from the product stream. Modeling of chemical reactors that decompose ammonia to produce hydrogen for fuel cells, internal combustion engines, and for various industrial processes has been investigated by many researchers over several decades.

Kumar et al. [11] developed a comprehensive model for tubular catalytic membrane reactors that covers all possible scenarios. First and foremost, the model was developed such that it was applicable to palladium and/or palladium alloy based membrane. Also, the reaction taking place on the tube or shell side, isothermal and/or adiabatic operating conditions, reactive or non-reactive sweep gases, multi-component diffusion through the gas films on both sides of the membrane, and variations in operating pressure were all accounted for. Mass, energy, and momentum balances for the shell and tube sides of the reactor to model all flows into and out of the system were constructed. Furthermore, an extensive literature survey and developed permeation rate equations for both porous ceramic membranes and palladium/palladium alloy composite membranes had been done. Finally, a comparative case study of dehydrogenating ethylbenzene (EB) to produce styrene (ST) with four catalysts was done to validate the model. The reactor's performance was positively influenced by the change from a porous ceramic membrane to a palladium composite membrane. The results were increases of 2.36% in ethylbenzene conversion, 17.49% in styrene yield, 2.72% in styrene selectivity, and a decrease of 87.07% in ethylbenzene selectivity. It was concluded that the reason for such dramatic changes

in ethylbenzene conversion, styrene yield, and ethylbenzene selectivity was the relatively low hydrogen selectivity of the porous ceramic membrane compared to palladium alloys. In this case, the porous ceramic membrane considered was not purely selective to hydrogen and allowed ethylbenzene to permeate through as well. Effectively, this removal of reactants from the reaction side of the membrane had hindered the conversion of ethylbenzene by removal of reactant coupled with a decrease in trans-membrane pressure gradient. Furthermore, the effect of a reactive purge gas on the shell side of the reactor was simulated. It was found that this increased the conversion of ethylbenzene 6.0%, but only increased the yield of styrene 1.78%. When this is compared to the previously mentioned 17.49% increase in the yield of styrene obtained with the use of a hydrogen selective palladium composite membrane, it seemed almost counterproductive to use a reactive sweep gas instead of a palladium composite membrane. This was reasoned to be due to the fact that a palladium composite membrane has a much greater hydrogen selectivity than a porous ceramic membrane. The removal of products allowed the forward reaction to go further towards completion by Le Chatelier's Principle. Due to the purely hydrogen selective palladium composite membrane that allows for the sole removal of hydrogen from the reaction side had resulted in decreased percentage yield of toluene, benzene, and ethylbenzene and increases the yield of styrene only. Finally, a comparison between isothermal and non-isothermal operation had been done. It was determined that the ideal operating temperature was 925.0 K. The energy equation was solved for an axial temperature profile. This solution had illustrated that the temperature decreased from 925.0 K to 860.0 K for the initial 1/3 of the total length of the reactor due to the highly endothermic nature of the reactions. For the remaining 2/3 of reactor length, the temperature increased steadily towards 870.0 K. It was suggested that due to the endothermic nature of the reactions taking place, isothermal operation was an unreasonable assumption that overestimates the fractional conversion of ethylbenzene. In summation, a very general model with a broad scope of application was developed. It was concluded that a catalytic membrane reactor equipped with a hydrogen selective palladium composite membrane operating non-isothermally at 925.0 K performed better than an equivalent reactor equipped with a porous ceramic membrane due to increases in hydrogen selectivity and separation factor.

Kraisuwansarn [12] successfully simulated the catalytic decomposition of ammonia in both membrane and plug flow reactors and compared his numerical results to experimental

results found in literature. The study addressed the case of a membrane reactor was integrated into an IGCC power plant to decompose ammonia in the feed stream to simultaneously reduce the NO<sub>x</sub> outputs from the IGCC power plant and to produce hydrogen from the IGCC feed stream. The process was modeled as an initial value problem (IVP) subject to eight ordinary differential equations for mass balances on both the reaction and separation sides with the Gear's Method.

As an aside, Gear's Method was chosen due to its ability to efficiently solve initial value problems with a high "stiffness ratio". The stiffness ratio is defined as the quotient of the fastest rate and slowest rate ( $SR = R_{fast}/R_{slow}$ ) encountered in an initial value problem. Gear's Method is chosen as a solution methodology for initial value problems when the stiffness ratio is greater than 500. Moreover, it is capable of operating with stiffness ratios up to  $10^6$  [13]. The successful use of Gear's Method in this study was represented by the output of low percent error values from the program. This was reasoned to be primarily due to the forward reaction rate being  $10^3$  times faster than the reverse reaction in a membrane reactor.

In Ref. [12], the operating temperatures and pressures were chosen to replicate the feed stream to an IGCC power cycle. The range of temperatures and pressures inputted into the simulation were 810.0 – 1366.0 K and 18.0 – 35.0 bar, respectively. It was assumed that there was plug flow on both sides of the membrane, that the magnitude of the reverse reaction was negligible compared to the forward reaction, that there was negligible heat and mass transfer resistance in the catalyst bed, and that the removal mechanism was Knudsen diffusion. The results of this simulation had exhaustively proven the superiority of membrane reactors to plug flow reactors in all conditions. It was shown that there is an exponential decrease in hydrogen mole fraction along the length of the membrane reactor due to hydrogen removal via membrane. This decrease resulted in an equilibrium shift to favour the forward reaction and consequently consume more ammonia. Due to the previously mentioned equilibrium shift, there is an exponential decrease in ammonia mole fraction along the length of the reactor. A limitation of the direct employment of a membrane reactor to decompose the ammonia of an IGCC feed stream had been implied. That is, the presence of approximately 20.0% hydrogen mole fraction in the IGCC feed stream inhibits the forward reaction by initially contributing to the hydrogen partial pressure. The simulation had effectively shown that for a membrane reactor, a high mole fraction of hydrogen in the feed stream was detrimental to the ammonia conversion factor. This

point was illustrated by the decrease in ammonia conversion factor by 40.0% for a corresponding increase in feed hydrogen mole fraction of 20.0%. Finally, the optimum parameters for membrane reactor operation were discussed. From the results of the simulation, the researcher had concluded that the forward reaction could be driven further by the employment of a strictly hydrogen selective membrane such as palladium. This was due to the retention of reactant in the reaction side coupled with the allowance of only hydrogen to permeate. While stated by the researcher of this study, it was originally illustrated by Itoh et al. in [14]. This was illustrated by decreasing the selectivity of the membrane to 10.0% of the Knudsen effective diffusivity. As a result, the conversion ratio increased from 1.706 to 2.420. The thermodynamic advantages of using a membrane reactor over a plug flow reactor were extensively shown.

The author of [15] has been producing membrane reactor systems for years and has produced scholarly literature on the fundamentals of membrane reactor design and the benefits of using membrane reactors. Also, a handful of problems encountered with the use of plug flow reactors for facilitating the methanol reforming reaction had been outlined in [15]. The main thermodynamic problem was the competing natures of the methanol cracking reaction and the associated water – gas shift reaction that follows. The methanol reforming reaction is an endothermic reaction and requires high temperature and pressure for a fast reaction rate. Conversely, the water – gas shift reaction is exothermic and would ideally be done at low temperature and pressure to facilitate efficient heat transfer from the reaction. In order to meet these requirements in a plug flow reactor a large sequential reactor – separator would be required. By consequence, the cost must increase and the heat transfer problem associated with these reactions would be further complicated. Finally, the produced hydrogen from a sequential reactor – separator may not be 100% pure. This poses a large problem for the usage produced hydrogen in PEM fuel cells due to the large decrease in PEM fuel cell power density that is associated with decreased hydrogen purity. It was mentioned that a hydrogen feed that contains as little as 20.0 ppm of carbon monoxide concentrations can reduce the power density of a PEM fuel cell by a factor of three. Due to this, a large and expensive fuel cell may be required if 100% pure hydrogen is not used. This was determined to be undesirable, and therefore the use of a membrane reactor in place of a sequential reactor – separator as an economical and efficient solution to these problems was suggested. The extensive list of benefits includes the following:

- expanded range of allowed operating temperatures and pressures;
- increased residence time for a fixed reactor volume due to removal of products;
- increased residence time due to the decreased volumetric flow rate caused by increased higher operating pressures;
- inverted pressure dependence of gas phase decomposition reactions;
- plug flow caused by enhanced heat transfer due to removal of products;
- decreased reactor weight and volume due to the allowed increases in operating pressure.
- expanded range of applications (automotive, industrial, etc.) due to decreased reactor weight and volume;
- 100% purity of hydrogen due to palladium membranes having strict selectivity for hydrogen.

An experimental investigation of methanol reforming in a membrane reactor was conducted in [15]. The reactor was continuously fed a methanol – water mixture for one month and produced 100.0% pure hydrogen at a rate of 800.0 cc/min at 150.0 psi and 265.0°C. After the experimental period, it was noted that there was a major drawback with the membrane reactor; that being that 20.0% of the produced hydrogen was lost in the raffinate stream in order to drive the remaining 80.0% of the produced hydrogen through the membrane. At first sight this appears daunting, but it was stated that the 80.0% hydrogen recovery is still far greater than the percentage of hydrogen recovered in the standard sequential reactor – separator system. Furthermore, the researcher suggests that with a high quality membrane and catalyst, hydrogen losses could be potentially reduced to as low as 5.0%.

Garcia et al. [16] had investigated two reactor designs and discussed their ability to produce H<sub>2</sub>. The conventional catalytic reactor which used a non-porous tube for hydrogen transport was compared to a multifunctional catalytic membrane reactor (MCR); that employed a permeable palladium membrane for hydrogen transport and removal from the product stream via trans – membrane diffusion. Moreover, a few catalysts were investigated for comparative purposes. The MCR that used a ruthenium catalyst supported by carbon nanotubes (CNT) on a palladium coated porous stainless steel (Pd - PSS) composite membrane exhibited the best reactivity and stability at elevated temperatures. Furthermore, it was found that a Pd-PSS composite membrane is thermally and mechanically stable at temperatures ranging from 673.0 –

773.0 K. It was mentioned that ruthenium is rather expensive due to its scarcity. But this was speculated to potentially be offset by the increased hydrogen production at lower temperatures. Furthermore, this option looked promising at higher temperatures due to its greater thermal stability. It was determined that trans-membrane pressure difference ( $\Delta P$ ) and hydrogen flux are linearly proportional and are therefore to be modeled by the Sievert's Law. Generally speaking, it was observed that an increase in reactor temperature and trans - membrane pressure produces higher hydrogen fluxes via high reaction rates and product removal. In summation, a Pd - PSS membrane with ruthenium catalyst mounted on carbon nanotubes increased the hydrogen production at lower temperatures and therefore extends the lifespan of the membrane reactor.

### **2.2.2 Overview of Ammonia Decomposition Kinetics**

The kinetics of ammonia synthesis has been investigated by several researchers over the years in an effort to efficiently produce ammonia for use as a fertilizer in the agricultural industry. As time went on and the notion of a hydrogen economy gained credibility and picked up momentum, there was a push towards further understanding the kinetics of ammonia decomposition for efficient hydrogen production.

Roy et al. [17] had extensively reviewed the catalytic decomposition over alumina supported nickel catalyst at temperatures ranging from 400°C – 600°C with two catalysts; 10.0% and 15.0% nickel content, respectively. It had been found that the partial pressure of hydrogen reduced the ammonia decomposition rate over the entire temperature range and the presence of nitrogen had negligible effect on ammonia decomposition. Furthermore, temperature dependent shifts in the decomposition rate expression were noticed. Firstly, from 400°C – 440°C, the ratio of the orders of reaction were approximately 1.0. This was reported to be due to the Ozaki – Taylor – Boudart mechanism. Secondly, from 440°C – 460°C, an increased effect of ammonia partial pressure on decomposition rate was observed. This was modeled as a ratio of orders of reaction in the neighbourhood of 2.0. Finally, when the temperature was increased beyond 500°C, it was shown that the reaction was totally driven by the partial pressure of ammonia and the effect of hydrogen partial pressure was determined to be negligible. It was reasoned that the increase in temperature causes a decrease in hydrogen adsorption. Moreover, it was suggested that negligible hydrogen adsorption occurs at temperatures greater than 600°C. The consequence of this is an increased nitriding of the catalyst surface which was driven by an increase in

ammonia feed concentration. It was concluded that all these “intermediate” steps occur very fast and that explains the first order dependence of the reaction rate on ammonia and negligible hydrogen dependence on reaction order.

Tamaru [18] studied the catalytic decomposition and synthesis of ammonia over transition metals and had developed a novel description of the reaction kinetics – a “new” general mechanism. This was said to differ from the classical Tymken – Pyzhev mechanism due to the reaction rate always being order zero with respect to hydrogen. A dynamic approach was taken to account for the intermediate steps that take place in a catalytic reaction. For ammonia decomposition over tungsten, a series of intermediate steps that occurred before the production of diatomic hydrogen and nitrogen occurred was identified. The decomposition of ammonia gas had quickly formed chemisorbed nitrogen and hydrogen which slowed as more nitrogen was chemisorbed on the tungsten. Conversely, it was found that nitrogen desorption was initially slow and increased its rate over time. It was determined that nitrogen chemisorption was a proportional to ammonia partial pressure and decreased with nitrogen surface coverage. Conversely, the nitrogen desorption was found to decrease with increasing nitrogen surface coverage. Furthermore, the nitrogen desorption rate was approximated with a Langmuir rate equation. The Langmuir – Hinshelwood mechanism was said to be the governing mechanism of the ammonia decomposition over tungsten. In spite of this, it was suggested that ammonia decomposition was to be best interpreted in terms of a dynamic balance between the adsorption and desorption of nitrogen radicals on the tungsten surface.

As an aside, the question about what kinetic mechanism is active for a given set of reaction conditions is a valid one. The variations in reaction rate were due to both an inversely proportional relationship between activation energy and reaction temperature coupled with the decreasing inhibitive effects of hydrogen partial pressure with reaction temperature. To the researcher, this had suggested a change in kinetic mechanism. On those caveats, a line of reasoning to help determine the active kinetic mechanism was introduced. It was claimed that if the chemisorbed nitrogen reverts back into ammonia and does not have sufficient energy to recombine into diatomic nitrogen molecules, then there is a quasi – equilibrium formed between the nitrogen radicals and the ammonia due to the available free energy quickly approaching order zero. This criterion suggested that the Tymken – Pyzhev mechanism was active. On the other

hand, if the chemisorbed nitrogen is desorbed and recombined into nitrogen molecules rather than reverting back to form ammonia, then there was no quasi – equilibrium between ammonia, hydrogen, and chemisorbed nitrogen. By consequence, this suggested that the “new” mechanism was active. Due to the temperature dependence of the ammonia decomposition reaction, the researcher discussed the existence of a transitional temperature which serves as a patching condition between the two kinetic mechanisms. Mathematical validity was illustrated with a simple “plug and play” of some sample numbers and checking against experimental results. When ammonia was decomposed over an iron catalyst, the researcher mentioned a “tungsten – type” behaviour over a temperature range of 600.0 – 1250.0 K. A relevant and notable mention here is that this type of model would come to be known as Tamaru’s Model. In conclusion, the decomposition of ammonia on metal catalysts proceeds between the two cases with the former and latter cases being extreme boundary cases.

Chellappa et al. [19] examined the high temperature decomposition of ammonia at near atmospheric pressures over a nickel catalyst. The researchers were prompted to conduct this study to further understand the kinetic mechanisms of ammonia decomposition and to verify the existence of a transitional region where the Tymken – Pyzhev mechanism changes to a Tamaru mechanism. Also, the requirement of ultra – pure hydrogen for PEM fuel cell operations can only be realized with the decomposition of ammonia at high concentrations ( > 99.0 % ). Due to the nature of catalytic reactions, the rate of ammonia decomposition was assumed intrinsically related to nitrogen chemisorption and recombinative desorption from the catalyst surface. The existence of a quasi – equilibrium state is claimed due to rate limiting nitrogen desorption. It should be noted here that due to the employment of an integral flow reactor, the reverse reaction was neglected. A differential analysis of integral data and had fitted their data to a power law rate model. A statistical analysis of the variables had shown that the conversion factor and reaction rates were predominantly influenced by ammonia pressure. The data was analyzed with the Tymken – Pyzhev model and calculated the reaction orders of ammonia and hydrogen. They had determined that the reaction orders with respect to ammonia and hydrogen were 0.67 and -1.0, respectively. Due to this, the researchers had not ruled out the possibility of reaction inhibition via hydrogen partial pressure. A maximum ammonia conversion of 99.74% at 500.0°C and 1.0 bar was calculated. Moreover, the data seemed to suggest that the activation energy is catalyst specific. This led to the conclusion that N–H bond cleavage was not a rate limiting process in

ammonia decomposition. Finally, the stability of the nickel catalyst was measured by running experiments over a continuous 15 day time period and attempting to measure any deviation in hydrogen production under a fixed set of experimental conditions over time.

According to Yin et al. [20], a ruthenium catalyst supported on carbon nanotubes and promoted by potassium hydroxide was found to be the most effective catalyst for the thermal decomposition of ammonia. The kinetics of ammonia decomposition were discussed and it was discovered that for temperatures less than 650.0 K, the recombinative desorption of nitrogen atoms was determined to be a rate limiting step. The turn over frequency data had seemed to indicate that when the temperature was decreased for nitrogen desorption, the turnover frequency increased. This had led to the conclusion that the recombinative desorption of diatomic nitrogen was the rate determining step at lower temperatures. Conversely, at temperatures greater than 750.0 K the breaking of N - H bonds of the adsorbed ammonia was determined to be a rate limiting step due to its high energy requirement. Furthermore, the high turnover frequency indicated that a ruthenium based catalyst had the highest activity whereas the nickel had the lowest. The effect of ruthenium concentration for ammonia decomposition was also noted. The researchers had found that for high concentrations of ruthenium, overall catalytic efficiency had been theorized to be relatively low due to the burying of active ruthenium sites in sub - layers. A link between the pH of the support to the catalytic efficiency was established. It was showed that alkalinity increased catalytic efficiency and acidity hindered catalytic efficiency. The promoter in this work was potassium hydroxide. This was justified by the increase in ammonia turn over frequency number.

### **2.3 Heat and Flow Considerations in Packed Beds**

Packed beds are commonly used in both chemical and process industries. They have proven to be functional as heat exchangers, reactors, separators, dryers and filters. The fundamentals and other relevant aspects of heat and fluid flow in packed beds are discussed in this section.

Schlunder [21] discussed both heat and mass transfer mechanisms in packed beds. Furthermore, a simple model for the heat transport in packed beds in order to accurately predict effective thermal conductivities in packed beds was developed. Several mathematical limits as a function of gas velocity flowing through the bed were shown. For extremely high gas velocities, the quantities of thermal and mass diffusivity are shown to be equal by a limit expression. Also,

heat transfer via conduction and radiation are assumed to be negligible when compared to the heat transfer via forced convection. Conversely, for extremely low gas velocities; the dominant heat transfer mechanism is conduction and the effective thermal conductivity of the packed bed – gas flow regime is reduced to that of the thermal conductivity of the packed bed. Physically, this is a “zero – flow rate” limit. Equations were derived by the superposition of the results from the above mentioned limits. These were then taken to derive equations for thermal diffusivity for 1 - d and 2 - d flux cases. As a final step, the previously mentioned expressions were used and went further to determine equations for the convective Peclet number as a function of the molecular Peclet number for both 1 - d and 2 - d flux cases, respectively.

The mathematical analysis was reinforced and supported with experimental results. The resulting axial and radial temperature profiles were obtained as a function of reciprocal bed height and dimensionless radius, respectively. The results had shown a positive, increasing and linear relationship between centerline temperature and reciprocal bed height. Also, a positive relationship was shown between increasing gas velocity and increasing centerline temperature. However, the radial dimensionless temperature difference profile was shown as a negative, decreasing, and linear relationship as dimensionless radius approached unity. Alternatively, the effect of gas velocity was inversely proportional to the radial dimensionless temperature gradient. With respect to the temperature profiles, the only error observed was due to an unavoidable scatter of temperatures along the circumference of the packed bed due to imperfect packing. It was shown that poor conductors (insulators) with relatively high molecular Peclet numbers have a convective Peclet number that is within the close neighborhood of the asymptotic value and exhibited negligible changes in behaviour for any change in gas velocities. On the other hand, it was shown that for good conductors with relatively low molecular Peclet numbers, the convective Peclet number would approach the asymptotic value of roughly 8.5 but only at much higher gas velocities. This is due to the required reduction of the contribution of conductive heat transfer in order to increase the contribution of convective heat transfer and by extension increasing the convective Peclet number. It was determined that the effective conductivity of a packed bed of materials with relatively low Peclet numbers was much higher. The results of the experimental work were in good agreement with the contemporary literature on the topic at the time. Furthermore, the experimental results were remarkably accurate and had only a maximum error of slightly less than 7.0%.

Achenbach [22] had extensively reviewed the heat and flow characteristics in a packed bed. It was stated that the forced convective heat transfer that takes place in a packed bed differs significantly from that in a bare tube due to the existence of small spheres (the packing) and their arrangement. Also, the increased difficulty of accurately representing an “infinitely” large and randomly packed bed in a general fashion further exacerbates this heat and fluid flow problem. The two main factors that affect forced convection in a packed bed that are of prime importance are the statistical void fraction and tube - particle diameter ratio. Due to this, modified expressions for Reynolds and Nusselt numbers to be a function of statistical void fraction were derived for this purpose. As the statistical void fraction approached zero, the Reynolds number showed decreasing behaviour which indicated that the packed bed is a form of flow resistance and ergo; inhibits the onset of turbulent flow. Moreover, the Nusselt number showed decreasing behaviour like the statistical void fraction. This was due to the conductive nature of the packing and the wall – particle conduction which reduces Nusselt number. Five experimental techniques were mentioned, the reasoning behind their use was explained, various examples of their usage and finally, their limitations. It was suggested that empirical heat transfer results should be expressed via a formula for Nusselt number that will be solely a function of Reynolds number, Prandtl number, and statistical void fraction. As an extension of this with respect to fluid flow through a packed bed, the researcher states that the pressure drop across a packed bed is solely a function of Reynolds number and statistical void fraction. It was determined that the pressure drop through a packed bed was very sensitive to changes in statistical void fraction. The steep and positive gradients associated with the derivative expression representing the change in pressure drop to the change in statistical void fraction for very large and very small Reynolds numbers indicated the magnitude of the statistical void fraction and served as grounds for the existence of what the researcher calls the “bypass effect”. This was due to non - uniformities in the statistical void fraction with respect to radius. The statistical void fraction at the wall was found to be higher than the average value for the bed and therefore it was a local region of high velocity. The bypass effect can skew heat and fluid flow calculations. This was speculated as the probable explanation for the large differences in the reported experimental results. In a packed bed, the thermal conductivity was treated differently; its nature slightly changes from a purely material property to a property of the flow regime in question. Depending on the heat and flow conditions encountered, it was suggested that the thermal conductivity was best to be thought of

as the sum of flow and stagnant gas thermal conductivities. An interesting relationship which linearly relates the flow thermal conductivity to the Peclet number was mentioned. Its purpose was to model the change in heat exchange as a function of velocity fluctuations. It was speculated that the stagnant gas conductivity was affected by a handful of various heat transfer mechanisms:

- conduction through the gas and solid phases;
- solid – solid and “trans – void” area radiation heat transfer;
- conduction through contact patches;
- pressure dependent thermal conductivity of gases (Smoluchowski effect).

Finally, the experimental work employed a naphthalene mass transfer method with a constant wall concentration boundary condition to simulate the constant wall temperature boundary condition. The expression for wall Nusselt number as a function of Reynolds and Prandtl numbers was obtained. Good agreement was obtained for a large range of Reynolds number, however, it lost its accuracy at Reynolds numbers less than 100 due to a predominantly diffusion driven heat transfer regime that dwarfs the relative magnitude of the contribution of forced convective heat transfer.

Wen et al. [23] reported on transient and steady state heat transfer of gas flow through a packed bed with a constant wall temperature. Experiments were conducted under the constant wall temperature condition and expressions for convective heat transfer coefficient, axial and radial thermal conductivities were derived from the experimental results. The experimental unit was a vertical stainless steel column that was 1100.0 mm tall with inner and outer diameters of 41.0 and 48.0 mm, respectively. J-type thermocouples were placed into the packed bed at seven axial positions (30.0 mm, 188.0 mm, 379.0 mm, 579.0 mm, 764.0 mm, 964.0 mm, and 1062.0 mm) and at the 579.0 mm and 764.0 mm axial positions, there were thermocouples arranged in five radial positions (0.0 mm, 5.0 mm, 10.0 mm, 15.0 mm, 20.0 mm, and 24.0 mm). The wall was kept at a constant temperature of  $100.0^{\circ}\text{C} \pm 2^{\circ}\text{C}$  by an electrical heater. The column was packed with glass spheres that were 5.0mm in diameter. Axial and radial temperature profiles were obtained from the experimental results and it was found that the constant wall temperature condition had resulted in inversely proportional behaviour between Reynolds number and

particle – gas convective heat transfer coefficient. By consequence, a greater amount of heat was transferred into the packed bed.

Furthermore, the data collected had shown the system reached steady state after approximately 5000 seconds and it was found that the temperature increased towards the wall temperature with increasing axial distance. The axial temperature was found to have an S – shaped profile. As expected by intuition, the bulk fluid temperature was determined to be the lowest along the centerline of the bed and increased to the wall temperature by the exit of the bed. The results were correlated to the solution for dimensionless axial and radial temperature profiles of a two dimensional, axial dispersion, plug flow energy equation with good agreement. With respect to the dimensionless axial temperature profile, the main discrepancy existed in the former half of the reactor where unsteady heat transfer and changing physical properties of the flow were claimed to be accountable. On the other hand, the solution for the dimensionless radial temperature profile had a good fit with the experimental data for an axial position of 579.0 mm. However, it had overshoot the experimental data for an axial position of 764.0 mm due to a variable wall convective heat transfer coefficient as opposed to a constant value. Finally, it was determined that the effective wall heat transfer coefficient was best modeled as a function of the Reynolds number by the Li – Finlayson correlation.

#### **2.4 Palladium as a Hydrogen Selective Membrane**

A membrane is defined as a permeable and selective surface that allows one way mass transfer through it via positive pressure gradient across the membrane. Membranes exist throughout nature. An example of a membrane is human skin. Human skin can be thought of as a membrane that allows sweat to permeate from the inside out but does not allow water to permeate from the outside in. Palladium has been identified as a hydrogen selective membrane that is capable of absorbing 900 times its own volume in hydrogen. There is a large body of literature on the study of hydrogen diffusion through palladium. A great deal of study in the area of surface science has been done with particular focus on the palladium – hydrogen system due to the potential of palladium as a hydrogen storage and transport medium.

Gryazanov [24] reported that the first metallic membrane was a palladium tube constructed by T. Graham. Hydrogen gas is able to diffuse easily through palladium and its alloys. This makes palladium membranes an attractive option for high purity hydrogen

separation from a flow stream in a chemical reactor. The researcher broke down the process of hydrogen mass transfer from the flow stream to the exterior in five sub-processes:

- disassociative hydrogen adsorption onto the palladium surface;
- the Langmuir chemisorption of hydrogen atoms in a penetration site;
- the Fickian diffusion of hydrogen atoms through the palladium membrane;
- recombinative desorption of hydrogen from the palladium surface;
- molecular gas transport away from the membrane surface and into the free stream.

It was noted that the first step requires little to no activation energy. Secondly, it was reported that the permeability of palladium alloys differs from that of pure palladium. The table below presents an excerpt of the findings.

Table 2.3: Relative permeability of palladium and its alloys

<b>Pd (%)</b>	<b>Ag (%)</b>	<b>Au (%)</b>	<b>In (%)</b>	<b>Ru (%)</b>	<b>P<sub>alloy</sub>/P<sub>Pd</sub></b>
100.0	-	-	-	-	1.00
90.0	10.0	-	-	-	1.50
80.0	20.0	-	-	-	1.60
70.0	30.0	-	-	-	1.80
60.0	40.0	-	-	-	1.80
95.0	-	5.0	-	-	2.00
93.5	-	-	6.0	0.50	2.80

The reasons for increased permeability of palladium alloys compared to pure palladium were said to be likely due to decreased tortuosity of the membrane due to alloying, decreased activation energy due to increased catalytic effects, and an increase in the mean free path of the hydrogen gas. The latter would result in a shift from a purely Fickian regime to include Knudsen like behaviour. In addition to the increased permeability of palladium alloy membranes, a couple more benefits of palladium alloys compared to pure palladium were suggested. These were said to be that palladium alloys handle thermal cycling in the presence of hydrogen better than pure palladium and they have a 500.0% increase in lifetime. Finally, experimental study on the dehydrogenation of cyclohexane in a membrane reactor equipped with a palladium membrane and packed with a dehydrogenation catalyst – in this case either Cr<sub>2</sub>O<sub>3</sub>/Al<sub>2</sub>O<sub>3</sub> or Pt-Re/Al<sub>2</sub>O<sub>3</sub> was

conducted. The hydrogen selective palladium membrane coupled with the catalyst had resulted in much higher conversions due to hydrogen removal and increased residence time. It was also suggested that the palladium membrane would eliminate side reactions by selective removal of products and retain all reactants.

The phenomenon of hydrogen permeation in bulk palladium membranes has several steps in series. Ward et al. [25] analyzed this topic from a kinetic point of view and developed a comprehensive model of hydrogen permeation through a palladium membrane. The list of steps given in [24] had been further expanded upon to give a total of seven.

- molecular transport from the bulk gas to the gas layer adjacent to the surface;
- disassociative adsorption of hydrogen onto the membrane surface;
- transition of atomic hydrogen from the surface into the bulk of the palladium membrane;
- the Fickian diffusion of atomic hydrogen through the palladium membrane;
- transition of atomic hydrogen from the opposite membrane surface;
- recombinative desorption of hydrogen from the membrane surface;
- molecular gas transport away from the membrane surface and into the free stream.

Due to the lengthy list of mechanisms that occur during hydrogen diffusion through bulk palladium, a detailed mathematical model verified by a comparison with known data from other group's experimental works was deemed sufficiently comprehensive and accurate. It had been shown that the Sievert's Law was valid for palladium membranes with a thickness less than 10.0  $\mu\text{m}$ . However, the manufacturing of such thin membranes remains a complicated technical issue. The effects of external mass transfer resistance through a thin gas layer in the neighbourhood of the surface during the adsorption and desorption steps was accounted for. The results had indicated a large undershooting of hydrogen flux due to mass transfer resistance through a gas layer. When the results were compared to the Sievert's Law, a transitional temperature of 450.0 K was determined to be where the diffusion of hydrogen through a palladium membrane changed from a desorption limited process to become trans – membrane pressure gradient driven and obeying the Sievert's Law.

Adsorption was determined to be the rate limiting step in the case where the partial pressure of hydrogen in the mixture was low or if the membrane had been contaminated. Two

potential adsorption mechanisms: Langmuir and Quasi – Chemical adsorption were compared. The former was found to only be valid for low surface coverage of hydrogen on palladium and is modeled as an exponential decrease of adsorption rate with increasing surface coverage. Conversely, the latter has been proven to be valid over all surface coverage values and is based on a probabilistic surface coverage expression. For a low surface coverage, the adsorption rate is mildly affected. As surface coverage increases, the adsorption rate exponentially decreases rapidly. This model was chosen to be applied to both the disassociative adsorption and recombinative desorption processes due to its validity over a complete range of surface coverage. The bulk diffusion process was modeled as a Fickian diffusion process due to the nature of the palladium membrane. The conditions by which bulk diffusion would be a rate limiting process were investigated and it was found that between 240°C – 640°C, little to no data suggested that bulk diffusion is a rate limiting step. Furthermore, a relationship between the surface – to – bulk diffusion process on the feed side to the bulk – to – surface diffusion process occurring on the permeate side and had determined that the bulk – to – surface diffusion rate was much faster than the surface – to – bulk diffusion rate. Relationships between temperature and surface coverage on both sides of the membrane were established. These had determined that on both sides of the membrane, surface coverage was inversely proportional to temperature. This was suggested to be the reason for the observed increase of hydrogen flux corresponding to increasing temperature. Finally, the limitations on hydrogen flux through a palladium membrane were mentioned. It was determined that if bulk diffusion was the rate limiting step, then the hydrogen flux through the membrane would be at a minimum. Alternatively, it had been determined that maximum hydrogen flux would occur if only bulk – to – surface diffusion was the limiting step.

Morreale et al. [26] had conducted a novel study on the permeability of hydrogen in palladium at high temperatures and pressures. The pressure ranges examined were 10.0 – 27.6 bar and the temperature ranges were 623.0 – 1173.0 K. The importance of this high temperature and high pressure study was driven by the increasing use of palladium and palladium alloys in membrane reactors for hydrogen production and separation. It was mentioned that palladium has several advantages in its role as a hydrogen membrane such as: catalytic surface, high hydrogen permeability, near infinite selectivity for hydrogen, thermal stability, and corrosion resistance. Furthermore, it was mentioned that the hydrogen permeability of a palladium membrane should increase due to the required activation energies for diffusion processes are endothermic. Since

the hydrogen flux through a palladium membrane is a diffusion dominated regime as previously established in [25], it was concluded that the permeability increases with increasing temperature.

The Sievert's Law was also discussed at length and a connection was made between the deviation of the pressure exponent and palladium membrane properties. A partial pressure exponent of 0.50 was defined as corresponding to a scenario in which the hydrogen atoms formed a perfect solution in the bulk palladium and then diffused through. Due to this, it was concluded that any pressure exponents greater than 0.50 were due to membrane leakage in thin membranes, membrane poisoning by unwanted substances, lattice defects, mass transport resistances, thermal hysteresis, and if a composite membrane is employed; palladium – support interfacial effects. A hydrogen permeability test bench to conduct experiments was constructed. Experiments were conducted by varying the pressure drop across the membrane for five isotherms. Furthermore, the previously defined relationship of increasing permeability with increasing temperature was again verified. The Sievert's Law behaviour was observed with respect to the trans – membrane pressure difference. However, the best fit to the experimental data was found not to be a partial pressure exponent of 0.50, rather it was determined to be 0.62. The reasons for this were determined to be the existence of a surface adsorption/desorption or a surface – gas diffusion rate limiting step. Finally, it was concluded that due to the high pressures, the concentration of hydrogen atoms in the palladium lattice may have increased in a fashion to inhibit the formation of an ideal hydrogen solution in palladium. Overall, the results compared favourably with previously established results from low pressure experiments.

According to Al-Raisi et al. [27], the transport of atomic hydrogen through a palladium membrane was said to be best modeled by the Sievert's Law if the adsorption equilibrium constant is the same on feed and permeate sides. The Sievert's Law can also be extended to be applicable in modeling hydrogen flux. The pressure exponent was constrained to a value of 0.50 and the membrane thickness at 25.0  $\mu\text{m}$ . The investigation had been conducted over a temperature range of 473.0 – 573.0 K, and with/without a helium sweep gas. Furthermore, it was postulated that potential increased rates of atomic hydrogen diffusion could lead to a potential depletion of atomic hydrogen throughout the membrane can potentially cause a gas layer of ammonia and nitrogen could form and impede the flux of atomic hydrogen from the reactor vessel by acting as a source of mass transfer resistance. It had also been proven that with an

increasing mole fraction of helium sweep gas, the boundary layer thickness increased linearly. This was hypothesized to be an effect of increasing degree of concentration polarization and they proposed that this can be minimized by increasing the ammonia feed flow rate. This was all assumed to be during steady state operation of the membrane.

It should be noted that palladium and palladium alloys are just one of many types of hydrogen selective membranes. That being said, Kluiters [28] delivered an extensive status review on membrane systems for hydrogen separation from IGCC systems. A list of some advantages and disadvantages associated with membrane technology was mentioned. Some advantages of membranes were determined to be:

- low energy consumption during operation;
- the potential to separate a desired substance continuously;
- ability to operate under mild process conditions;
- membranes scale up or down very easily;
- ability to operate without the addition of any activating substances;
- membranes can easily be combined with other separation technologies.

However, membranes also have some disadvantages inherent to them. Some disadvantages of membranes were determined to be:

- depending on the material, membranes have a tendency for fouling and/or poisoning;
- depending on the application, membrane lifetimes are typically short;
- depending on the material and operating conditions, the membrane may have low selectivity and/or flux;
- an area dependent linear scaling up factor as opposed to an economy of scale.

The palladium membrane had been compared to various other membrane materials and several points had been noted. As a hydrogen selective membrane, palladium and related alloys exhibit great temperature stability from 300.0°C – 600.0°C. Furthermore, they show the highest selectivity to hydrogen and highest hydrogen flux compared to other types of membranes. The only material limitations on palladium and related alloys was the damage due to  $\alpha - \beta$  phase transition and potential poisoning by hydrogen sulfide, hydrochloric acid, and carbon monoxide.

Poisoning of the membrane surfaces had been mentioned to reduce the hydrogen flux by upwards of 20.0 %. Consistent with the previous studies [24 - 27], the transport mechanism of hydrogen through a palladium membrane was said to be a Fickian diffusion process. Finally, the researchers also suggest that the modeling of membrane flux should be done with the Sievert's Law.

## Chapter 3: Background Information

A broad and comprehensive background study is conducted in this section of the thesis work to mathematically communicate the physical details of the thermal decomposition of ammonia in a catalytic membrane reactor to produce hydrogen. A detailed overview of three different ammonia thermal decomposition systems is presented here based on the literature. Reaction kinetics and catalytic reactions are discussed in detail. The power rate law and Tymken – Pyzhev model are both discussed in detail. A mathematical case for the thermal decomposition of ammonia is made by comparing the reaction kinetics and production rates of methanol reforming and steam methane reforming. Furthermore, the effect of product extraction is modeled and applied to a simple batch reaction to simulate the effect of a “membrane” on the equilibrium concentrations of the three reactions considered. A commentary about the environmental aspects of the three reactions is also made based on the results of the mathematical study. Finally, a simple hypothetical model of a shell and tube type membrane reactor is modeled to bring together all the models found in the literature and form a mathematical understanding of the physical phenomena occurring.

### 3.1 Current Hydrogen Production Systems from Ammonia Decomposition

In this section, a detailed review of some current hydrogen production systems from the thermal decomposition of ammonia is presented.

Table 3.1: Experimental systems reviewed in this thesis work

System #	System	Reference
1	Micro-Reforming with Micro-Combustor	Kim et al. [29]
2	CMR Fed by NH <sub>3</sub> Plant Purge Gases	Rahimpour et al. [8]
3	NH <sub>3</sub> Cracker for H <sub>2</sub> Production	Kordesch et al. [30]

#### 3.1.1 The Micro-Reforming System with Micro-Combustor

The first system presented in this thesis was published by Kim et al. [29]. A micro – reformer that is heated by an annular micro – combustor to produce hydrogen from the thermal decomposition of ammonia was developed and tested. An annular type micro – combustor fueled by propane as a heat supply to simulate the effect of gas velocity on hydrogen production was

chosen. This was determined to be a far more practical alternative to electrical heating due to cost, scaling, and deployment issues. In order to employ this reformer to produce hydrogen for automotive or industrial purposes, it was suggested that the odds are in favour of hot exhaust/flue gases being used as a heat supply. The reasons for this are due to the different mechanisms of heat transfer associated with heating by exhaust/flue gases and electrical heating. In the case of the former, gas – metal heat transfer is taking place by forced convection from a flowing exhaust/flue gas to the reactor. This scenario would be applicable for automotive and cogeneration applications. Whereas in the latter, the heat transfer mechanism is natural convection across an annular gap from a hot wall heated by electrical resistance to the reactor placed in the center. This scenario is more applicable to experimental analyses and would take much work to adapt it for an automotive or industrial application. Below is the diagram of the experimental apparatus of [29].

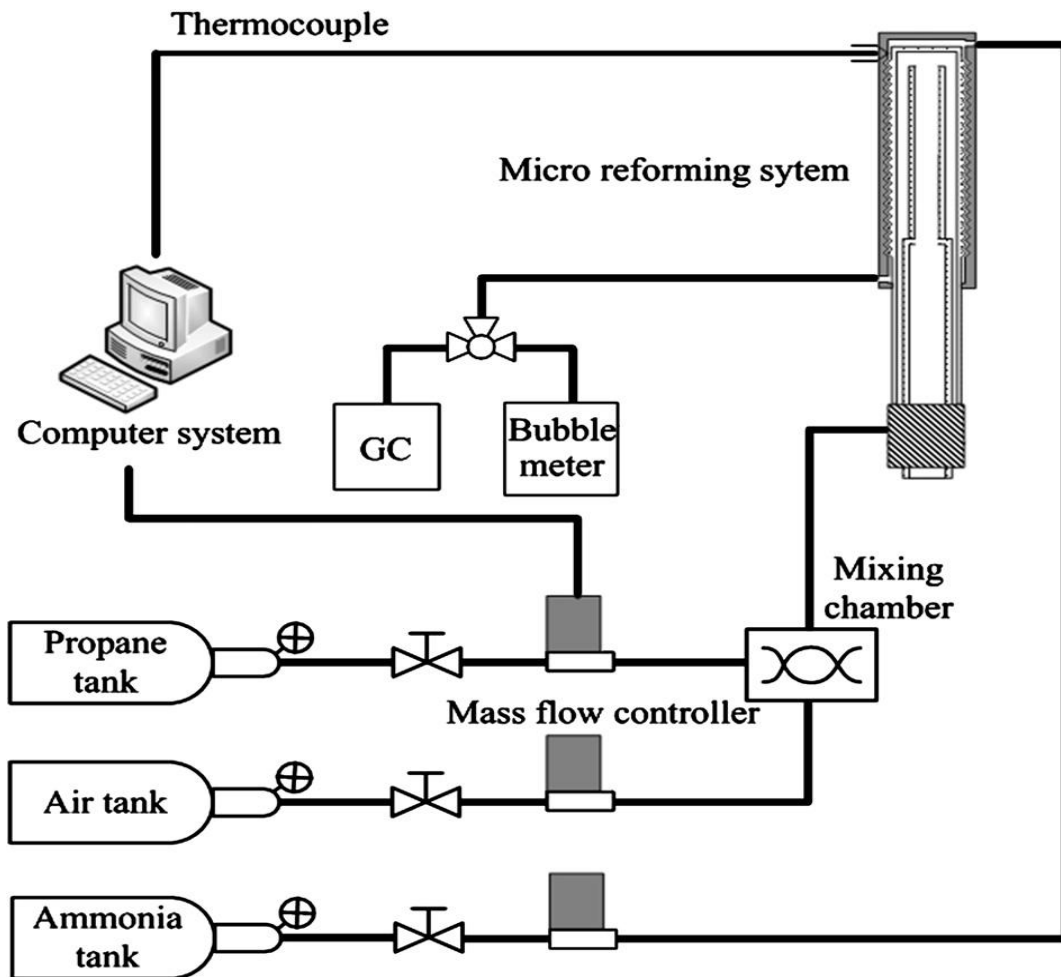


Figure 3.1: Process diagram of the micro - reforming system (Kim et al. [29]).

This research group had tested three catalysts: nickel, ruthenium, and iridium. It was found that ruthenium was the most active catalyst due to the increased production of hydrogen. This agrees with [20, 24]. The effect of gas velocity was determined to be profound and central to the efficiency of the system. The variation of gas velocity served as a method of active control in this experiment. In order to determine the optimal balance of output to input, gas velocity was varied from 2.6 – 3.7 m/s. It had been determined that the effect of high gas velocities was increased heat transfer to the reformer, in other words, a larger input. This increased efficiency to a point where the input became excessive. Beyond this point, system efficiency dropped off drastically. Also, this behaviour was observed with ammonia flow rate. As ammonia flow rate increased, conversion percentage and system efficiency increased to an optimum point. The optimum value which produced maximum conversion percentage and system efficiency was experimentally determined to be approximately 10.0 mL/min. Furthermore, the optimum operating parameters of the system were determined. With a ruthenium catalyst, the micro – reformer produced a maximum of 5.40 W of hydrogen. The optimal gas velocity was determined to be 3.1 m/s which led to both a maximum ammonia conversion percentage of 98.0% and system efficiency of 13.7%. The minimum ammonia concentration in the raffinate stream was found to be approximately 10,000 ppm. When operating with a nickel catalyst, the researchers determined an optimal gas velocity of 3.7 m/s and a maximum system efficiency of approximately 6.0%. Due to this, a filtration system to catch and recycle ammonia to further decrease the concentration in the raffinate stream was recommended as well. This approach is recommended for micro – reformer use with PEM fuel cells.

### **3.1.2 The CMR fed by NH<sub>3</sub> Plant Purge Gases**

The second system mentioned in this thesis was envisioned as a hydrogen production system from ammonia plant purge gases. Rahimpour et al. [8] proposed to couple a continuous membrane reactor (CMR) to simultaneously produce and separate hydrogen from the purge gases used in ammonia plants. Potentially, 6035.0 tons of hydrogen could be produced annually from such a setup. A model was developed to determine the effects of reactor temperature, feed pressure, membrane thickness and sweep gas ratio on hydrogen recovery for both co – current and counter – current reactors. Finally, a batch reactor was compared to a membrane reactor. The conclusions reached were the same conclusions as in [11,12,15]. Moreover, [8] had again

demonstrated the superior performance of a membrane reactor compared to a batch reactor. A schematic of the CMR system considered was taken from [8] shown in Figure 3.2.

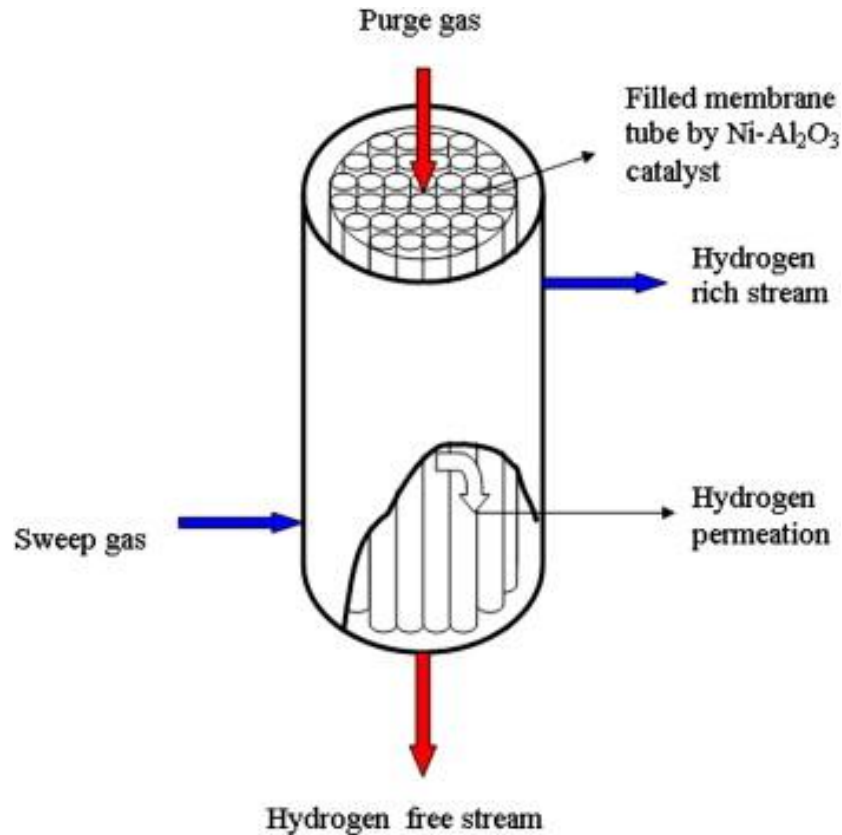


Figure 3.2: Diagram of shell and tube C.M.R (Rahimpour et al. [8]).

Like several other research works mentioned in this thesis, [8] had reaffirmed the positive relationship between hydrogen production and ammonia conversion percentage with temperature. The temperatures explored in this study ranged from 623.0 – 923.0 K. The family of curves that portray ammonia conversion percentage as a function of dimensionless reactor length illustrates how elevated temperatures reduce the required reactor length. The consequences of this are not explicitly mentioned in the work, but the reduction of required reactor length allows for greater flow rates for a fixed reactor size by simply increasing the operating temperature. It should be noted that a negative ammonia conversion in the entry region of the reactor is due to the reverse reaction creating ammonia from hydrogen in the feed stream. This is due to the reaction rate being an Arrhenius type relationship that varies exponentially with temperature. Increasing pressure from 15.0 atm to 25.0 atm and then to 35.0 atm generates a

family of curves which illustrated the moderate increase of hydrogen recovery from approximately 90.0 mol/hr to approximately 110.0 mol/hr for 15.0 atm to 35.0 atm, respectively. The high feed pressure would generate an increase of trans – membrane pressure difference. Coupled with an inverted pressure dependence associated with membrane reactors, there is an increase in hydrogen flux. An inverse relationship between membrane thickness and hydrogen recovery was shown. When the membrane thickness was decreased from 0.014 mm to 0.010 mm, the hydrogen recovery had increased from approximately 70.0 mol/hr to 90.0 mol/hr, respectively. Thinner membranes exhibit higher permeability due to the existence of a less tortuous path for hydrogen atoms to diffuse through. The effect of using a sweep gas on hydrogen removal was investigated. A sweep gas ratio (SGR) was defined as the quotient of sweep gas flow rate to feed flow rate. In this work, the sweep gas ratio was varied from 0.0 to 0.8 and determined that the ammonia conversion increased drastically with increasing sweep gas ratio. Ammonia conversion increased from approximately 20.0% to approximately 98.0%. The reasons for this were determined to be that the “sweeping” effect of the sweep gas is similar to product removal and by the Le Chatalier’s principle, pushed the forward reaction further. Finally, co – current and counter – current operation were compared and contrasted. Finally, it was determined that counter – current operation was superior due to the bulk of hydrogen recovery occurring in the former 1/2 of the reactor length. This was believed to be due to increased hydrogen removal from the surface of the exit side of the membrane.

### **3.1.3 The NH<sub>3</sub> Cracker for H<sub>2</sub> Production**

The inventors Kordesch et al. [30] developed and patented an ammonia cracker system for the production of hydrogen from the decomposition of ammonia. It was claimed that the system in [30] could be self-sustaining by proportioning the produced hydrogen to both supply heat to the cracker unit and to fuel an alkaline fuel cell. Comparisons between both a tube type and plate type cracker were made and it was determined that the plate type cracker was easier to manufacture, had a more uniform heat distribution, and was easier to scale up. The schematic of the invented system is presented below in Figure 3.3.

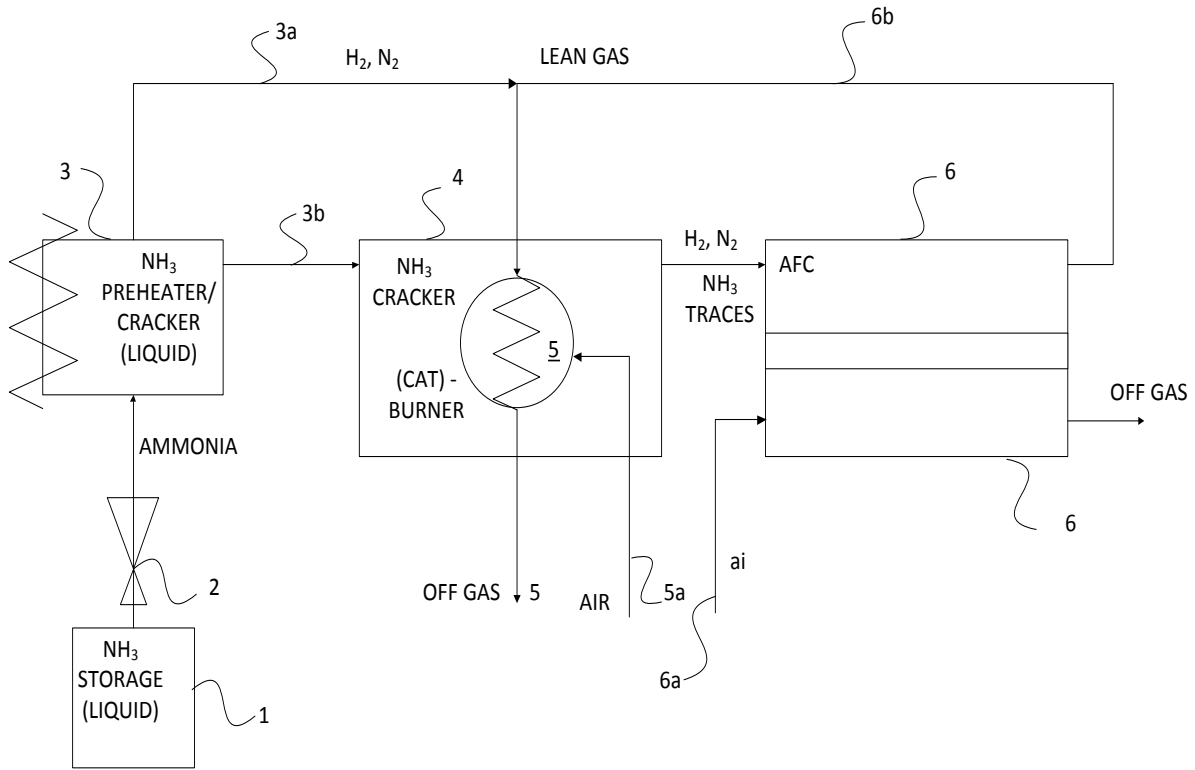


Figure 3.3: Schematic of NH<sub>3</sub> cracking system (adapted from Kordesch et al. [30]).

In order to address the problem associated with start – up, it was suggested that an ammonia heat exchanger/cracker (3) that heats and partially decomposes ammonia to be partially burned in the main cracking unit (4) to bring the entire system up to temperature. The ammonia cracker was designed to produce 11.5 kW and was found to consume approximately 3.0 kW to supply heat to the endothermic ammonia decomposition reaction. An alkaline fuel cell (6) was chosen because it is approximately 60.0% efficient and doesn't experience such a large decrease in performance when it is fed with a nitrogen and hydrogen mixture with minute traces of ammonia [7]. For the large ammonia feed flow rates (400.0 L/hr to 800.0 L/hr), the ammonia conversion was found to be the highest at temperatures upwards of 700.0°C for all five catalysts explored. Due to the endothermic nature of the ammonia decomposition reaction, the increase ammonia flow rate for a fixed cracker temperature resulted in increased heat transfer from the heater tubes to the packed bed in the entry region of the cracker. This resulted in non – isothermal operation and a temperature profile with a minimum point in the entry region of the cracker as in [11].

## 3.2 Kinetic Models for Ammonia Decomposition

In this section, the governing kinetic models for ammonia decomposition will be discussed. The Power Rate Law model and the model of Tymken – Pyzhev are presented with relevant differences and mathematical equations.

### 3.2.1 The Power Rate Law

The Power Rate Law for chemical reaction is the basic model for chemical reaction rates. It is thoroughly discussed in [31]. The equation developed for the net rate of reaction was modeled as a simple difference between the forward and reverse reaction rates.

$$r_{net} = r_{fwd} - r_{rev} \quad (3.1)$$

Here, the first term represents the forward reaction and can be described as a product of the forward rate constant and the concentrations of the reactants raised to their stoichiometric coefficients. The forward rate constant is determined by an Arrhenius equation. Similar logic holds true for the reverse reaction. It can be modeled as a product of the reverse rate constant and the concentrations of the products raised to their stoichiometric coefficients. The reverse reaction constant can be modeled as a quotient of the forward reaction rate constant and the equilibrium constant. Applying these to a generic chemical reaction, the following equations were obtained.

$$r_{net} = k^+([A]^a[B]^b) - k^-([C]^c[D]^d) \quad (3.2)$$

$$K_{eq} = \frac{k^+}{k^-} \quad (3.3)$$

When Eq. 3.3 was solved for  $k^-$  and substituted backwards into Eq. 3.2, the following equation for the overall reaction rate was derived.

$$r_{net} = k^+([A]^a[B]^b) - \frac{1}{K_{eq}}([C]^c[D]^d) \quad (3.4)$$

### 3.2.2 The Model of Tymken – Pyzhev

In the late 1930's, the researchers Tymken and Pyzhev attempted to thoroughly understand the kinetic mechanisms in ammonia synthesis and decomposition. Initially this effort had great success in explaining the kinetic data available at the time. However, as time went on and more researchers did more work in the area; they had shown that the work of Tymken – Pyzhev was

insufficient to explain the plethora of intermediate steps occurring in ammonia decomposition. When one applies this to a gas phase reaction such as ammonia decomposition or synthesis it becomes a function of partial pressures of the products and reactants as well as a function of the equilibrium constant [31, 32]. It can be written as follows:

$$r_{net} = k^+ \left[ \left( \frac{P_{NH_3}^3}{P_{H_2}^2} \right)^\beta - \left( \frac{P_{N_2}}{K_{eq}^2} \right) \left( \frac{P_{H_2}^2}{P_{NH_3}^3} \right)^{1-\beta} \right] \quad (3.5)$$

Here, one can see that the reaction rate is heavily influenced by high ammonia partial pressures and/or low hydrogen partial pressures. The exponential  $\beta$  term in the equation is introduced to compensate for any deviance from a “perfect” reaction. For iron based catalysts,  $\beta = 0.25 - 0.60$ . The reverse reaction is often neglected in cases where the reaction is far removed from equilibrium. This assumption can be applied in membrane reactors operating at high temperature and pressure with low hydrogen partial pressures due to hydrogen removal [15,18, 31]. With that in mind, Eq. 3.2 can be slightly modified as follows:

$$r_{net} = k_o e^{-\left(\frac{E_a}{RT}\right)} \left( \frac{P_{NH_3}^3}{P_{H_2}^2} \right)^\beta \quad (3.6)$$

Ammonia decomposition is endothermic with an approximate standard enthalpy of reaction of 46.4 kJ/mol. While the ammonia synthesis reaction favours high pressure and not high temperature, the ammonia decomposition reaction works in the reverse fashion. It favours high temperature and not high pressure [31]. Here in lies the problem, according to Eq. 3.6 the reaction rate favours high ammonia partial pressures and low hydrogen partial pressures. On the other hand, the nature of the reaction does not favour high pressure at all. That being said, there are limitations on the applicability of the Tymken – Pyzhev model. High temperatures upwards of 550.0°C to 600.0°C show negligible inhibitive effects of increasing hydrogen partial pressure. The results of this are shown in [17,18].

### 3.2.3 Comparison of SMR, CH<sub>3</sub>OH, and NH<sub>3</sub> Reactions from First Principles

In this section, the power rate model and the Tymken – Pyzhev model are combined and employed to determine rate equations for the three reactions considered. Due to the system under investigation being a membrane reactor that selectively removes hydrogen from the product stream. Therefore, an acceleration of the forward reaction rate is expected via Le Chatalier’s Principle. There is a variable introduced in this section to account for hydrogen extraction or

“draw”. This is the unique and attractive attribute which separates the membrane reactor from the simple batch reactor. A simple block diagram is constructed to show the chemical flows into and out of the reactor for the batch reactor initially. It is then modified with the hydrogen extraction ratio and boundary cases are used to test and confirm its validity. Finally, EES is used to model the reaction rates and trans – membrane pressure drops as a function of hydrogen extraction factor for selected isotherms.

There are three reactions under investigation. These are listed in the table below with their standard enthalpies of reaction and typical operating temperatures.

Table 3.2: Various chemical reactions for thermal H<sub>2</sub> production

Reaction	Chemical Equation	Standard Enthalpy of Reaction (kJ/mol)	Operating Temperatures (K)
Ammonia Decomposition	$\text{NH}_3 \rightarrow 0.5\text{N}_2 + 1.5\text{H}_2$	45.90 <sup>a</sup>	673.0 – 873.0
Methanol Reforming	$\text{CH}_3\text{OH} + \text{H}_2\text{O} \rightarrow \text{CO}_2 + 3\text{H}_2$	131.70 <sup>a</sup>	400.0 – 570.0
Steam Methane Reforming	$\text{CH}_4 + 2\text{H}_2\text{O} \rightarrow \text{CO}_2 + 4\text{H}_2$	164.70 <sup>a</sup>	973.0 – 1173.0

<sup>a</sup>: Source: Chorkendorff and Niemantsverdriet [31]

A simple block diagram for a chemical reactor is illustrated below with inward and outward flows. Moreover, the “hydrogen extraction ratio” is introduced and defined. Both batch and membrane reactors are introduced. The major differences between them are also explained in subsequent paragraphs.

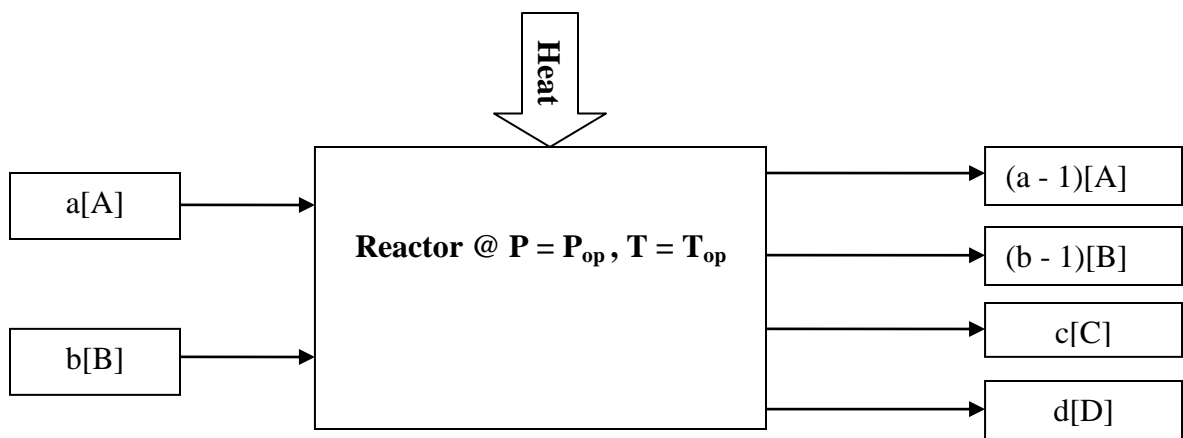


Figure 3.4: Batch reactor for an arbitrary chemical reaction.

In Figure 3.4, the reactor is shown as a “black box” in which  $a + b$  moles of reactant enter and decompose according to their respective chemical equation. The reaction is constrained by the outputs being fixed by their respective stoichiometric constants. That being said, this case only represents when there is no hydrogen is being removed via a membrane. To accommodate for this, a new variable is introduced: the “hydrogen extraction ratio” ( $x$ ). This variable is used to mathematically investigate the effect of selective product extraction on chemical reaction rate, chemical equilibrium constant, and trans – membrane pressure drop. Figure 3.4 is modified below to illustrate how the new variable integrated into the system.

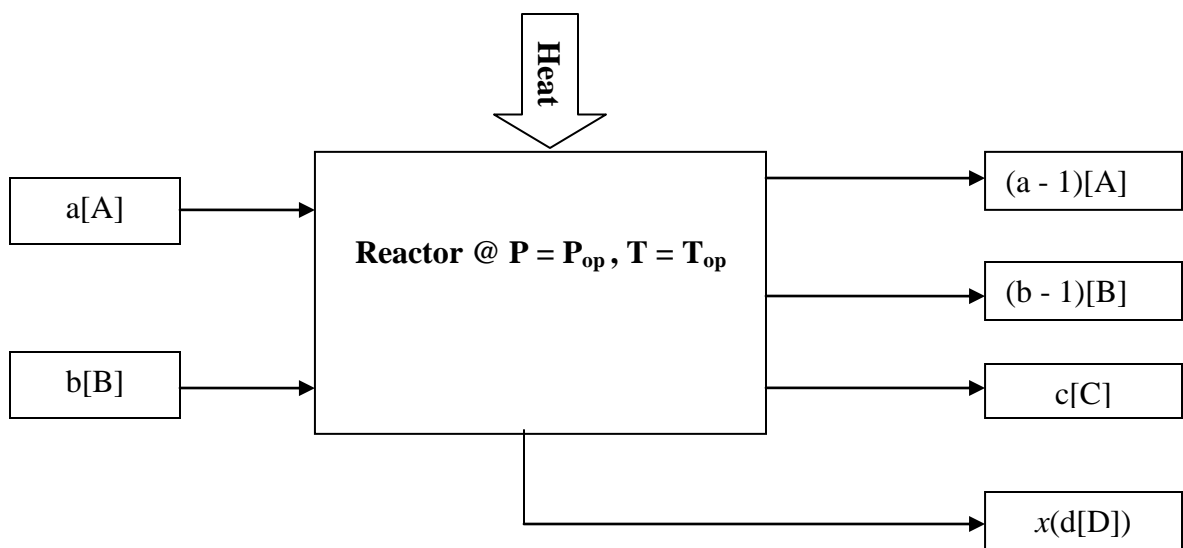


Figure 3.5: Membrane reactor for an arbitrary chemical reaction.

This type of approach needs some verification in the form of numerical consistency. If the total number of moles for zero extraction matches the total number of moles for the batch case, then the total number of moles for the membrane case must also be true by analogy. By consequence, the variable chosen is a valid one because it's not violating any conservation laws. The boundary cases are given as follows:

- When  $x = 0$ , there is no hydrogen removal and the total number of moles corresponds to that of the batch reactor case.
- When  $0 < x < 1$ , there is a linear increase in hydrogen removal and the total number of moles corresponds to the membrane reactor case.

For the three reactions mentioned in Table 3.2, the total number of moles for the membrane case had been determined in this fashion. These are listed in Table 3.3.

Table 3.3: Total number of moles ( $n_{tot}$ ) for the membrane reactor case

Reaction	Total number of moles ( $n_{tot}$ )
Ammonia Decomposition	$n + 1.5x - 0.5$
Methanol Reforming	$2n - 1 + 3x$
Steam Methane Reforming	$3n - 2 + 4x$

When the Power Rate Law and the Tymken – Pyzhev model was applied to the three reactions mentioned in Table 3.2, the following three equations were derived based on a balance of forward and reverse reaction rates [31].

$$r_{NH_3} = k \left[ \left( \frac{P_{NH_3}}{(1-x)P_{H_2}^{1.5}} \right) - \left( \frac{P_{N_2}^{0.5}}{K_{eq}} \right) \left( \frac{(1-x)P_{H_2}^{1.5}}{P_{NH_3}} \right) \right] \quad (3.7)$$

$$r_{CH_3OH} = k \left[ \left( \frac{P_{CH_3OH}P_{H_2O}}{(1-x)P_{H_2}^3} \right) - \left( \frac{1}{K_{eq}} \right) \left( \frac{(1-x)P_{H_2}^3 P_{CO_2}}{P_{CH_3OH}P_{H_2O}} \right) \right] \quad (3.8)$$

$$r_{CH_4} = k \left[ \left( \frac{P_{CH_4}P_{H_2O}^2}{(1-x)P_{H_2}^4} \right) - \left( \frac{1}{K_{eq}} \right) \left( \frac{(1-x)P_{H_2}^4 P_{CO_2}}{P_{CH_4}P_{H_2O}^2} \right) \right] \quad (3.9)$$

$$k = k_o e^{-\left(\frac{E_a}{RT}\right)} \quad (3.10)$$

Here, the forward reaction rate constant is described in Eq. 3.10. Data for pre –exponential factor and activation energy were taken from relevant literature sources. These are listed in Table 3.4 with their respective sources.

Table 3.4: Sample activation energies and pre – exponential factors

Reaction	Activation Energy (kJ/mol)	Pre – Exponential Factor
Ammonia Decomposition <sup>b</sup>	$196.0 \times 10^3$	$2.098 \times 10^6$
Methanol Reforming <sup>c</sup>	$115.0 \times 10^3$	$6.0 \times 10^8$
Steam Methane Reforming <sup>d</sup>	$240.0 \times 10^3$	$1.172 \times 10^{12}$

<sup>b</sup>: Source: Hellgardt et al. [32] <sup>c</sup>:Source: Spivey [33] <sup>d</sup>:Source: Levent et al. [34]

The anticipated effect of product removal is a decrease in overall product partial pressure. By Le Chatelier’s Principle, the overall reaction rate is expected to increase.

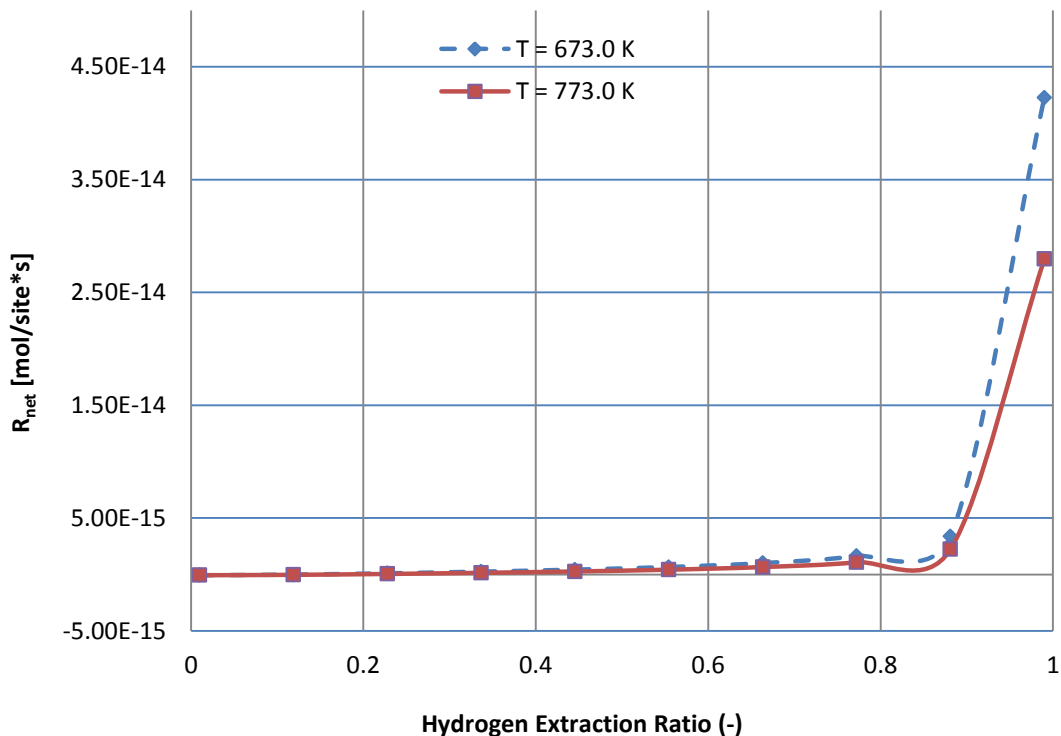


Figure 3.6: NH<sub>3</sub> decomposition rate vs. H<sub>2</sub> extraction ratio at 20.0 bar.

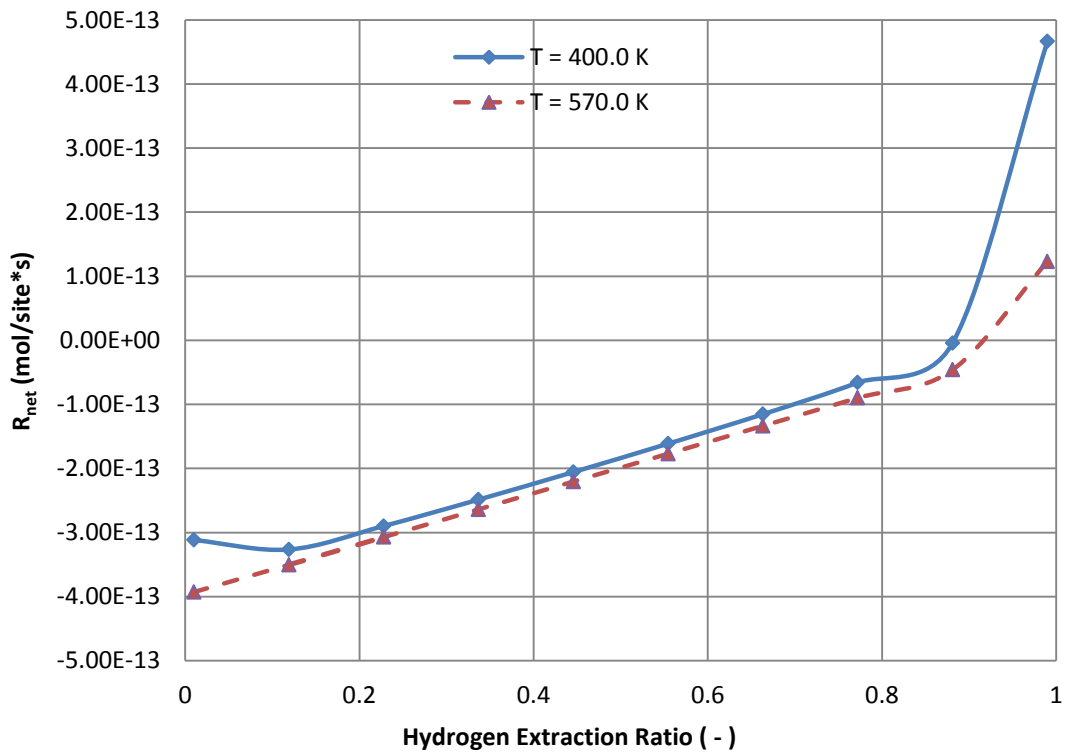


Figure 3.7: CH<sub>3</sub>OH reaction rate vs. H<sub>2</sub> extraction ratio at 20.0 bar.

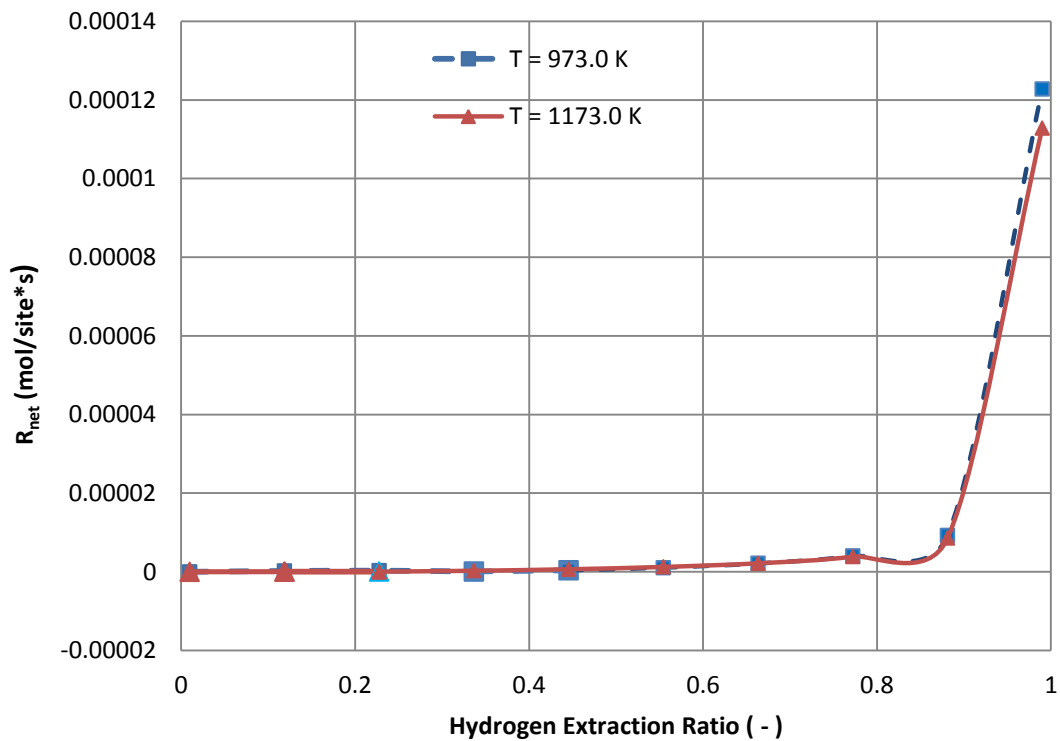


Figure 3.8: SMR reaction rate vs. H<sub>2</sub> extraction ratio at 20.0 bar.

Figures 3.6 – 3.8 illustrate the reaction rates of three reactions listed in Table 3.2. It can clearly be seen that as hydrogen is removed from the product stream via a membrane, the forward reaction is accelerated. The negative values of reaction rate on the graphs indicate that the reverse reaction is favoured. On the other hand, the positive values of reaction rate on the graphs indicate that the forward reaction is favoured. The ammonia decomposition and steam methane reforming reactions are greatly accelerated with hydrogen removal. These results are in agreement with Le Chatalier's principle. The initial decrease in methanol reforming rate would most likely be due to the Gibb's free energy at 400.0 K initially increasing slightly at low hydrogen extraction ratios and then decreasing as the hydrogen extraction ratio increases. In thermodynamic terms, this is due to what is known as the Gibb's free energy. A reaction is said to be thermodynamically favourable if the Gibb's free energy is less than zero. When the Gibb's free energy is greater than zero, the converse is true and a reaction is said to be thermodynamically unfavourable. The chemical equilibrium occurs when the forward and reaction rates have asymptotically approached the same value and are equal. In thermodynamic terms, when the Gibb's free energy is zero, then a reaction is said to be in chemical equilibrium. Finally, the ammonia decomposition reaction has the lowest standard Gibb's free energy of -16.4 kJ/mol. When compared to the methanol and steam methane reforming reactions, which have standard Gibb's free energies of +3.5 kJ/mol and +113.4 kJ/mol, respectively [31]. Due to this, the ammonia decomposition reaction is much more favourable thermodynamically than the other two. This type of behaviour also occurred in the outputs of the EES code. The sample outputs for the temperature ranges considered are listed in Table 3.5.

Table 3.5: Sample Gibb's free energies for three chemical reactions

Reaction	Chemical Equation	Range of Gibb's Free Energies (kJ/mol)	Range of Operating Temperatures (K)
Ammonia Decomposition	$\text{NH}_3 \rightarrow 0.5\text{N}_2 + 1.5\text{H}_2$	-3.621 – -8.087	673.0 – 773.0
Methanol Reforming	$\text{CH}_3\text{OH} + \text{H}_2\text{O} \rightarrow \text{CO}_2 + 3\text{H}_2$	+25.723 – +16.429	400.0 – 570.0
Steam Methane Reforming	$\text{CH}_4 + 2\text{H}_2\text{O} \rightarrow \text{CO}_2 + 4\text{H}_2$	+12.182 – -4.982	973.0 – 1173.0

When Figures 3.6 – 3.8 were analyzed in light of the information in Table 3.5, the behaviour of the reaction rates and the apparent tipping point in hydrogen draw where the forward reaction becomes favoured over the reverse reaction and begins to accelerate became clarified. Since the ammonia decomposition reaction is more thermodynamically favourable than either methanol or steam methane reforming, the required reduction of hydrogen partial pressure to accelerate the forward reaction is less. The methanol reforming reaction is strongly thermodynamically unfavourable and as such the required reduction in hydrogen partial pressure to accelerate the forward reaction is high. The steam methane reforming reaction presents an interesting case with transitional behaviour where an initially unfavourable ( $G > 0$ ) reaction passes through equilibrium ( $G = 0$ ) by increased temperature and the forward reaction becoming favourable ( $G < 0$ ). The effect of passing over the equilibrium point is shown by the decrease in required hydrogen removal for forward reaction acceleration.

At this point we are faced with a conundrum. Firstly, the reduction of hydrogen partial pressure has been shown to accelerate reaction rates by decreasing the Gibb's free energies for all three reactions. Secondly, the removal of hydrogen has been shown to increase conversion rates and reactor efficiencies as in [11, 12, 14, 15]. Finally, one major benefit with membrane reactors is that while 100.0% hydrogen recovery is not possible, membrane reactors still produce higher hydrogen recovery numbers in comparison to batch reactors [15]. In this case removal of hydrogen causes a reduction in hydrogen partial pressure and ergo, a reduction in driving force

for hydrogen recovery. This problem was mentioned in [15] where only approximately 80.0% of the hydrogen was recovered during the reforming of methanol. If one was to calculate the pressure drop across the membrane as a function of the hydrogen draw factor, the equation would look as follows:

$$\Delta P_{tm} = P_{H_2} * (1 - x) - 1 \quad (3.11)$$

This was applied to all three reactions under consideration and was used to determine the maximum trans – membrane pressure drop and maximum possible hydrogen recoveries as a percentage. The results from this numerical simulation are depicted in Figures 3.9 through 3.11.

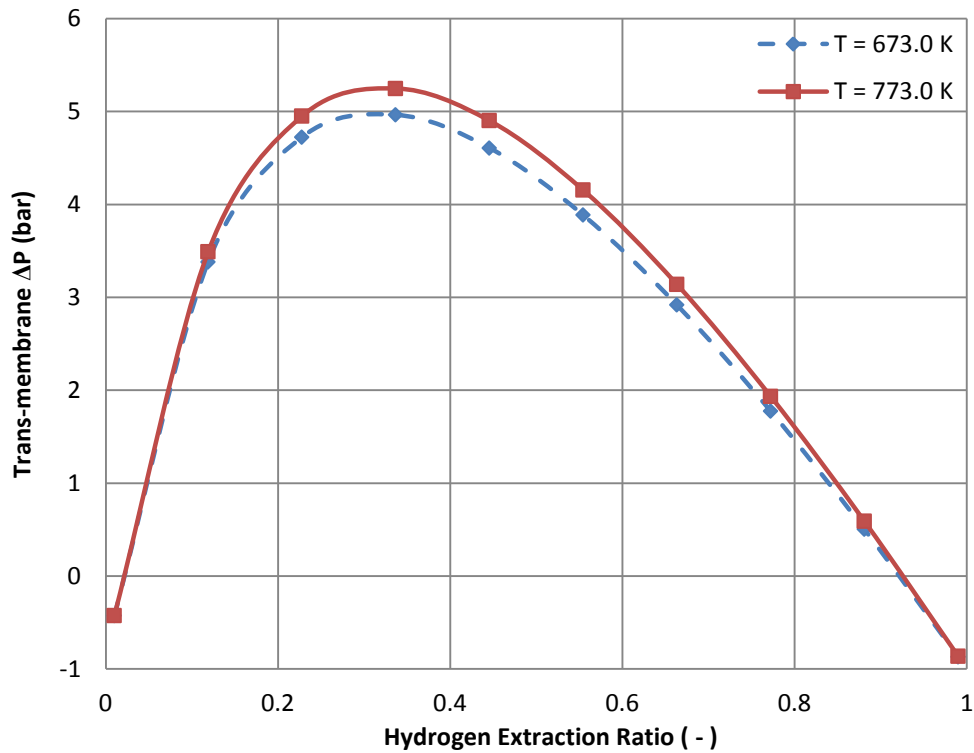


Figure 3.9: Trans – membrane ΔP vs. H<sub>2</sub> extraction ratio for the NH<sub>3</sub> decomposition reaction at 20.0 bar.

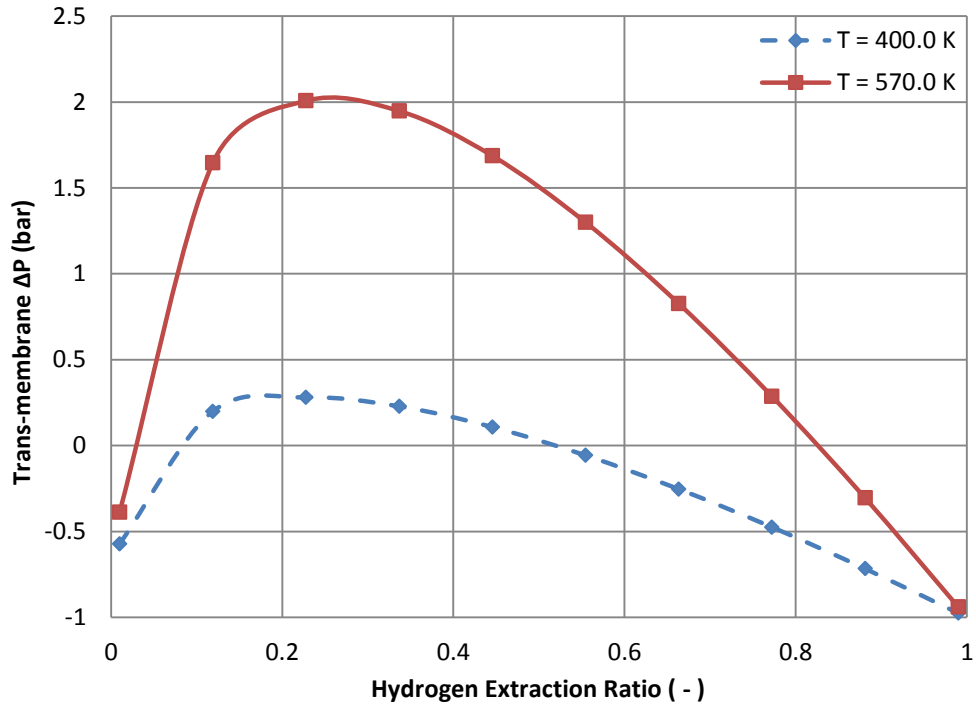


Figure 3.10: Trans – membrane  $\Delta P$  vs.  $H_2$  extraction ratio for the  $CH_3OH$  reforming reaction at 20.0 bar.

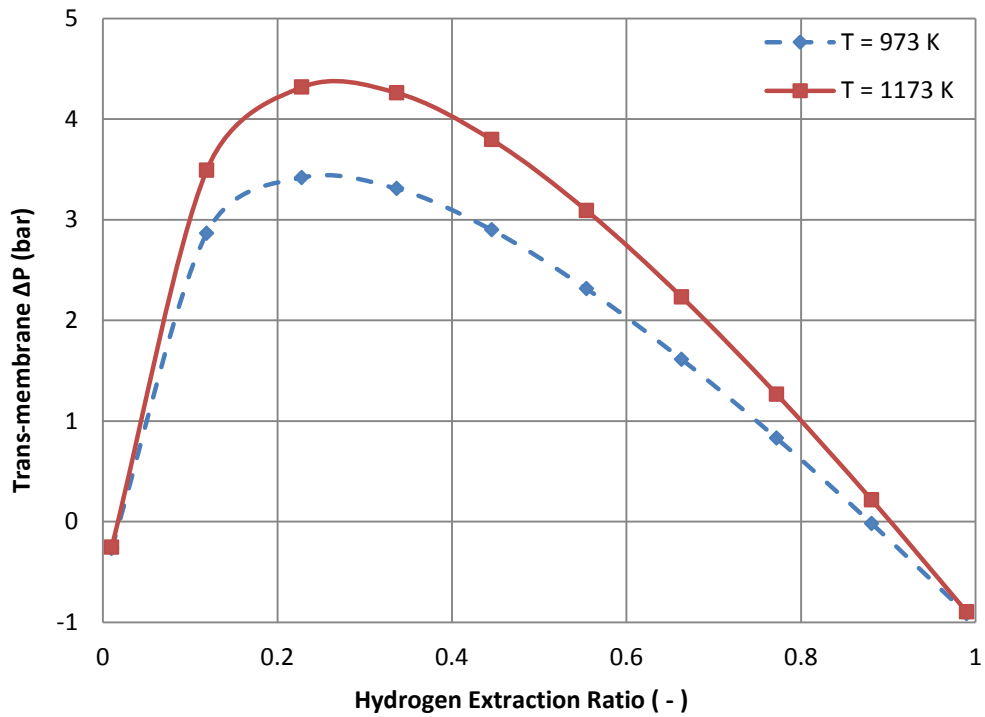


Figure 3.11: Trans – membrane  $\Delta P$  vs.  $H_2$  extraction ratio for the SMR reaction at 20.0 bar.

The maximum pressure drops were determined by taking the derivative of the fitted equations in Figures 3.9 – 3.11, setting them to zero and solving them. The maximum hydrogen recoveries were determined by solving the fitted equations in Figures 3.9 – 3.11 for their zeroes and taking the largest value. These results are tabulated and shown below.

Table 3.6: Maximum H<sub>2</sub> recovery and trans – membrane pressure drop for NH<sub>3</sub> decomposition reaction

<b>Temperature (K)</b>	<b>Maximum Hydrogen Recovery (%)</b>	<b>Maximum Trans – Membrane Pressure Drop (bar)</b>
673.0	92.0	4.964 at 33.67 % extraction
773.0	92.5	5. 248 at 33.67 % extraction

Table 3.7: Maximum H<sub>2</sub> recovery and trans – membrane pressure drop for CH<sub>3</sub>OH reforming reaction

<b>Temperature (K)</b>	<b>Maximum Hydrogen Recovery (%)</b>	<b>Maximum Trans – Membrane Pressure Drop (bar)</b>
400.0	50.0	0.281 at 22.78 % extraction
570.0	82.1	2.007 at 28.09% extraction

Table 3.8: Maximum H<sub>2</sub> recovery and trans – membrane pressure drop for SMR reaction

<b>Temperature (K)</b>	<b>Maximum Hydrogen Recovery (%)</b>	<b>Maximum Trans – Membrane Pressure Drop (bar)</b>
973.0	87.6	3.418 at 22.9 % extraction
1173.0	90.1	4.313at 22.7% extraction

Figures 3.9 – 3.11 illustrate a critical point about membrane reactor performance. If the reactor was viewed exclusively through the lens of Le Chatalier's principle, one would simply assume that 100.0% hydrogen recovery is the best possible outcome for both speeding up the forward reaction rate and hydrogen production. However, there is a mathematical balance between hydrogen recovery and trans – membrane pressure drop. As hydrogen is removed, the hydrogen partial pressure decreases and the reaction rate increases to compensate. However, the decrease in hydrogen partial pressure due to increasing the hydrogen draw causes the trans – membrane pressure drop and by extension the hydrogen flux.

An interesting point to mention is the physical significance of the zeroes in Figures 3.9 through 3.11. The upper zeroes illustrated an upper limit on hydrogen extraction ratio that states that it is physically impossible to remove 100% of the hydrogen from the reactor because the hydrogen partial pressure in the reactor becomes less than the shell pressure. Due to this, hydrogen flux cannot physically happen. However, if a hydrogen compressor was to draw vacuum on the shell side then it could be possible to remove 100% of the hydrogen from the reactor. However, doing that may generate a second problem. With no hydrogen on the membrane walls, other gases would form a layer that would impede path of the hydrogen to the membrane and could potentially result in decreased hydrogen production. That being said, the lower zero is a physical impossibility. It implies a backward flow of hydrogen from the shell side into the reactor. However, there was no hydrogen at high pressure in the shell side initially to allow for this to happen. Moreover, the shell side was defined as an open system at 1.0 bar and is unable to accumulate hydrogen in order to increase the pressure to force a backwards flow at low hydrogen extraction ratios.

All things considered, the ammonia decomposition reaction conducted in a membrane reactor seemed to be the best choice when compared to methanol reforming or steam methane reforming. The ammonia decomposition reaction exhibited the greatest potential hydrogen recovery and it is thermodynamically favourable due to its high spontaneity and its relatively low enthalpy of reaction compared to the competing reactions. Another interesting feature about the ammonia decomposition reaction is that the reaction rate is steadier for a greater range of hydrogen extraction ratios. This was indicated by the plateau that forms as the hydrogen draw approaches 100.0%. This was determined to be a desirable behaviour because it showed low

sensitivity of reaction rate to changes in hydrogen extraction. One such change would be membrane permeability changing with temperature. Finally, the differences in trans – membrane pressure drops between the two temperatures are at a minimal for the ammonia decomposition reaction. This illustrated a relatively constant trans – membrane pressure drop with changes in temperature.

### 3.3 Modeling the Equilibrium Shift Associated with Hydrogen Removal

As previously mentioned, the effect of reducing hydrogen partial pressure in the products will cause the reaction to go further forward by Le Chatalier’s principle. In this section, the effect of hydrogen removal on the equilibrium concentrations is determined by employing the hydrogen extraction variable. A computer code was written in the EES software to determine all relevant thermodynamic and physical properties. With this data, concentration profiles are generated and some conclusions are also made in this regard.

#### 3.3.1 Comparison of SMR, CH<sub>3</sub>OH, and NH<sub>3</sub> Reactions from First Principles

More often than not, chemical reactions are far removed from equilibrium. Due to this, the reverse reaction must be accounted for [31, 32]. At chemical equilibrium, the Gibb’s free energy becomes zero and the forward and reverse reaction rates are asymptotically approaching the same value. In this special case, the reaction has gone as far to completion as possible. This was seen as an absolute upper limit for production from a chemically reactive system. Due to the change in the total number of moles because of hydrogen removal, the concentration profiles are quite different. As previously mentioned, this type of approach requires some verification. The sum of all concentrations should equal unity and therefore, the checking criterion is as follows:

$$1.0 = \frac{1}{n_{tot}} \sum_{i=1}^j c_i \quad (3.12)$$

The Gibb’s free energy was calculated in terms of equilibrium constant and then set to zero and solved by the EES software. The following equations were used to model the concentration profiles as a function of hydrogen extraction ratio:

$$\text{Change in Gibb’s Free Energy: } dG(T, P) = dH(T) - T * dS(T, P) \quad (3.13)$$

$$\text{Change in Entropy: } dS(T, P) = S_{(T,P)} - S_{(T_0,P_0)} \quad (3.14)$$

Entropy at (T, P): 
$$S_{(T,P)} = R * T * \ln(K_{eq} * \frac{P}{P_0}) \quad (3.15)$$

Equilibrium Constant: 
$$K_{eq}(T) = \frac{[C]^c * [D]^d}{[A]^a * [B]^b} \quad (3.16)$$

By combining Eqs. 3.12 through 3.16 together, setting the Gibb's free energy expression to zero and then writing them in EES as a function of their thermo - physical properties yields concentration profiles for the ammonia decomposition reaction, methanol reforming reaction and steam methane reforming reaction as a function of hydrogen extraction ratio for the applicable temperature and pressure ranges. These results are depicted below in Figures 3.12 – 3.14.

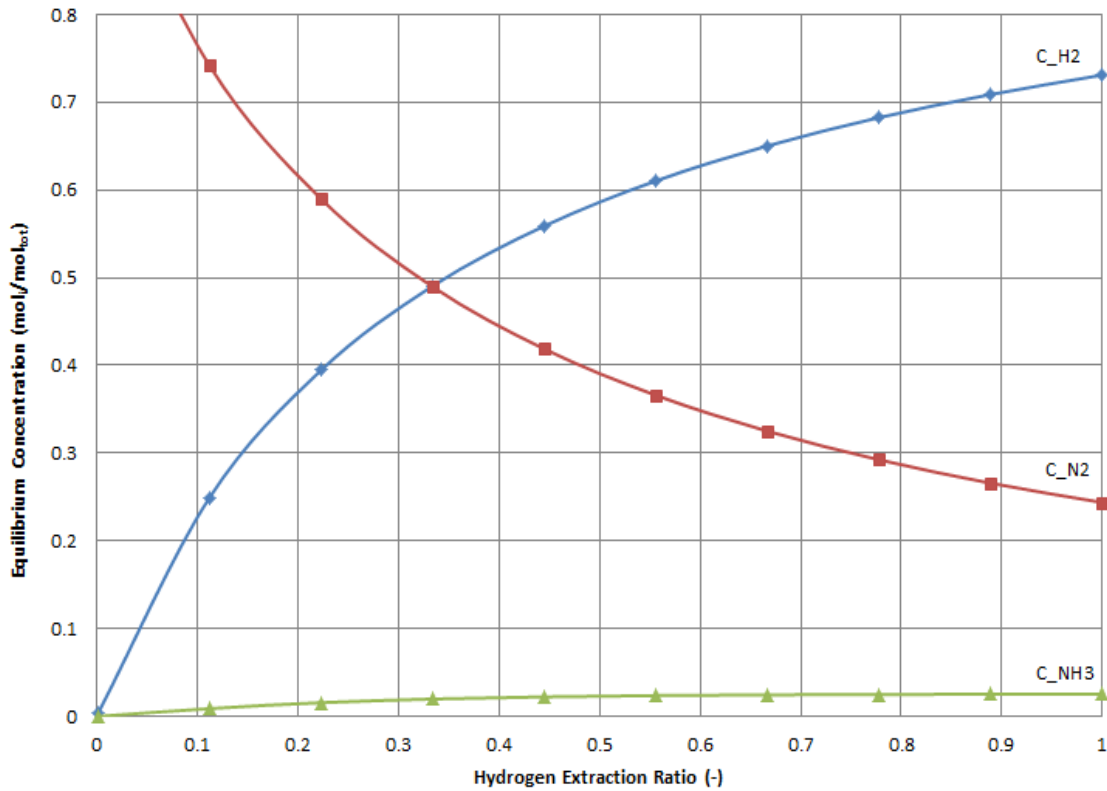


Figure 3.12: Equilibrium concentration vs. H<sub>2</sub> extraction ratio NH<sub>3</sub> decomposition reaction.

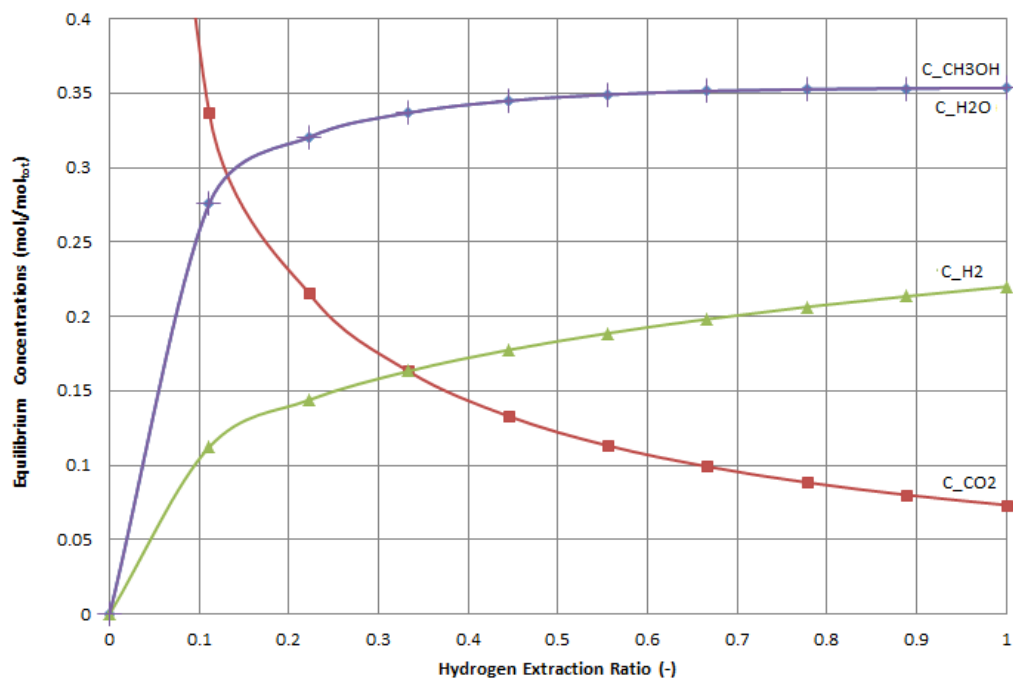


Figure 3.13: Equilibrium concentration vs. H<sub>2</sub> extraction ratio for CH<sub>3</sub>OH reforming reaction.

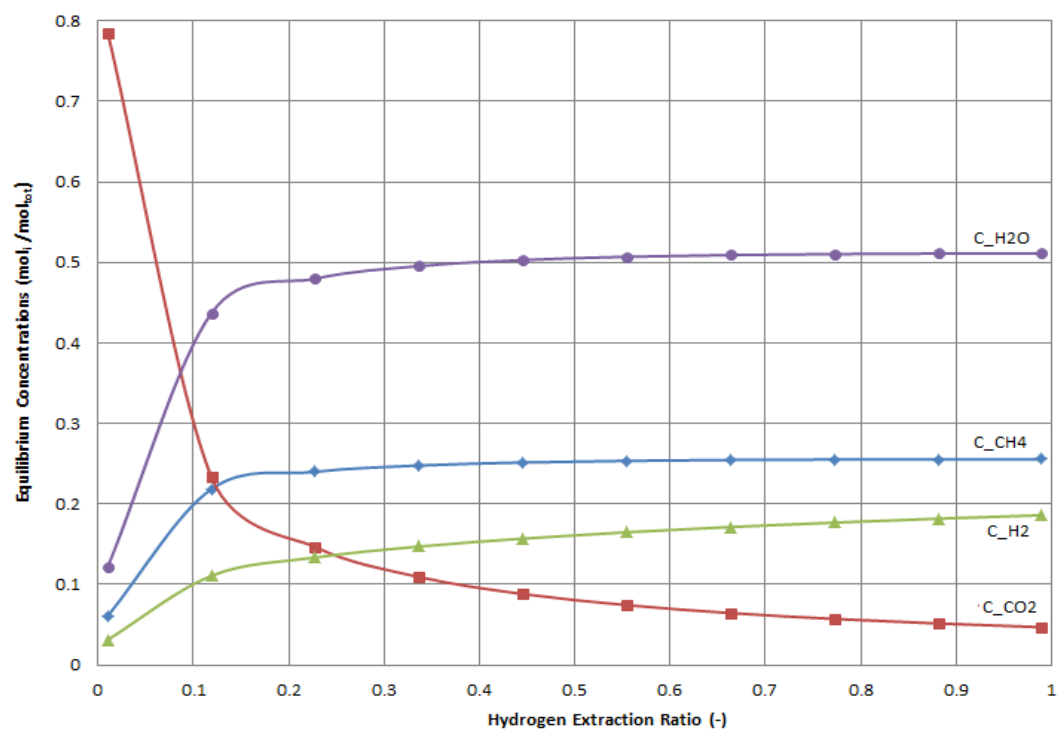


Figure 3.14: Equilibrium concentration vs. H<sub>2</sub> extraction ratio for SMR reaction.

Figures 3.12 – 3.14 illustrate the equilibrium concentrations for the ammonia decomposition, methanol reforming, and SMR reaction. Despite the reactions being different, there is one common thread between all three. The removal of hydrogen positively influences the forward reaction. Due to this, the equilibrium concentration of hydrogen increases for the reactions examined. Figures 3.12 – 3.14 are directly compared to draw some conclusions about the effect of hydrogen removal on relative concentrations in each reaction it can be clearly seen that every reaction except the ammonia decomposition reaction has a significant increase in reactant concentration associated with increased hydrogen draw. When one compares the three reactions, one notices that the SMR and methanol reforming reactions both produce carbon dioxide and have a greater fraction of their equilibrium concentration devoted to reactants than products. Conversely, the ammonia decomposition reaction heavily favours hydrogen production and even more so when hydrogen removal via a membrane reactor is taken into consideration. Mole for mole, the ammonia decomposition reaction has proven to be a more efficient reaction that converts an overwhelming majority of its reactant into products and one which produces no carbon dioxide. Additionally, by simply dividing the enthalpy of reaction for each of the listed reactions in Table 3.2 by the stoichiometric number of moles of hydrogen produced shows that ammonia decomposition requires only 30.6 kJ/mol<sub>H<sub>2</sub></sub> compared to much larger 41.18 kJ/mol<sub>H<sub>2</sub></sub> or 43.9 kJ/mol<sub>H<sub>2</sub></sub> for SMR and methanol reforming, respectively.

### 3.4 Characteristics of Solid Catalysts

Since the experimental work conducted in this thesis was done with a nickel (II) oxide catalyst, it is fitting to mention some characteristics of solid catalysts before delving into the experimental section.

The catalyst chosen was a Ni<sub>2</sub>O<sub>3</sub> catalyst with an  $\alpha$  – Al<sub>2</sub>O<sub>3</sub> support. It is a black coloured powder with particulate sizes ranging from 20.0 – 100.0 mesh. This catalyst was chosen for being relatively cost effective, commercially available, and more effective than competing iron based catalysts. In chapter 5 of [31], solid catalysts are discussed in detail. Some positive attributes about an  $\alpha$  – Al<sub>2</sub>O<sub>3</sub> support were briefly mentioned. These are re – iterated in the list below:

- controlled surface area and porosity;
- high thermal stability;
- high mechanical strength against crushing and attrition.

Gases that are adsorbed on an oxide catalyst surface after heterolytic disassociation. On an oxide surface, the metal cation acts as an electron acceptor and the oxide anion acts as a proton acceptor. Moreover, oxides are effective catalysts due to their minimal surface free energy. Oxides have a lower surface free energy than metals but higher than hydrocarbons. More specifically, since Ni<sub>2</sub>O<sub>3</sub> is a FCC crystal structure the number of free neighbours in a surface tends to be maximized. Water easily disassociates and adsorbs on an oxide surface as a proton and a hydroxide ion. To illustrate this point, an example of this will be applied to methanol reforming. For all intensive purposes, the SMR reaction is to be treated the same as the methanol reforming reaction due to the same water – gas shift reaction occurring. Afterwards, a similar approach is used to further understand the ammonia decomposition reaction. The methanol reforming reaction is to be treated as the summation of a methanol decomposition reaction and the water – gas shift reaction. As a series of two chemical reactions, the overall chemical equation, it would look as follows:



In the water – gas shift reaction, the water disassociates upon contact with the oxide surface into a proton (H<sup>+</sup>) and a hydroxide ion (OH<sup>-</sup>). Furthermore, both hydroxide ions in the methanol decomposition and water - gas shift reactions disassociate into two oxygen ions (O<sup>-2</sup>) and two protons (H<sup>+</sup>). The methyl cation (CH<sub>3</sub><sup>+</sup>) loses three protons (H<sup>+</sup>) to surface sites due to heterolytic adsorption of hydrogen on the nickel oxide surface which leaves a carbon ion (C<sup>-4</sup>). A simple balance and recombination of ions is responsible for the formation of the products.

A similar yet different process occurs for ammonia decomposition. The difference is that the reaction is a purely gas phase reaction and there is no secondary reaction that occurs that is analogous to the water – gas shift reaction in either methanol reforming or SMR. Smedarchina et al. [35] conducted a first principles study of ammonia decomposition on silicon dimers and had

experimentally determined that the nitrogen was bonded to the silicon and the hydrogen was free. This was primarily due to a greater difference in electronegativity between silicon and nitrogen as opposed to hydrogen and silicon. When the ammonia decomposition reaction is applied over a  $\text{Ni}_2\text{O}_3$  catalyst, a slightly different approach was taken. Since the difference in electronegativity between oxygen and hydrogen is greater than the difference in electronegativity for oxygen and nitrogen, the ammonia decomposition reaction over a  $\text{Ni}_2\text{O}_3$  catalyst can be displayed as below.

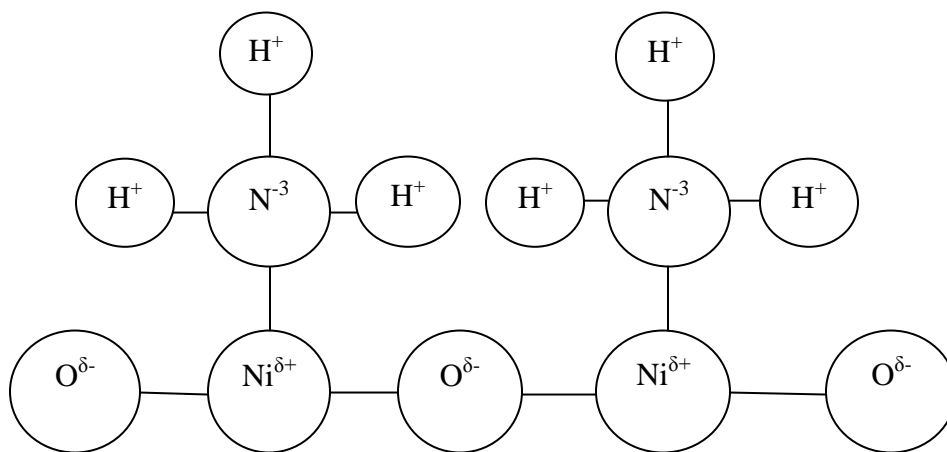


Figure 3.15:  $\text{NH}_3$  decomposition reaction on  $\text{Ni}_2\text{O}_3$  catalyst surface (adapted from [31]).

Due to the greater difference in electronegativity between hydrogen and oxygen than nitrogen and hydrogen or hydrogen and nickel, the oxygen kind of serves as a “hydrogen magnet” that pulls hydrogen off the nitrogen which allows them to form into hydrogen gas. The nitrogen ions then re - combine to form a triple bond and become nitrogen gas.

## Chapter 4: Experimental Works

In this chapter, the main experimental setup is introduced and explained. A process diagram for the main experimental setup is presented with labels and all relevant information. The objective of this experimental work is to successfully decompose ammonia over a  $\text{Ni}_2\text{O}_3$  catalyst in a membrane reactor for the production of hydrogen. A schematic of the main experimental setup is illustrated in Figure 4.1. The system will first be operated with nitrogen to safely determine the existence of any leakages. The operating temperature and pressure ranges are between  $400.0^\circ\text{C}$  -  $500^\circ\text{C}$  and 5.0 – 20.0 bar, respectively.

### 4.1 Design of a Membrane Reactor System for Hydrogen Production

Anhydrous ammonia was transferred from the pressurized tank into a 1.0” diameter stainless steel tube that is 18.0” long. It was capped with a 1.0” stainless steel end cap on one end and was reduced on the other end to be fitted with a Swagelok PGI series process pressure gauge and input/output Swagelok 4PT plug valves. It was placed into a 2.0” diameter black pipe that is 20.0” long. This had the appropriate reducing couplings to allow for 0.750” MNPT hose connections from a Neslab RTE – 140 heater/chiller unit to be attached. This circulated an 80:20 mixture of ethylene glycol and water to preheat the ammonia to  $52.0^\circ\text{C}$  and 21.0 bar. This was incorporated into the design to ensure that ammonia could be fed into the reactor at a controlled temperature and pressure. Reactor pressure was controlled by a Swagelok KPR series forward pressure regulator. Flow into the reactor was measured by an Omega FMA – 1812 electronic flow meter that was interfaced with a National Instruments NI – cDAQ9174 data acquisition system. This flow meter had a +/- 1.5% error rating from the factory. Flow out of the reactor was controlled by Swagelok SS – 4MG needle valve. This served as a flow control device to impede flow out of the reactor and to generate backpressure. Heat was supplied to the reactor by an electrical resistance furnace that can be connected in either series or parallel for a power consumption of 0.3 or 1.2 kW, respectively. Due to the hydrogen selective nature of a palladium membrane there were two outlet streams, they are called the hydrogen and raffinate streams, respectively (see Figure 4.1). Sampling ports are on each stream to allow for the potential withdrawing samples of fixed volumes and/or to accommodate for the potential vacuuming of the entire system. An additional two K type thermocouples are installed in both product streams to measure and record their temperatures. Two Omega FL – 5000 series 65.0 mm glass tube flow

meters are installed to measure the flow rates in each product stream. These both have +/- 2.0% error ratings from the factory.

Heat was supplied by a 1.2 kW electrical resistance furnace that used Nichrome wires embedded in the ceramic for heating. The electrical resistance furnace was designed in house and built specifically for this experiment. It consisted of two banks which contain a semicircular array of 13 vertical wires embedded 0.250” deep in dense pourable ceramic that are 2.625”x 5.25”x 18.0”. The banks were then attached to their frames which are then attached via hinges and filled with Rockwool insulation. The entire assembly was then wrapped with approximately 2.0” of Rockwool insulation and piping insulation. All joints were taped with aluminum tape.

Ideally, a uniform temperature distribution along the length of the reactor is required to ensure relatively constant heat transfer to the reactor. This required the controlling of power to the furnace once the temperature reached the set point temperature. Due to this, the electrical resistance furnace is controlled by an Omega CN7523 P.I.D controller that is passed temperature measurements from a 20.0” K type thermocouple placed down the center of the furnace. The entire control system sends furnace on – off signal data to the aforementioned data acquisition system. This data will be integrated and used to determine the power consumption of the furnace during an experimental period by the following relationship:

$$P_{tot}(T, t) = \int_0^t F(T) * dt \quad (4.1)$$

The integrand in Eq. 4.1 was modeled as a unit step function [36] due to the furnace being an open and closed electrical circuit. It was modeled by the following equation:

$$F(T) = \begin{cases} 0 & T_{SV} \geq T \geq 1300 \\ 1 & 0 \leq T \leq T_{SV} \end{cases} \quad (4.2)$$

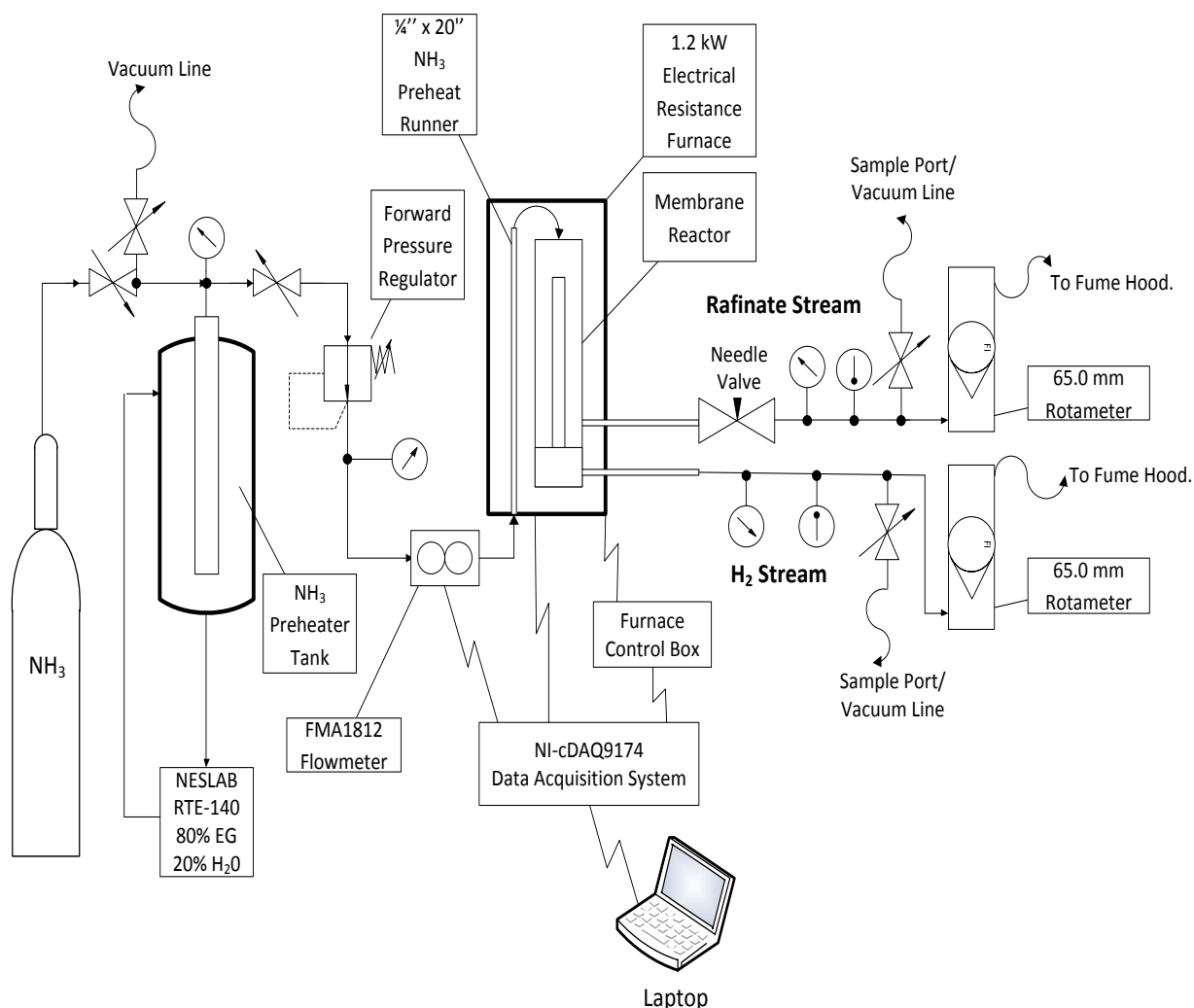


Figure 4.1: Schematic of main experimental setup for H<sub>2</sub> production from NH<sub>3</sub> decomposition.

The experimental system process diagram is shown above in Figure 4.1. The flow was monitored by an Omega FMA1812 flow meter and controlled manually by generating backpressure with a needle valve. The sampling ports were made for being able to either draw vacuum on the system or to extract a sample from either stream. Outward flows were measured by 65.0mm glass tube rotameters. All temperatures were measured with K-type thermocouples and pressures were measured with Swagelok Bourdon tube pressure gauges.

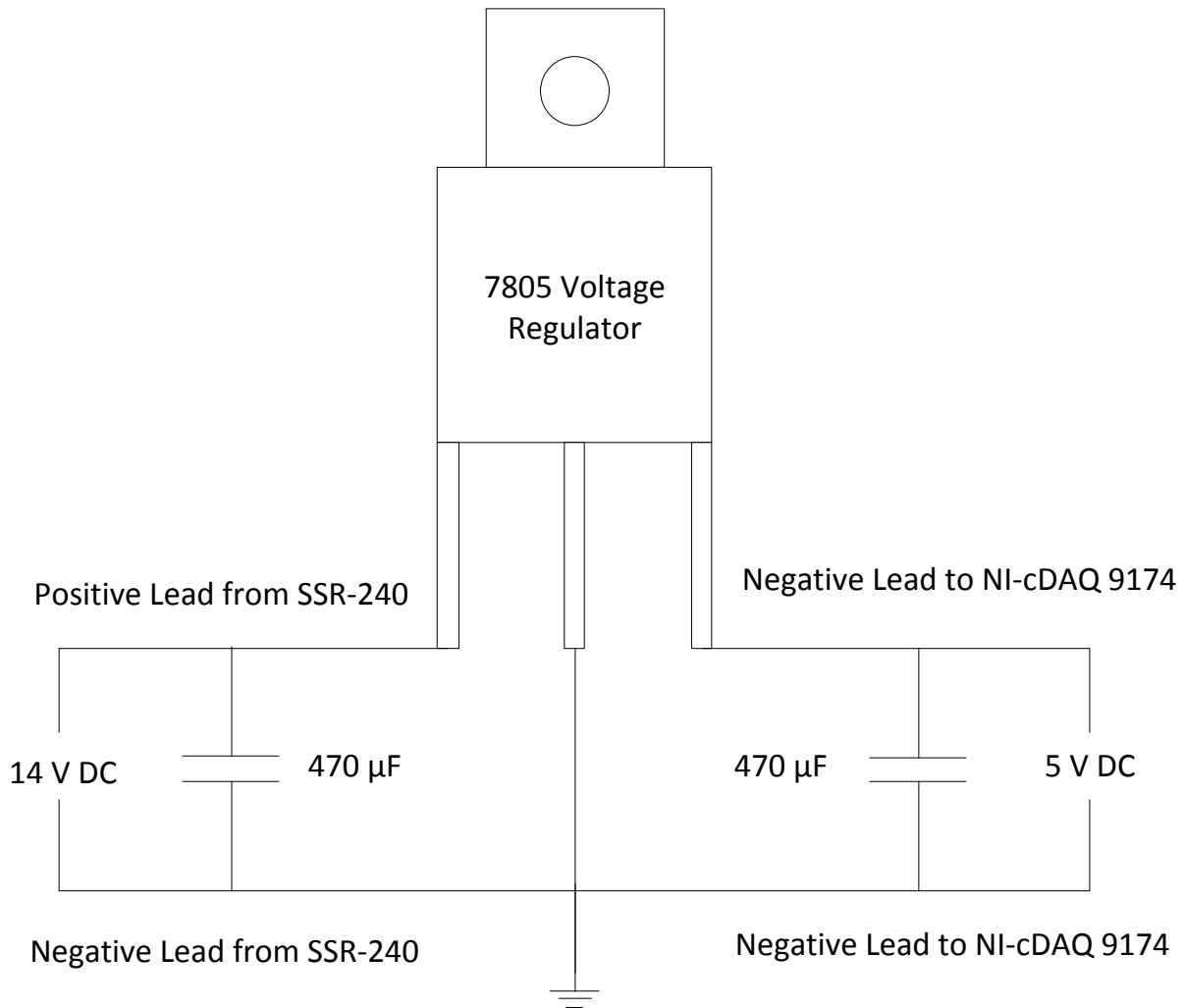


Figure 4.2: Voltage regulator circuit to step 14.0 V DC down to 5.0 V DC.

Figure 4.2 illustrates a voltage regulator circuit with two 470  $\mu\text{F}$  capacitors and electrical leads to the NI – cDAQ9174 data acquisition system. This was done to prevent sending an over voltage to the NI – cDAQ9174 because the control voltage to actuate the solid state relay is in the neighbourhood of 14.0 V DC and the NI – cDAQ9174 has a maximum voltage rating of 10.0 V DC. The voltage regulator circuit dissipated the excess 9.0 V as heat and the signal to the NI – cDAQ9174 was recorded as 5.0 V DC when the furnace is on and as null when the furnace is off. The outputs were then divided by 5.0 to give a nominal value of 1.0 to the “on” position. The “off” position will still register a 0.0 V DC signal. A USB connection between the NI – cDAQ9174 and a laptop served to generate an “on – off” time history of the furnace which will be used in energy and exergy efficiency calculations in Chapter 5.

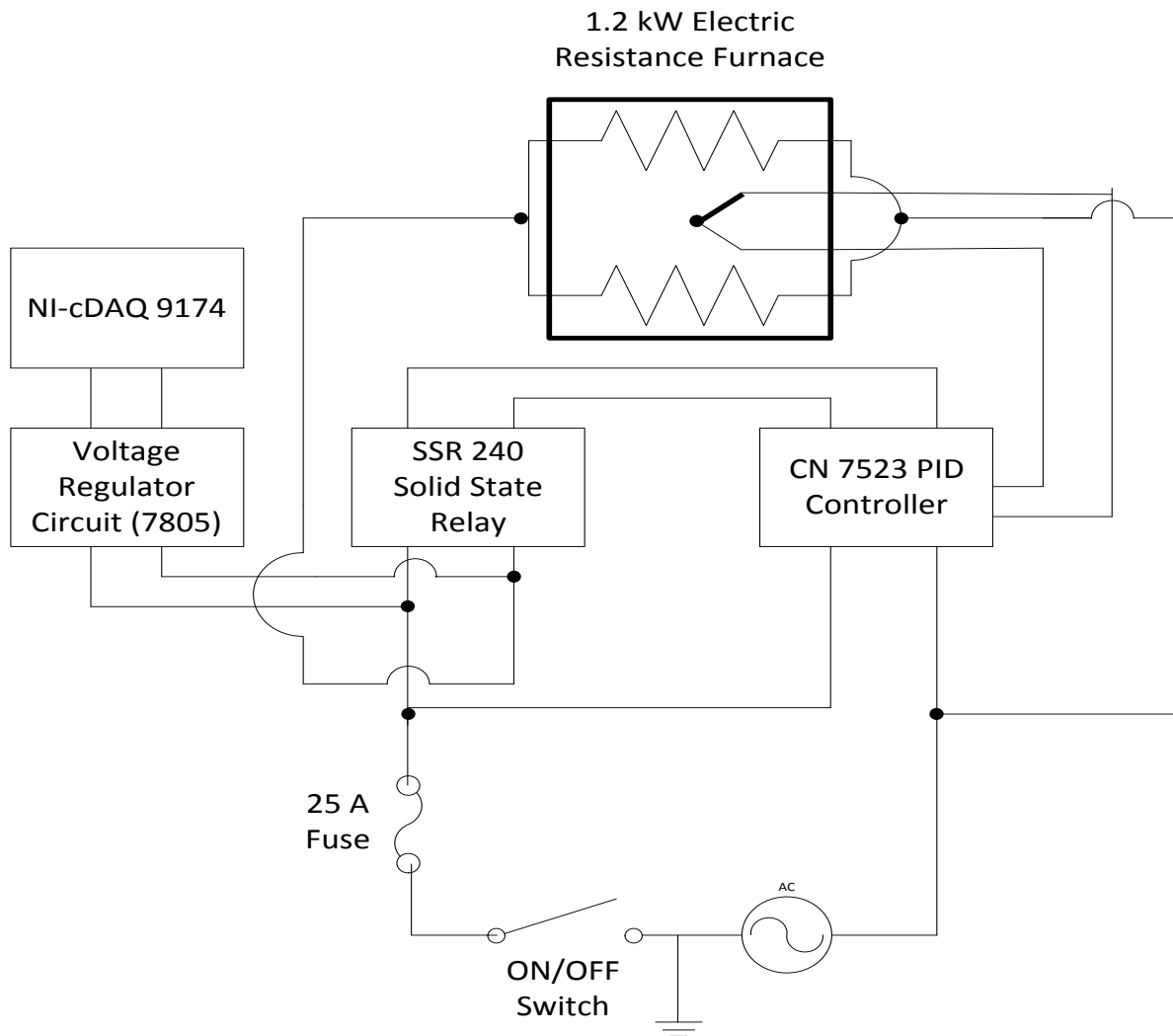


Figure 4.3: Electrical diagram of furnace control system.

Figure 4.3 illustrates the complete control system for the electrical resistance furnace used in this thesis work. Such a control system was required to maintain a set-point temperature, and to monitor the power consumption of the furnace.

The design choices for a membrane reactor system to decompose ammonia for hydrogen production have been mentioned and justified above in Section 4.1 and illustrated in Figures 4.1 through 4.3. Figures 4.4 through 4.7 depict the completed experimental unit.



Figure 4.4: Frontal view of experimental setup.



Figure 4.5: Left hand side view of experimental setup.

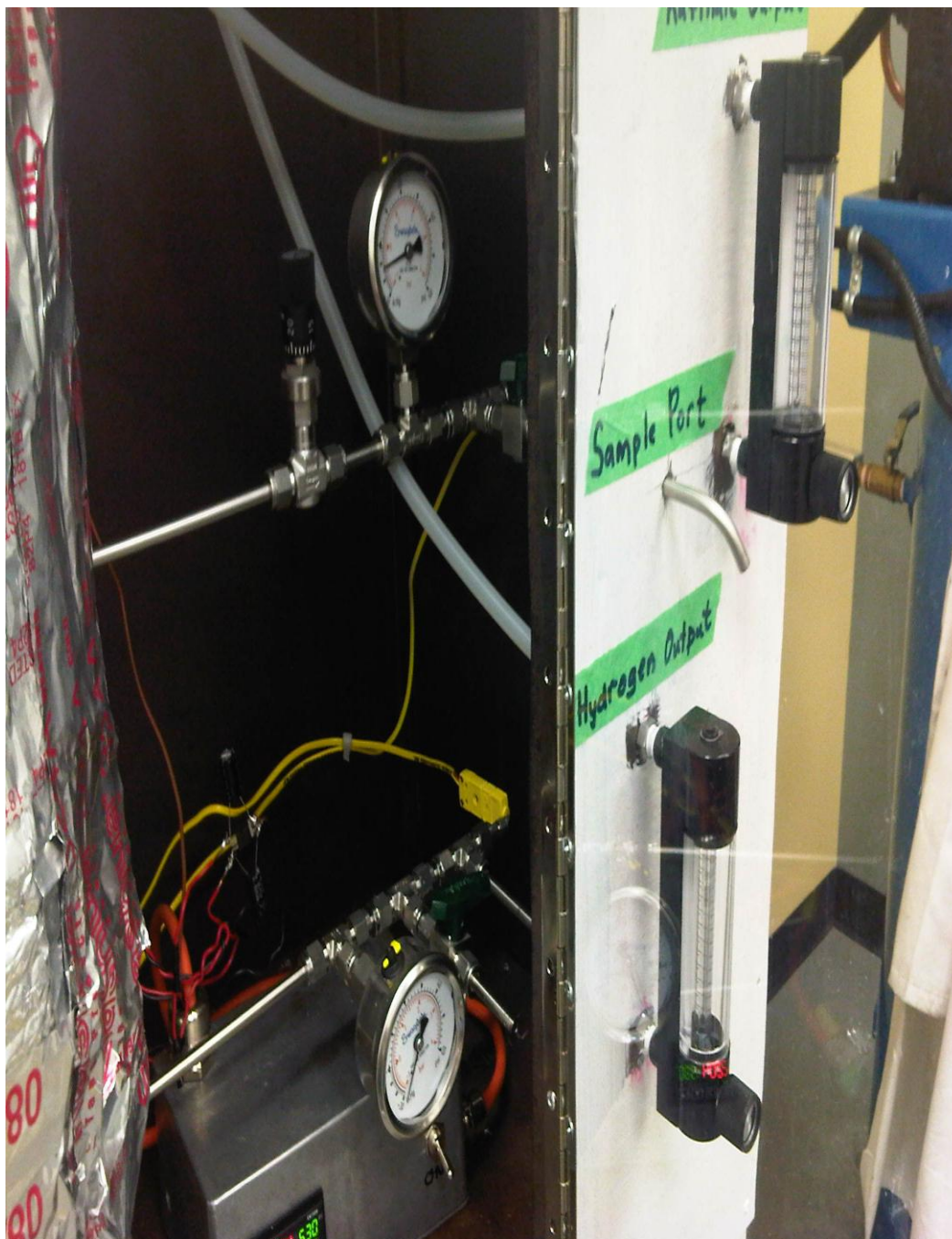


Figure 4.6: Right hand side view of experimental setup.

#### 4.1.1 Charging the Experimental Unit with $\text{NH}_3$

The ammonia preheater was built to ensure that the reactor was supplied with ammonia at a constant pressure and temperature. A Neslab RTE – 140 heater/chiller was used to circulate an 80:20 mixture of laboratory grade ethylene – glycol and water at a constant temperature. The

charging procedure is described below with some calculations based on the performance ratings from the RTE – 140 manual [37].

- 1) The NH<sub>3</sub> preheater tank was brought down to – 29.0 in.Hg. of vacuum. This was done to eliminate the presence of air in the system.
- 2) The valves were opened to allow high pressure NH<sub>3</sub> (8.6 bar) to flow into the NH<sub>3</sub> preheater tank.
- 3) When the pressures equalized at 8.6 bar, the RTE – 140 was set at 0°C and the pump was turned on.
- 4) This was allowed to run for 6.0 minutes to condense approximately 130.0 g of NH<sub>3</sub>.
- 5) Since the required amount of NH<sub>3</sub> was in the preheater tank, the RTE – 140 was turned to heating mode (54°C) to pressurize the NH<sub>3</sub> to approximately 21.0 bar (308.0 psi).

These quantities were determined by a simple energy balance between the cooling capacity of the RTE – 140 and the enthalpy of vapourization for NH<sub>3</sub> at 0°C.

$$\dot{Q}_{cool.} = \dot{m}_{cond.} * \Delta H_{evap.} \quad (4.3)$$

The enthalpy of vapourization of NH<sub>3</sub> at 0°C is 1262.0 kJ/kg [38] and the cooling capacity of the RTE – 140 is 0.500 kW at 0°C [37]. When these were substituted into Eq. 4.3, the condensation rate of NH<sub>3</sub> is 0.3962 g/sec. Since the reactor required a maximum of 3.0 mg/sec of NH<sub>3</sub>, then based on a 12.0 hour working day this was approximately 130.0 g of NH<sub>3</sub>.

$$\frac{m_{NH_3,tot.}}{\dot{m}_{NH_3,cond.}} = t_{fill.} \quad (4.4)$$

Here, the time required to fill the NH<sub>3</sub> preheater with enough NH<sub>3</sub> to operate for 12.0 hours at a feed rate of 3.0 mg/sec was 5.47 minutes. A filling time of approximately 6.0 minutes is suggested to ensure sure the system doesn't prematurely run out of NH<sub>3</sub>.

Since the reactor has a safe maximum operating pressure of 25.0 bar, the NH<sub>3</sub> preheater tank needs to be maintained at approximately 52.0°C. To do this, the RTE – 140 was switched to heating mode with a maximum heating capacity of 0.800 kW [37]. When Eqs. 4.3 and 4.4 are used again at a temperature of 50.0°C, the NH<sub>3</sub> phase change rate is approximately 0.7612 g/sec. This is far greater than the required 3.0 mg/sec required for operation. That being said, all this

value tells the reader is that the NH<sub>3</sub> vapour pressure should not drop unexpectedly due to lack of NH<sub>3</sub> vapour production. This was required to maintain a constant NH<sub>3</sub> feed pressure to the reactor.

#### 4.2 Statistical Design of the NH<sub>3</sub> Decomposition Experiments

In order to increase the efficiency of the experimental process, it was decided that the statistical design of experiments should be employed. Three main control parameters influence hydrogen production and reactor performance: temperature, pressure, and ammonia flow rate. When a general factorial design is used for these three variables with temperature, pressure and ammonia flow all having a depth of three, the result is 18 experimental runs [39].

Furthermore, a quantity called residence time will be introduced here. Residence time is commonly used in chemical engineering applications. It is defined as the time required for a volume of gas in the reactor vessel to travel the length of the reactor and exit. For an empty bare tube, residence time is simply the ratio of reactor volume to volumetric flow rate. Since this thesis is using a packed bed membrane reactor (PBMR), the residence time calculation must contain the statistical void fraction. Statistical void fraction is strictly a function of catalyst bed volume and total reactor volume. From [22], the statistical void fraction is defined as:

$$\epsilon = 1 - \frac{V_s}{V_t} \quad (4.5)$$

When Eq. 4.5 is substituted equation into the continuity equation and it is solved for residence time, the following equation is obtained:

$$t_{res} = \frac{V_r}{\dot{v} * \epsilon} \quad (4.6)$$

Given that the dimensions of the reactor and height of the packed bed are known values. The reactor height is 18.0", the inner diameter is 0.50" and the packing height was approximately 17.75". The residence times corresponding to the various ammonia flow rates were determined by Eq. 4.6 and listed in Table 4.1.

Table 4.1: Experimental conditions investigated.

Run #	Temperature (°C)	Pressure (bar)	NH <sub>3</sub> Flow Rate (mL/min)	Residence Time (s)	Max. H <sub>2</sub> Output (std.mL/min)
1,2	400.0, 500.0	5.0	12.0	3.748	75.0
3,4	400.0, 500.0	10.0	5.06	7.058	75.0
5,6	400.0, 500.0	20.0	2.25	15.86	75.0
7,8	400.0, 500.0	5.0	24.0	1.784	150.0
9,10	400.0, 500.0	10.0	10.12	3.529	150.0
11,12	400.0, 500.0	20.0	4.50	7.929	150.0
13,14	400.0, 500.0	5.0	48.0	0.937	300.0
15,16	400.0, 500.0	10.0	20.24	1.764	300.0
17,18	400.0, 500.0	20.0	9.0	3.965	300.0

Table 4.2: Experimental run table.

Run #	Time (min)	H <sub>2</sub> Flow (mL/min)	H <sub>2</sub> Pressure (bar)	Rafinate Flow (mL/min)	Rafinate Pressure (bar)
Pressure (bar)	5.0				
Temperature (°C)	10.0				
NH <sub>3</sub> Flow Rate (mL/min)	...				
Residence Time (s)	115.0				
	120.0				

### **4.3 Experimental Method for Conducting the NH<sub>3</sub> Decomposition Experiments**

As a step – by – step procedure, the ammonia decomposition experiments were conducted as follows:

- 1) The system was fully charged with NH<sub>3</sub> and the needle valve and both 65.0 mm rotameter valves were fully closed.
- 2) The furnace was brought up to the desired temperature and was allowed to stand for approximately 30 minutes to allow for steady state behaviour.
- 3) NH<sub>3</sub> was introduced at the desired pressure.
- 4) The needle valve was slowly opened to obtain the desired flow rate.
- 5) The system was allowed to run for 120.0 minutes.
- 6) This was repeated for the remaining two flow rates.
- 7) The needle valve was fully closed and the 65.0 mm rotameter on the raffinate stream was open until there was ~ 1.0 bar of pressure.
- 8) The 65.0 mm rotameter on the H<sub>2</sub> stream was fully shut.
- 9) The operating pressure was regulated to 5.0 bar with the forward pressure regulator.
- 10) Steps 4 through 6 were repeated for the remaining two flow rates.
- 11) The temperature was increased to the required temperature of the next experiment and steps 1 through 9 were repeated.
- 12) Each experiment was repeated three times to demonstrate repeatability and reliability of the experimental unit.

### **4.4 Method for Determining the Transient NH<sub>3</sub> Concentration in the Raffinate Stream**

Any efficient chemical reactor should convert the maximum amount of reactant into product. In other words, the amount of unreacted reactants should be minimized. In [29] a minimum ammonia concentration of 10,000 ppm was detected in the raffinate stream and a maximum ammonia conversion of 98.0 % was obtained. As a safeguard, all flow streams were disposed of via a fumehood after measurements. In this thesis work, the ammonia concentration as a function of time will be determined by calculating the difference between the amount of ammonia fed into the reactor and the amount of ammonia decomposed to produce hydrogen. The experimental data for the mass and energy flows were balanced to determine the transient ammonia concentration in the raffinate stream and the transient ammonia conversion percentage. Since the

ammonia feed rate was controlled and the raffinate and hydrogen production over time was measured, therefore simple mass and energy balances between the amount of hydrogen produced and the ammonia feed according to the balanced chemical equation with hydrogen production as the limiting factor would yield transient ammonia concentration in the raffinate stream.

# Chapter 5: Results and Discussion

## 5.1 Results for Hydrogen Production

The results for hydrogen production are shown below in Figures 5.1 through 5.6. The membrane itself is rated for a maximum hydrogen flux of 300.0 sccm [40] which equates to approximately 50.0 W of thermal power if it was to be perfectly combusted. The figures shown below are the results for hydrogen production as a function of time for the experimental conditions studied.

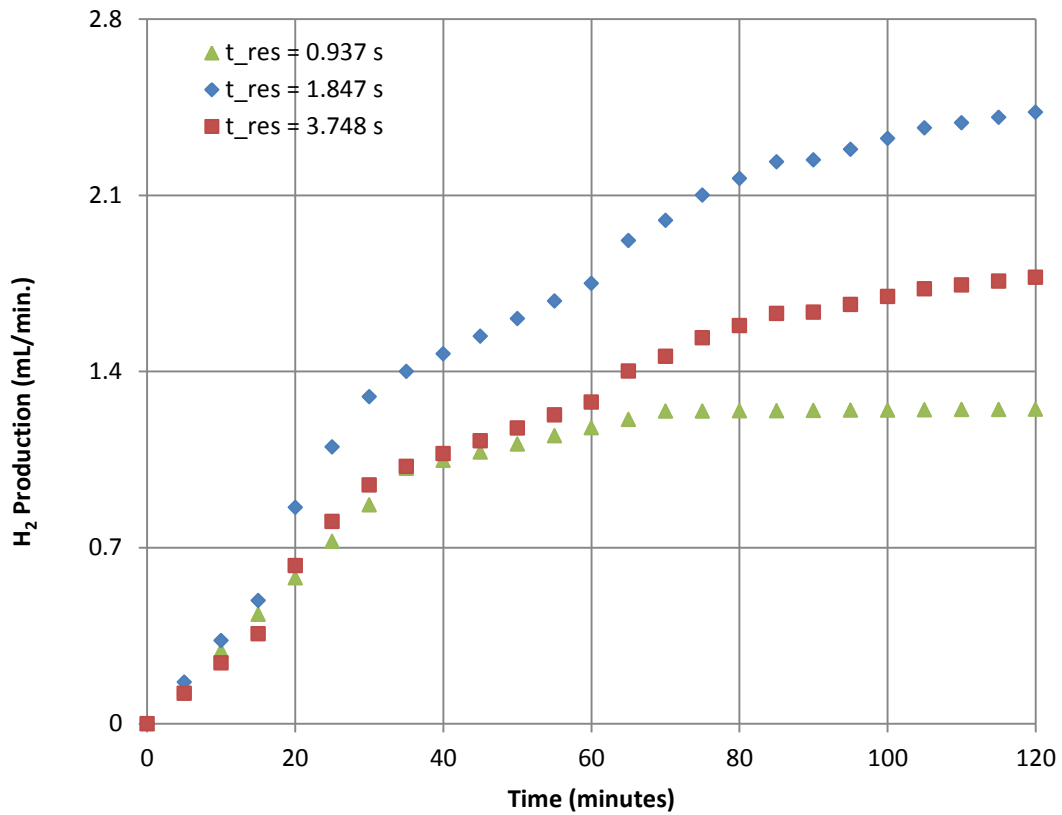


Figure 5.1: H<sub>2</sub> production vs. time at 400°C, 5.0 bar and three residence times.

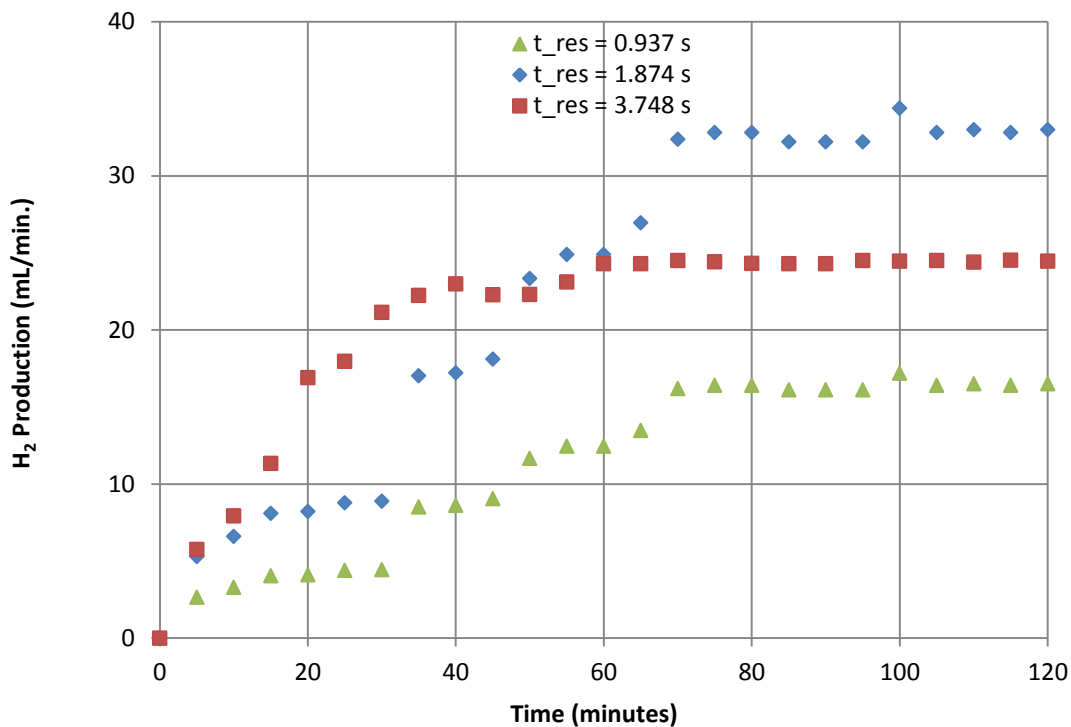


Figure 5.2: H<sub>2</sub> production vs. time at 500°C, 5.0 bar and three residence times.

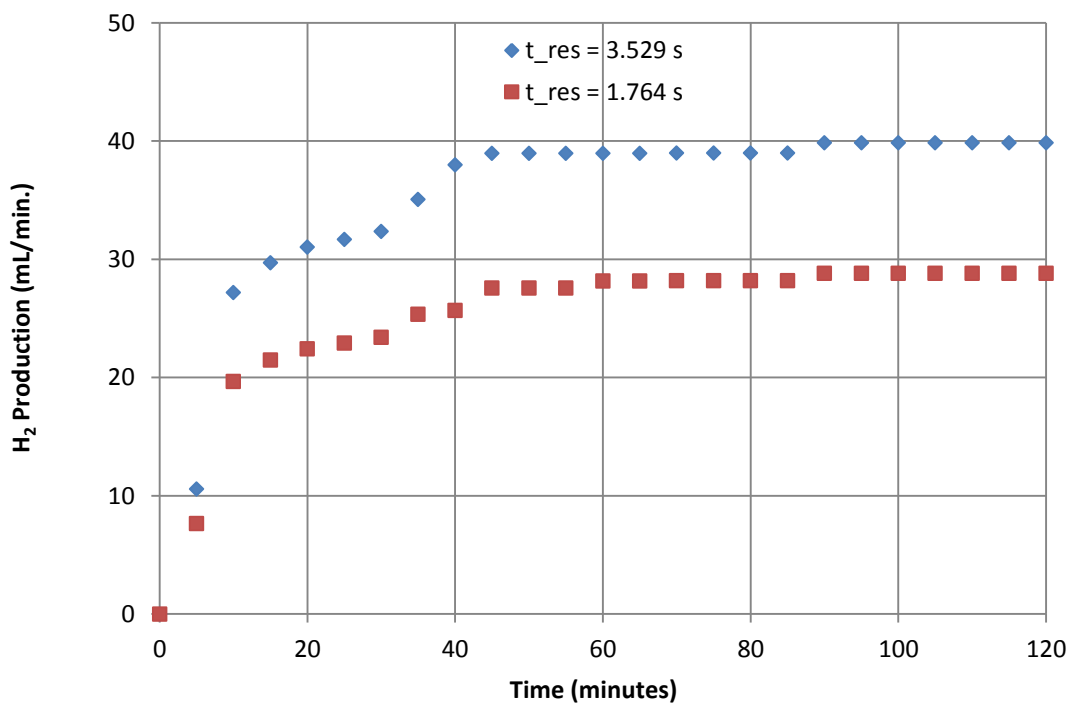


Figure 5.3: H<sub>2</sub> production vs. time at 400°C, 10.0 bar and two residence times.

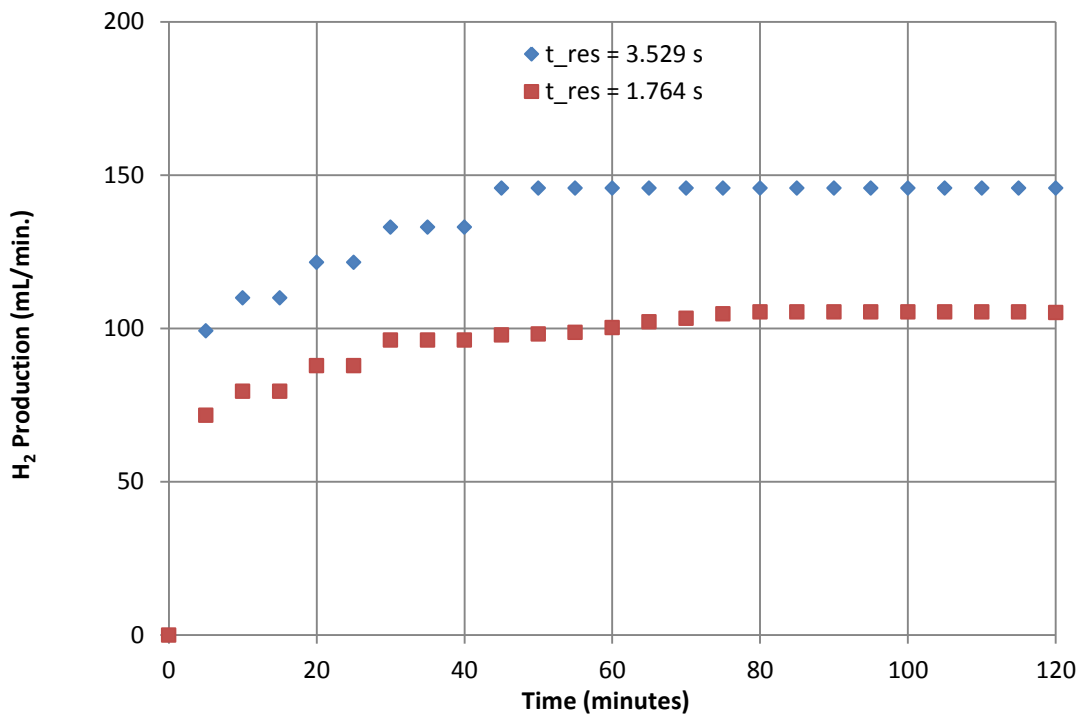


Figure 5.4: H<sub>2</sub> production vs. time at 500°C, 10.0 bar and two residence times.

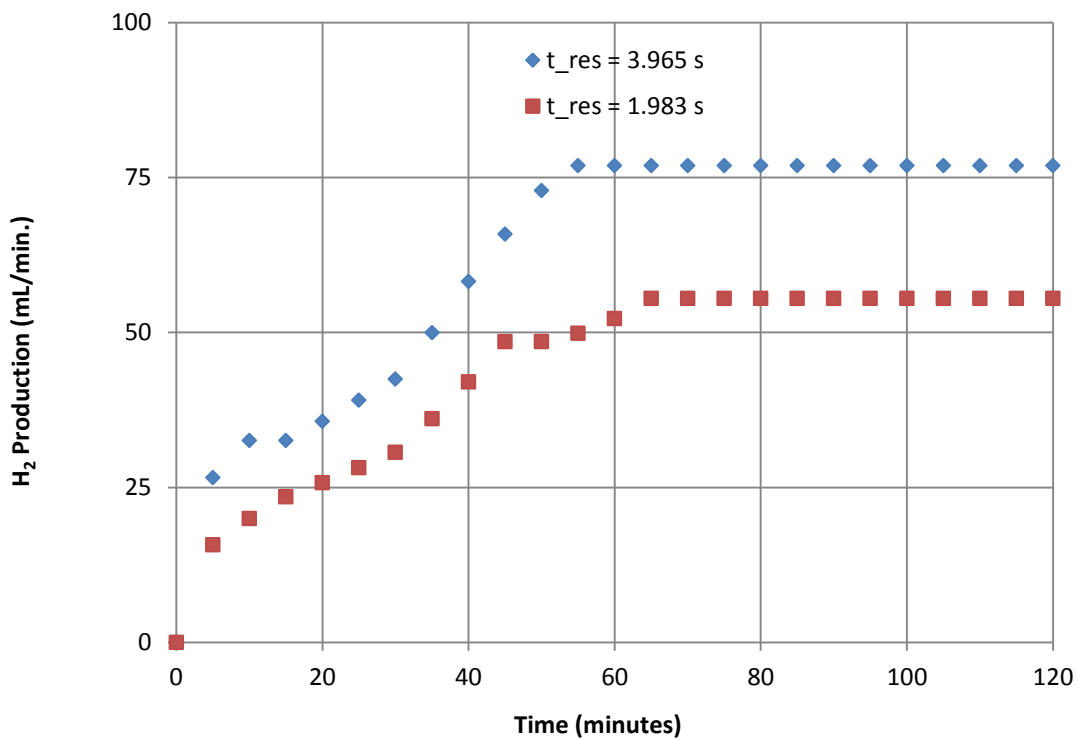


Figure 5.5: H<sub>2</sub> production vs. time at 400°C, 20.0 bar and two residence times.

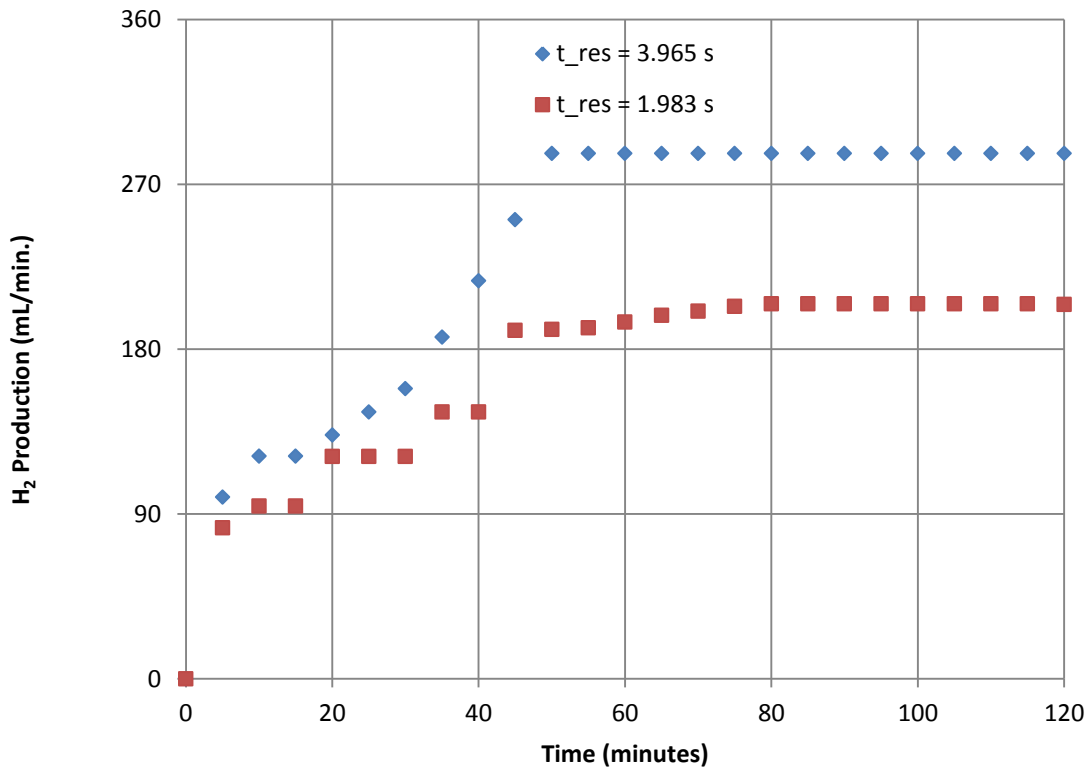


Figure 5.6: H<sub>2</sub> production vs. time at 500°C, 20.0 bar and two residence times.

Figures 5.1 through 5.6 illustrate a positive temperature and pressure dependence of ammonia decomposition over a Ni<sub>2</sub>O<sub>3</sub> catalyst. Hydrogen production was found to be at a maximum at the highest pressure and temperature investigated in this thesis work (20.0 bar, 500.0°C). The effects of increasing the operating pressure was determined to be three fold. Firstly, a higher pressure increases the ammonia density and ergo reduces the volumetric flow rate. Due to this, a higher residence time was achieved and more hydrogen was produced for a given mass flow rate. Secondly, due to the higher hydrogen partial pressure in the reactor associated with the higher operating pressure, there was a greater trans-membrane pressure difference. This increase in trans-membrane pressure difference was responsible for effectively generating a larger driving force which increased the flux of the hydrogen through the membrane. This was found to be in full agreement with [25-28] and was again observed in this experimental work. Finally, the by removing hydrogen from the product stream at a greater rate via higher operating pressure as previously mentioned, the hydrogen production rate would, initially, be much faster and would eventually reach a steady state value. This was determined to be due to the nature of the membrane reactor and the favourable equilibrium shift associated with

product removal as mentioned in [11,12,15,16]. All of the above mentioned points were experimentally verified in this thesis work and were all presented above in Figures 5.1 through 5.6. At 500.0°C and with a residence time in the neighborhood of 3.6 seconds, it was found that a quadrupling of reactor pressure caused approximately an increase in hydrogen production by a factor of approximately 12.0. Moreover, it was concluded that the reason for such seemingly low hydrogen production at 400°C was due to the catalyst not being particularly active. The calculations in EES for Gibb's free energy (see Table 3.5) had shown that the thermodynamics of this reaction are more favourable at 500.0°C than at 400.0°C. This resulted in low hydrogen production values and steady state taking longer to reach. The most extreme case of that is the case of 5.0 bar and 400.0°C, where steady state was never reached in the 2.0 hour experimental time. However, when the temperature was later increased to 500°C, the results for hydrogen production correlated better with the hypothesized expectations. The shortest threshold time required to reach steady state was observed to be approximately 45.0 minutes at 10.0 bar, 400.0°C and 500.0°C and for a residence time of approximately 3.529s. Since measurements were read in 5 minute intervals while the author attempted to steady the ammonia flow rate with the needle valve. The error and difficulty of this point resulted in changes in the slopes of the graphs and step like behaviour. These results agree well with the published experimental results of [15, 41, 42] with respect to the positive effects of pressure, temperature and residence time on hydrogen production trends. Due to the inaccuracies inherent with manual control, the hydrogen production fluctuated because of spikes in ammonia flow due to forward pressure regulation and the sensitivity of the metering valve. Coupled with this, the standard error reported by the manufacturer of the glass tube flow meters are +/- 2% of full scale.

## **5.2 Results for Overall System Performance**

Like any thermodynamic system, the maximization of system performance is ideal. Energy and exergy ratios coupled with energy and exergy efficiencies are the major performance indicators of the system under investigation. In this section, the calculations based on the data are broken down as transient energy and exergy ratios followed by energy and exergy efficiencies for steady state operation. This was for three reasons. Firstly, the system under consideration is ideally operating with waste heat as the energy source and is not a thermodynamic cycle per se, therefore the focus should be on the operating conditions which facilitate the maximum ratio of output to input. Secondly, since the ultimate objective of this experimentation was to make

conclusions about using a membrane reactor such as this to potentially provide fuel for an engine or fuel cell on demand without having to store hydrogen onboard; the ideal measure of this should be energy and exergy ratios that are hopefully greater than unity. Finally, the systems energy and exergy efficiencies are the prime performance indicators and paint the most descriptive picture of the system's thermodynamics.

The system under consideration requires an integrated approach for the calculation of system efficiency. Relevant measured quantities in this experiment were the hydrogen production rate in mL/min, the ammonia feed rate in mL/min. These were both later converted to kg/sec by multiplying by the appropriate conversion factors. The enthalpy of reaction was calculated as a function of temperature in EES and was converted to kJ/kg. Finally, the lower heating value of hydrogen was taken as approximately 121,000 kJ/kg. Figures 5.7 through 5.12 show the results for energy as a function of time.

The energy ratio for the reaction was calculated as a ratio of hydrogen energy output to ammonia energy requirement by the following equation:

$$\varepsilon_{sys}(t) = \frac{LHV_{H_2} * \int_0^t \dot{m}_{H_2}(t) * dt}{\Delta H_{rxn, NH_3} * \int_0^t \dot{m}_{NH_3}(t) * dt} \quad (5.1)$$

The exergy ratio for the reaction was calculated in a similar fashion. The chemical exergies of the required elements hydrogen were taken from [43]. A small computer code was written in EES to determine the relevant chemical exergies required to determine the exergy ratio. The exergy ratio was calculated with Eq. 5.2 and presented in Figures 5.13 through 5.18.

$$\varphi_{sys}(t) = \frac{Ex_{H_2} * \int_0^t \dot{m}_{H_2}(t) * dt}{Ex_{NH_3} * \int_0^t \dot{m}_{NH_3}(t) * dt} \quad (5.2)$$

The chemical exergy of hydrogen was taken directly from [43]. The thermomechanical component of the total exergy was determined to be negligible by the computation. Therefore, only the chemical exergy was used. The standard exergy of ammonia had to be computed by the following equation:

$$Ex_{tot}^{NH_3} = G_f^0 + \sum_i n_i * Ex_i^0 + [h(P_r, x_g) - h_o] - T_o * [S(T_{H_2}, P_{H_2}) - S_o] \quad (5.3)$$

$$G_f^0 = H_f^0 - T_o * S_f^0 \quad (5.4)$$

The maximum energy and exergy efficiencies of the reactor system at steady state were calculated by Eqs. 5.5 and 5.6, respectively. They were graphed in Figures 5.19 and 5.20 for the pressure and temperatures of 10.0 bar to 20.0 bar and 400.0°C to 500.0°C, respectively. The

results for energy and exergy efficiency for the experiments at 5.0 bar were omitted from this calculation due to the system never reaching steady state.

$$\eta_{steady,max} = \frac{LHV_{H_2} * \dot{m}_{H_2,steady}}{LHV_{NH_3} * \dot{m}_{NH_3,steady} + \dot{Q}_{in}} \quad (5.5)$$

$$\epsilon_{steady,max} = \frac{Ex_{tot}^{H_2} * \dot{m}_{H_2,steady}}{Ex_{tot}^{NH_3} * \dot{m}_{NH_3,steady} + Ex_{heat}} \quad (5.6)$$

The exergy due to heat was determined as the product of the furnaces power rating, fraction of “on-time”, and the Carnot number. It is expressed as follows:

$$Ex_{heat} = P_{tot} * \dot{Q}_{in} * \left(1 - \frac{T_0}{T_r}\right) \quad (5.7)$$

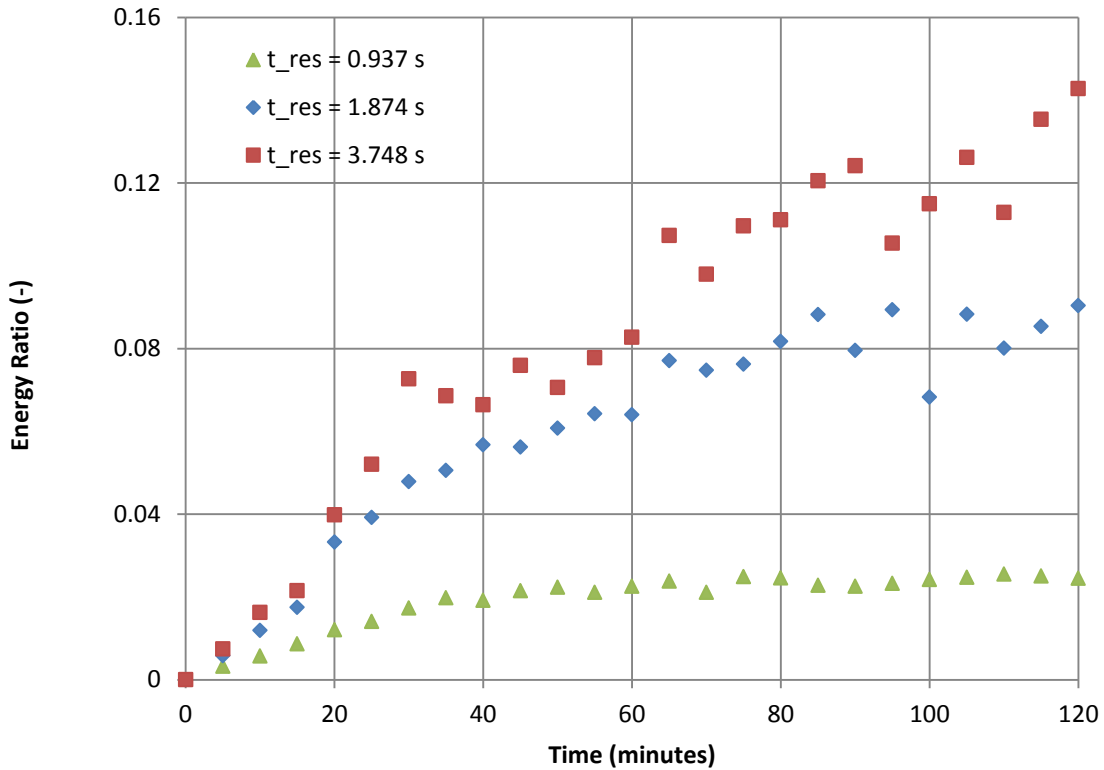


Figure 5.7: Energy ratio (-) vs. time for 400°C, 5.0 bar and three residence times.

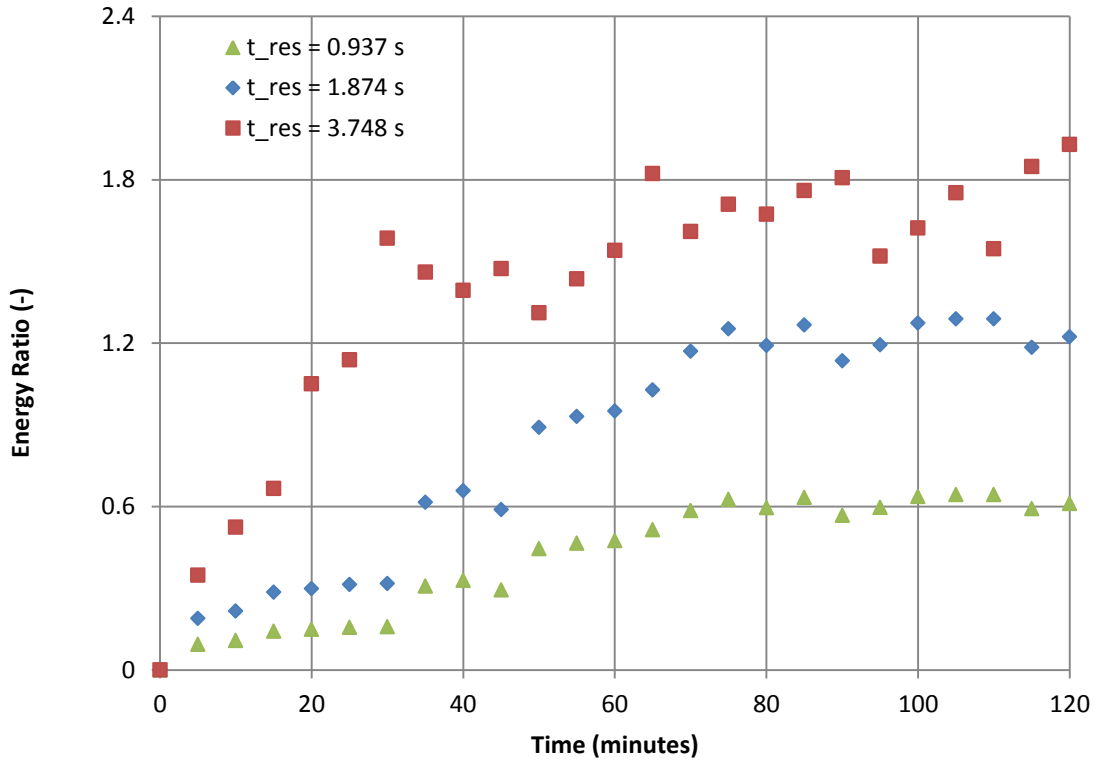


Figure 5.8: Energy ratio vs. time for 500°C, 5.0 bar and three residence times.

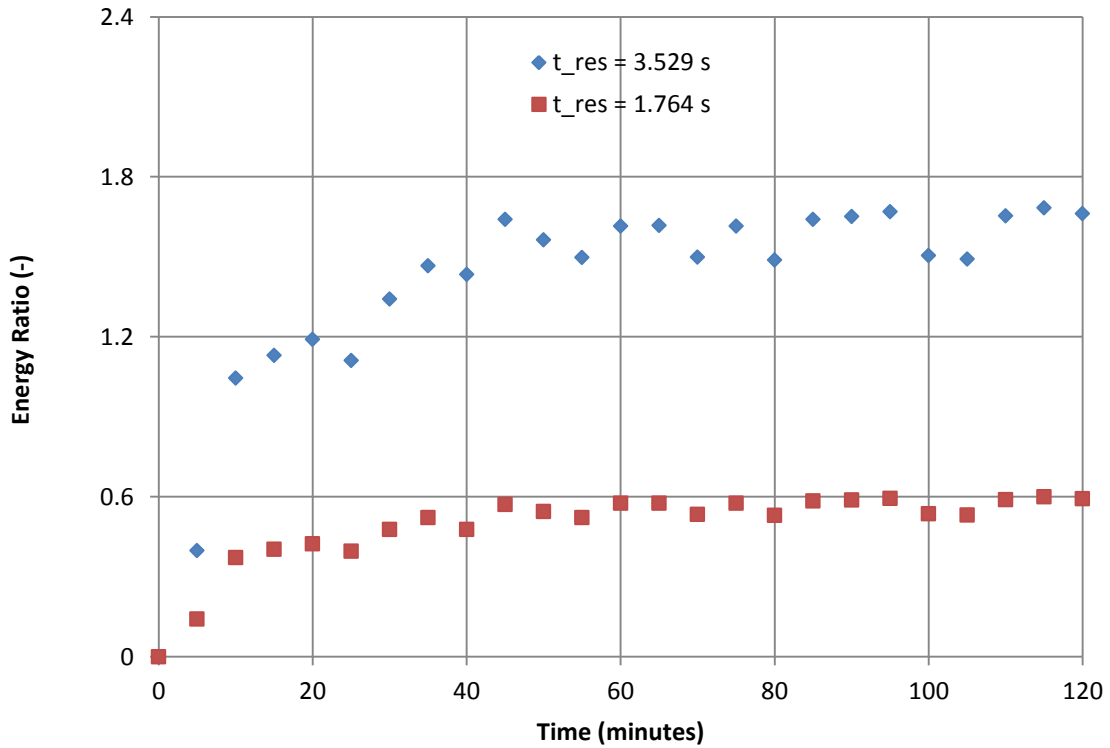


Figure 5.9: Energy ratio vs. time for 400°C, 10.0 bar and two residence times.

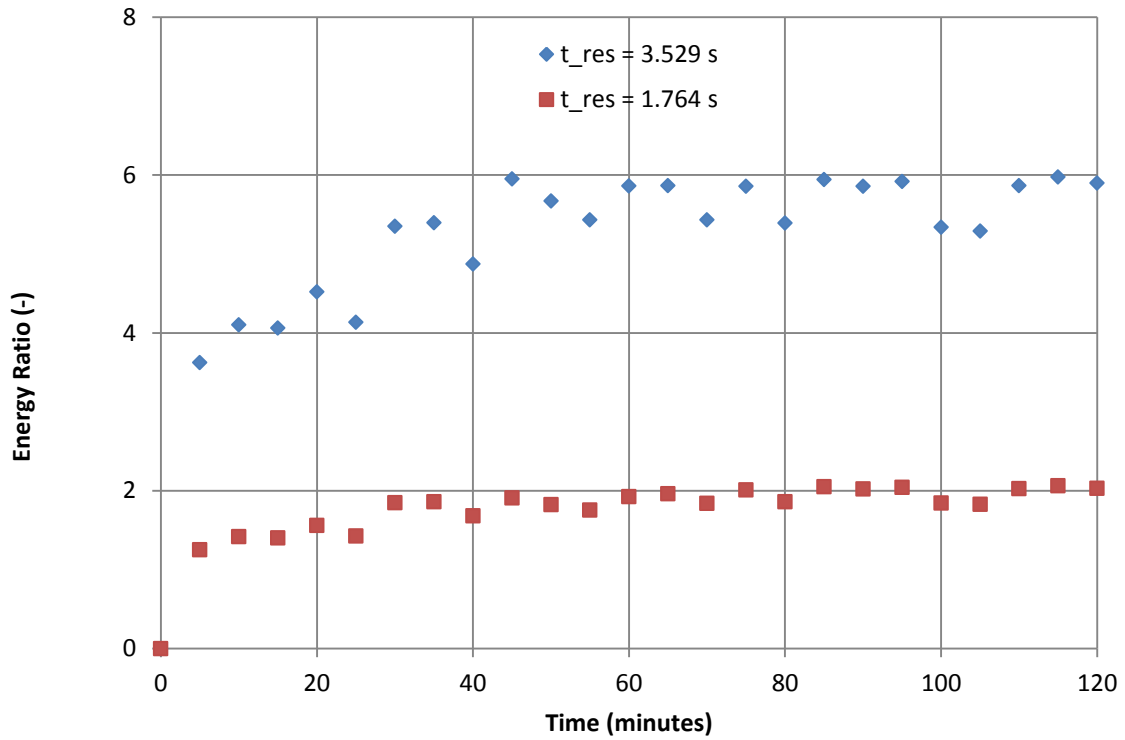


Figure 5.10: Energy ratio vs. time for 500°C, 10.0 bar and two residence times.

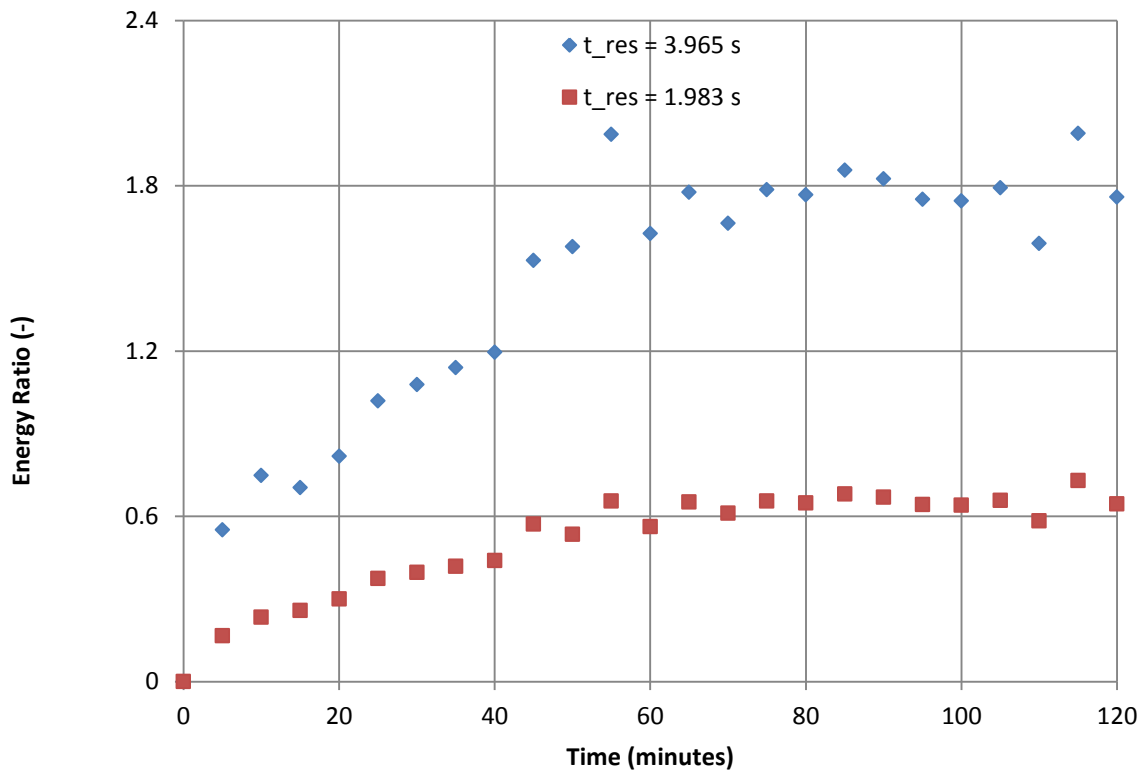


Figure 5.11: Energy ratio vs. time for 400°C, 20.0 bar and two residence times.

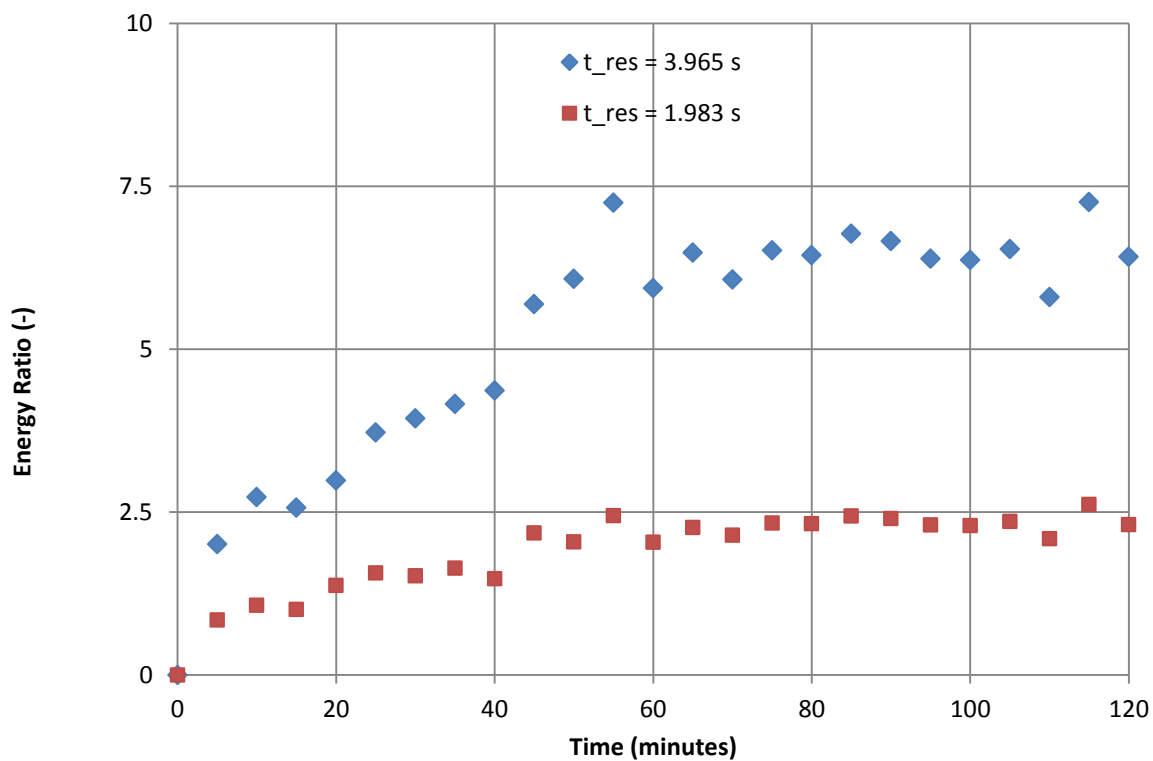


Figure 5.12: Energy ratio vs. time for 500°C, 20.0 bar and two residence times.

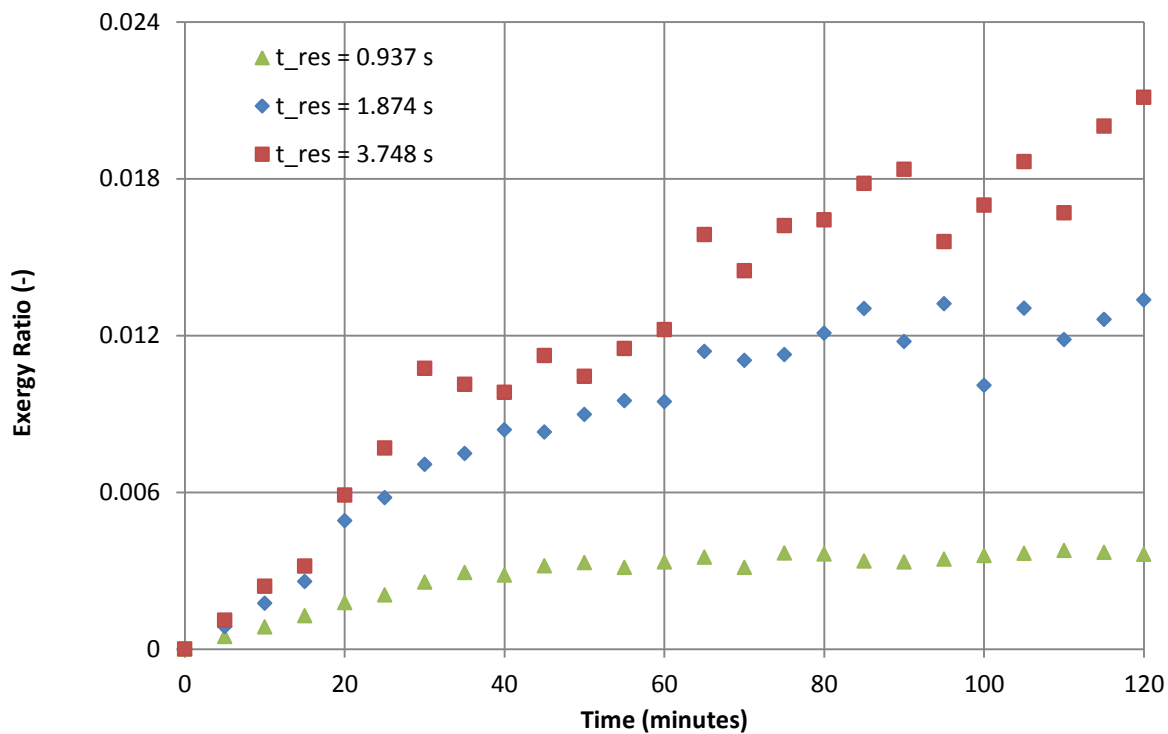


Figure 5.13: Energy ratio vs. time for 400°C, 5.0 bar and three residence times.

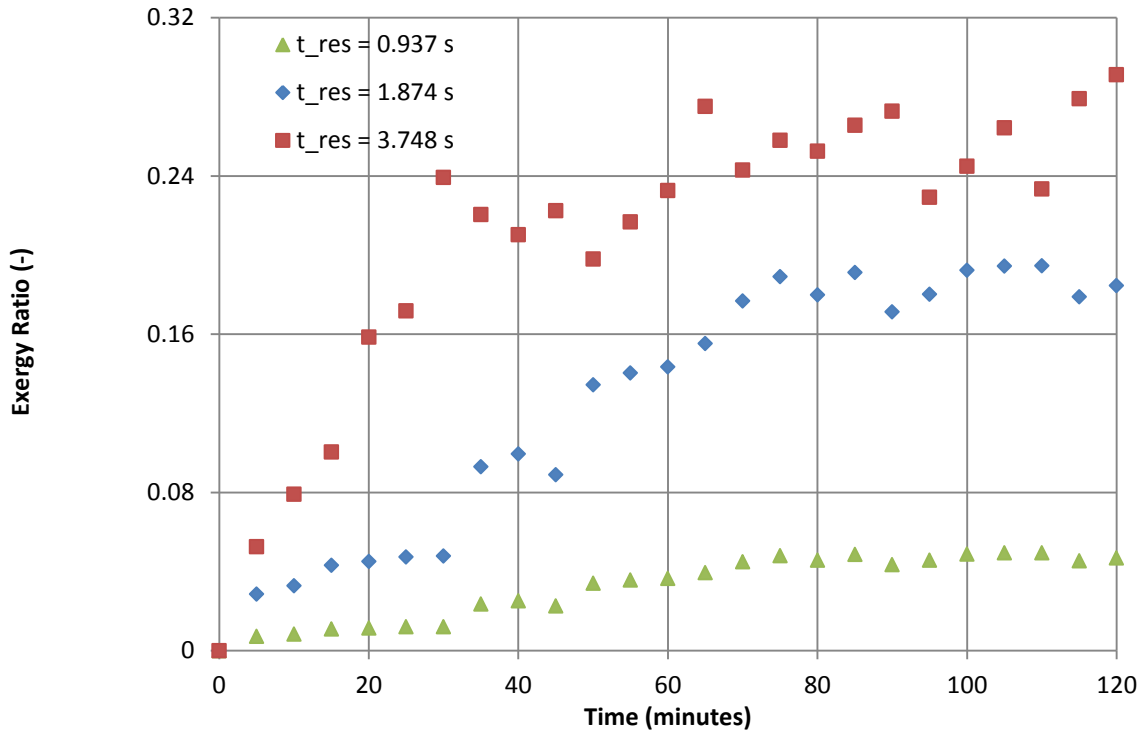


Figure 5.14: Exergy ratio vs. time for 500°C, 5.0 bar and three residence times.

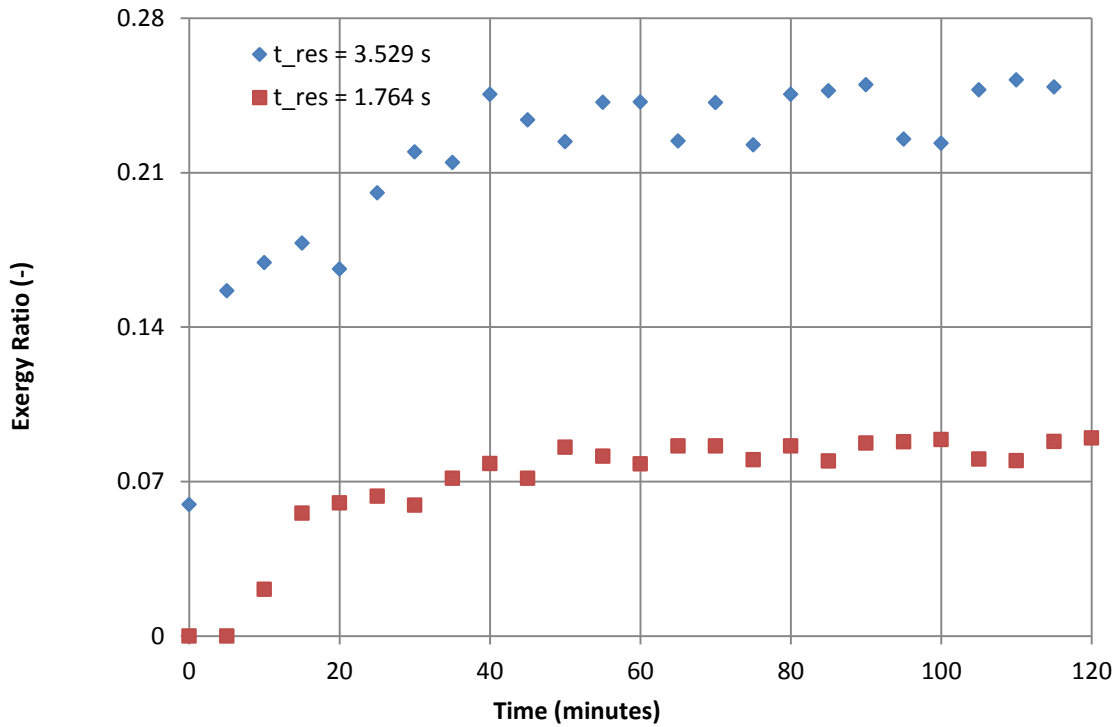


Figure 5.15: Exergy ratio vs. time for 400°C, 10.0 bar and two residence times.

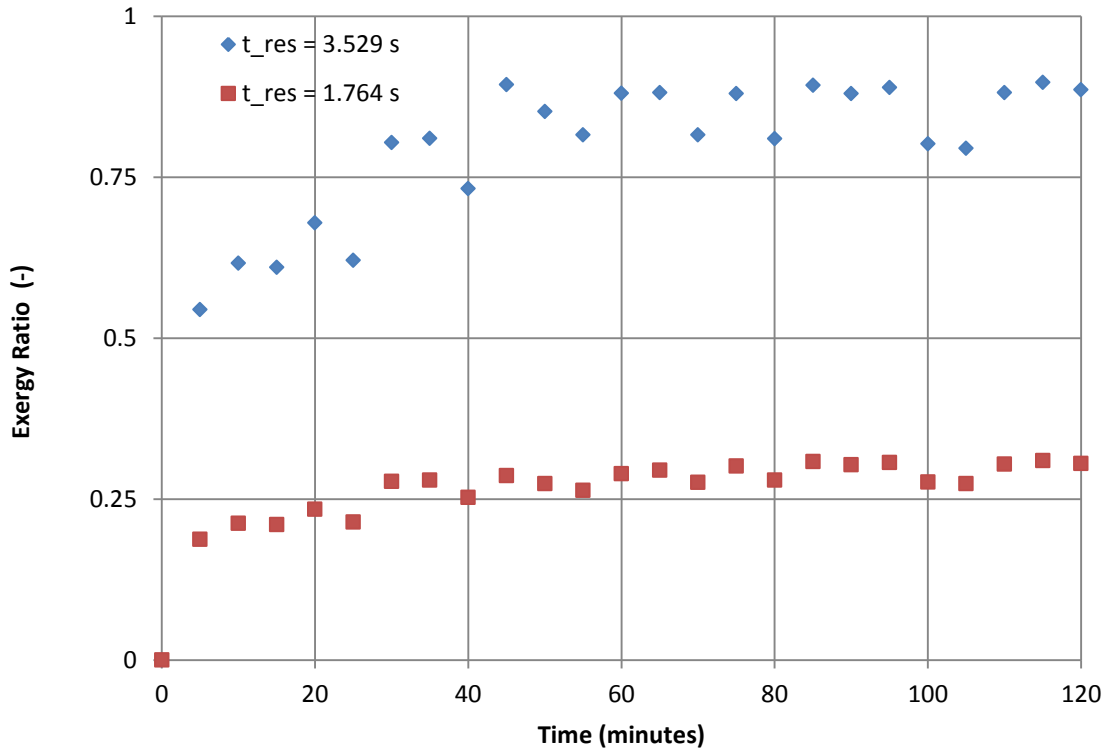


Figure 5.16: Exergy ratio vs. time for 500°C, 10.0 bar and two residence times.

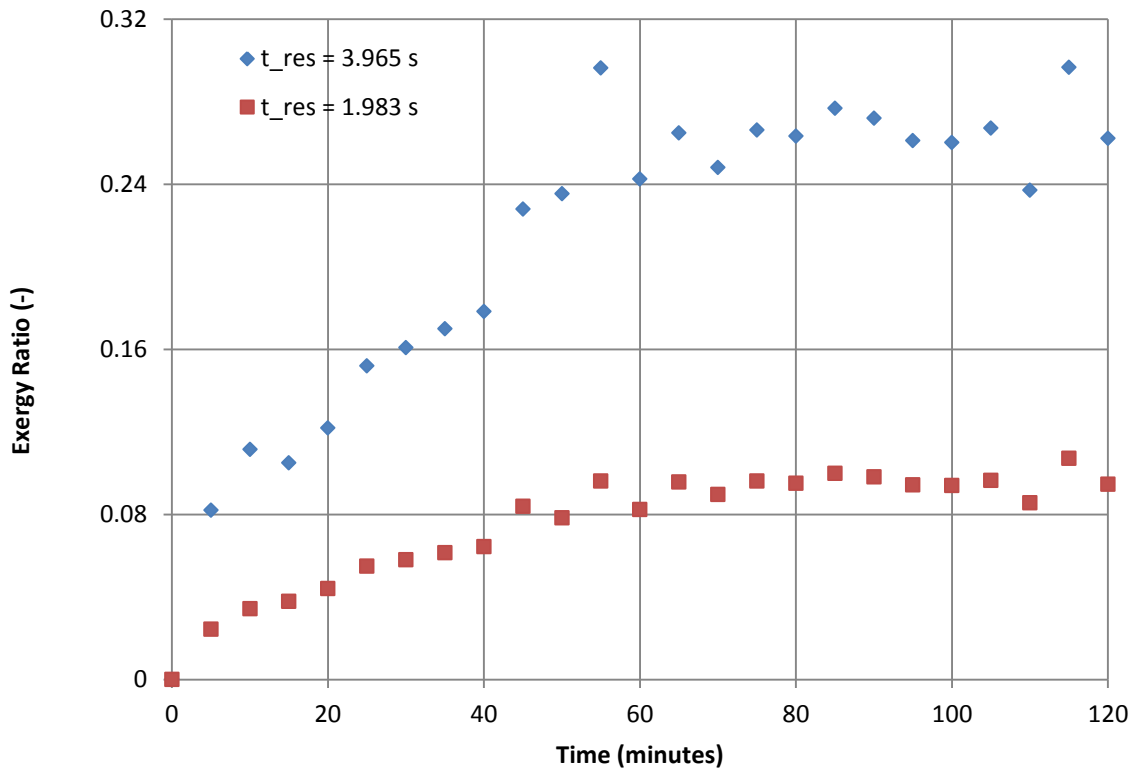


Figure 5.17: Exergy ratio vs. time for 400°C, 20.0 bar and two residence times.

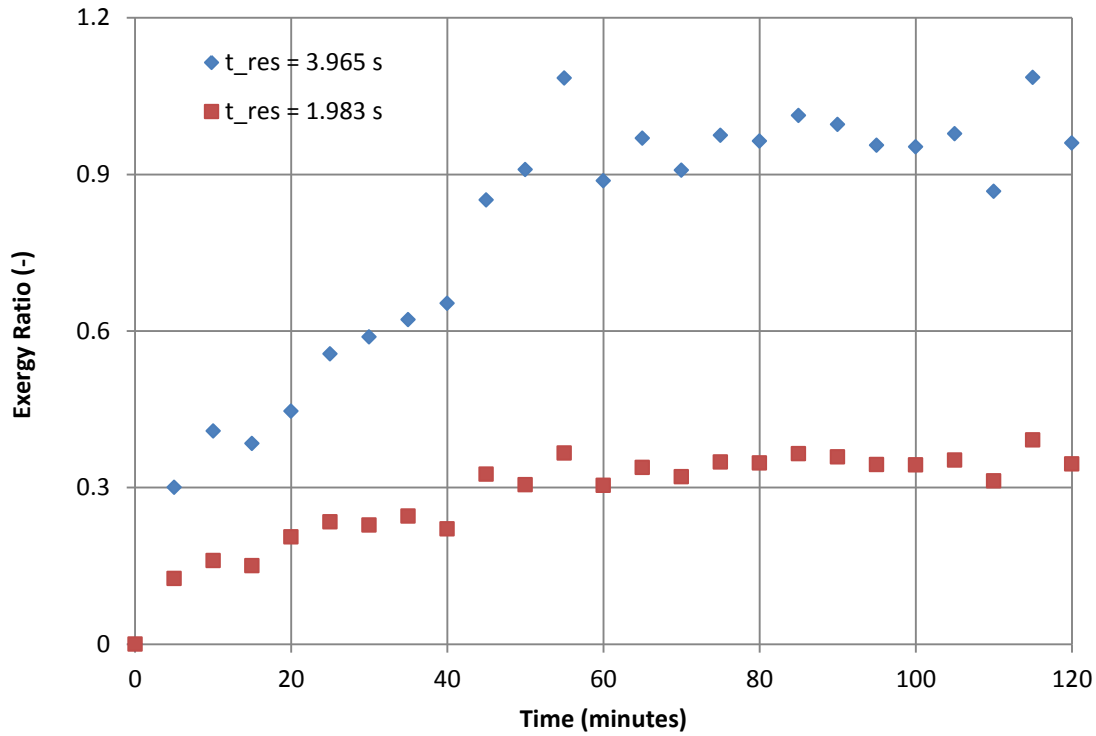


Figure 5.18: Exergy ratio vs. time for 500°C, 20.0 bar and two residence times.

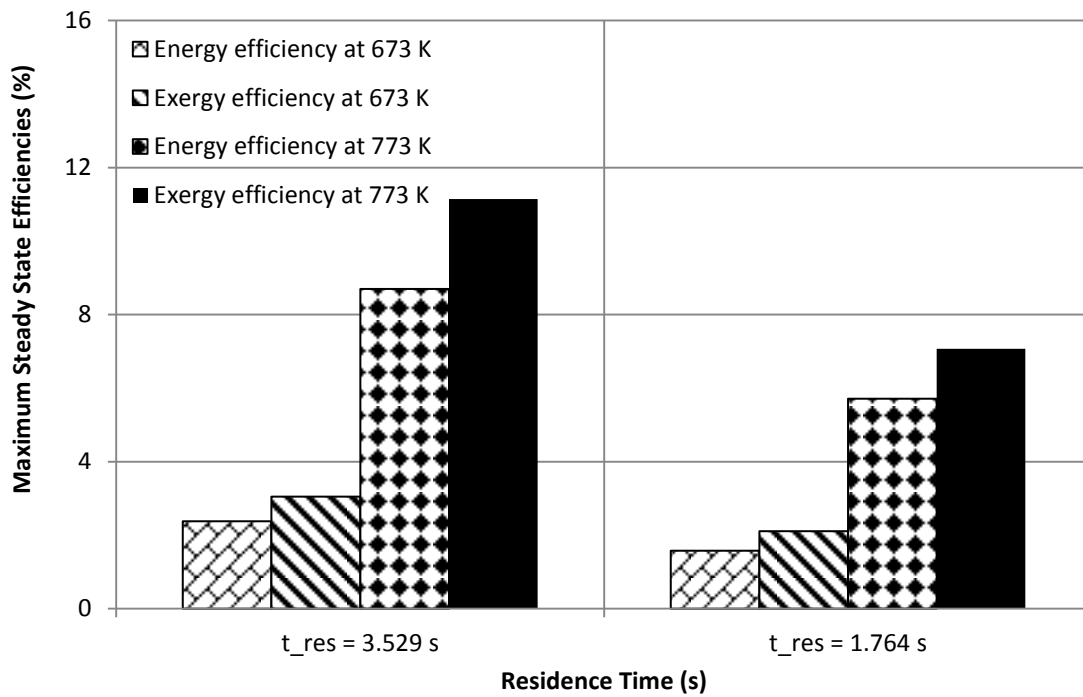


Figure 5.19: Maximum steady state energy and exergy efficiencies for 10.0 bar, 400.0°C, 500.0°C and two different residence times.

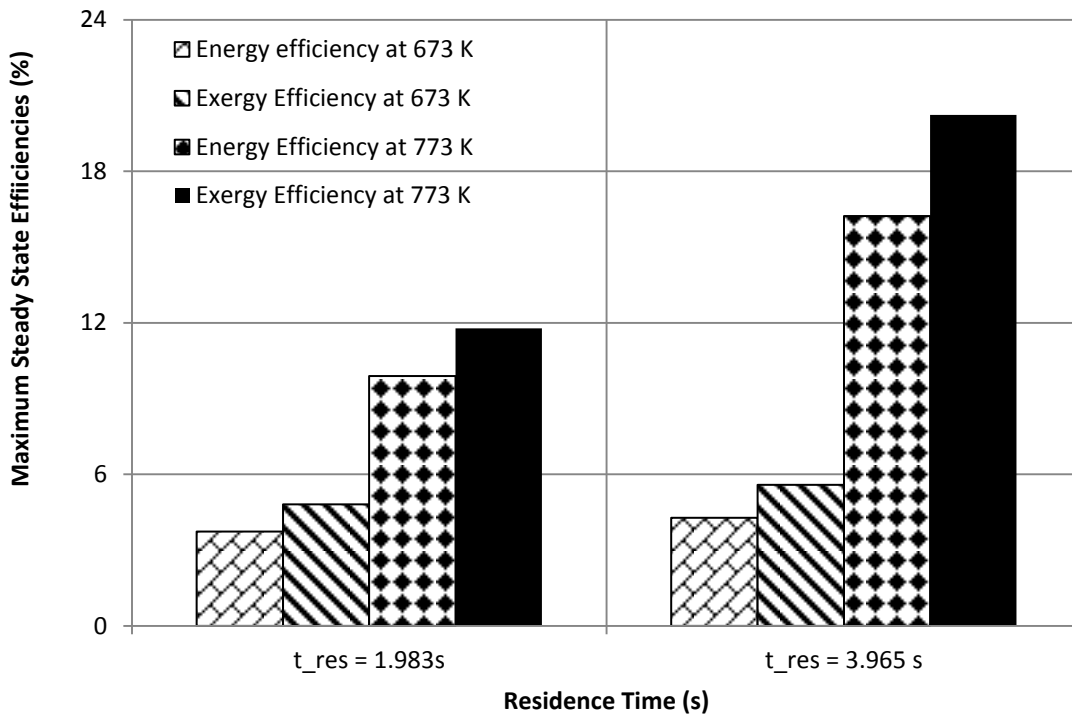


Figure 5.20: Maximum steady state energy and exergy efficiencies for 20.0 bar, 400.0°C, 500.0°C and two different residence times.

Figures 5.7 through 5.12 illustrate the positive effects of both pressure and temperature on energy ratio. The maximum allowable thermodynamic energy ratios by Eq. 5.1 are 7.0 and 6.87 for 400°C and 500°C, respectively. These two values would be akin to total ammonia conversion and maximum hydrogen production. The reasoning to employ an equation such as Eq. 5.1 was previously mentioned. That being said, the increase in energy ratio was found to be directly proportional to the increase in both operating temperature and pressure. High temperature and pressure resulted in the highest energy ratios in the range of 2.0 to 6.77 for the reaction. This was illustrated in Figures 5.10 and 5.12. This information suggested that in order to employ a membrane reactor system such as this for the purpose of providing fuel for an engine (see Figure 5.46), high pressure and temperature would be required to ensure the maximum fuel supply for the engine to ensure start up and continuous operation. Furthermore, high temperature and pressure would ensure maximum ammonia conversion and potentially eliminate the requirement for a nitrogen selective membrane to help recycle un-reacted ammonia (see Figure 5.46). Large fluctuations in the energy ratio were due to the fluctuations in ammonia and

hydrogen flow rates being amplified by a factor equal to the ratio of lower heating value of hydrogen to reaction enthalpy.

Figures 5.13 through 5.18 again illustrated the positive influence of increasing reactor temperature, feed pressure, and residence time on the exergy ratio. The exergy ratios for the reaction tended to be far less than unity for the pressure of 5.0 bar and the temperature of 400.0°C. According to Eq. 5.2, the exergy ratio is expected to decrease due to an increase in ammonia exergy at higher pressures. However, the increase of hydrogen production associated with the higher temperatures, pressures and residence times far outweighs the 3.5% increase in ammonia exergy when the pressure was increased from 5.0 bar to 20.0 bar. A maximum allowable exergy ratio for a perfect reaction was calculated to be 1.103:1. A maximum exergy ratio of 1.085:1 for the reaction was obtained at 20.0 bar and 500.0°C at a residence time of approximately 3.965s. This illustrated that 92.6% of the hydrogen's exergy output must be used to sustain the systems production via a feedback loop and only 7.4% of the hydrogen's exergy output would be a net gain. Also, the maximum exergy ratio for the reaction coincided with the conditions for maximum hydrogen production (see Figure 5.6). Furthermore, if a system such as this was to be integrated with an internal combustion engine to supply hydrogen fuel on demand, high pressures ( $P > 20.0$  bar) and temperatures ( $T > 500.0^\circ\text{C}$ ) should be used to for the high exergy ratios that would allow for a hydrogen feedback loop to provide heat for the reactor itself.

Figure 5.19 and 5.20 show the energy and exergy efficiencies of the system for two example scenarios. Both energy and exergy efficiencies were positively influenced by the increase in hydrogen production associated with higher temperatures, pressures and residence times. According to Figures 5.18 and 5.19, the exergy efficiencies of this reactor system are greater than the energy efficiencies. This was reasoned to be due to the existence of the Carnot number in Eq. 5.6 via Eq. 5.7 that reduces the  $Ex_{\text{heat}}$  term such that it is less than the  $Q_{\text{in}}$  term. The consequence of this is that the exergy efficiencies are greater than the energy efficiencies under the experimental conditions investigated. When coupled with the fact that the exergy of hydrogen is approximately 97% of its LHV [43], exergy efficiencies can be higher than corresponding energy efficiencies. Maximum energy and exergy efficiencies of 16.9% and 20.3% respectively were obtained at 20.0 bar, 500.0°C, and 3.965s. Increasing residence time also increased the both energy and exergy efficiencies. This magnitude of first and second law

efficiency is slightly greater than the efficiency results (13.7%) reported by Kim et al. in [29]. This is in agreement with [15,28,41,42]. Like the energy and exergy ratios previously described, the maximum energy and exergy efficiencies coincidentally occurred with the conditions that allow for maximum hydrogen production.

### 5.3 Results for Transient Ammonia Concentration in the Raffinate Stream

This section discusses the effectiveness of the membrane reactor in its production of hydrogen via the decomposition of ammonia. The minimization of ammonia concentration in the raffinate stream was determined to be a meaningful result for both thermodynamic and environmental reasons. The effects of operating temperature, pressure and residence time on transient ammonia concentration in the raffinate stream are illustrated in Figures 5.13 through 5.18.

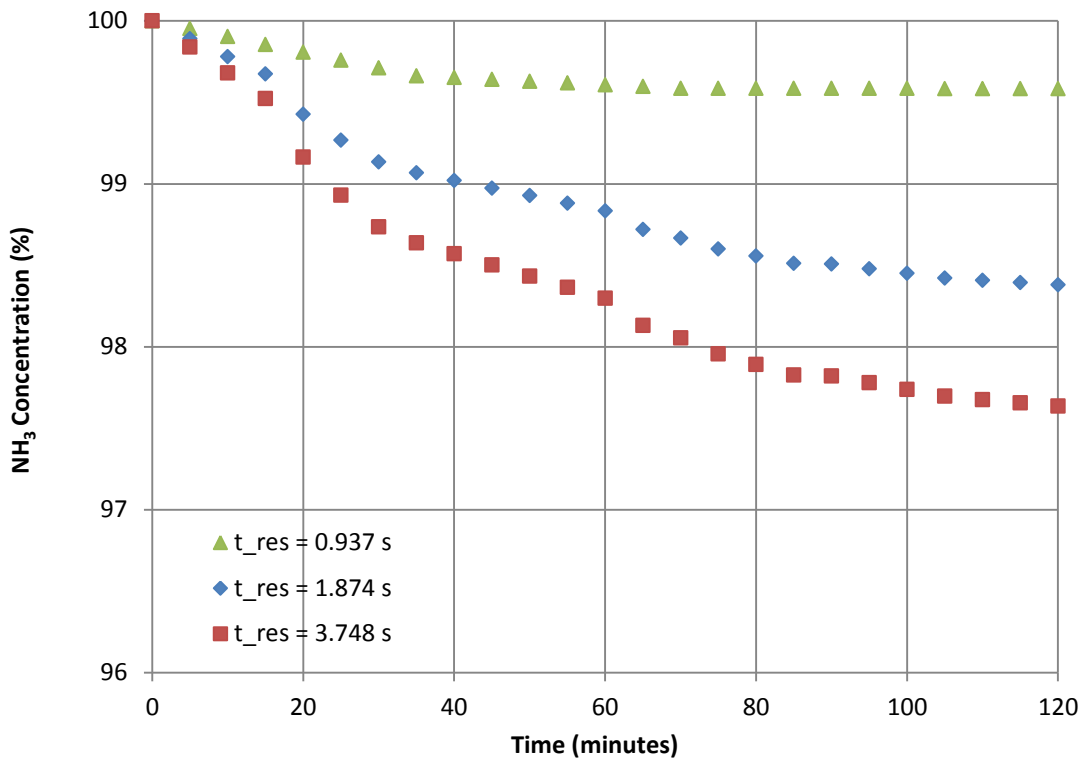


Figure 5.21: NH<sub>3</sub> concentration vs. time for 400°C, 5.0 bar and three residence times.

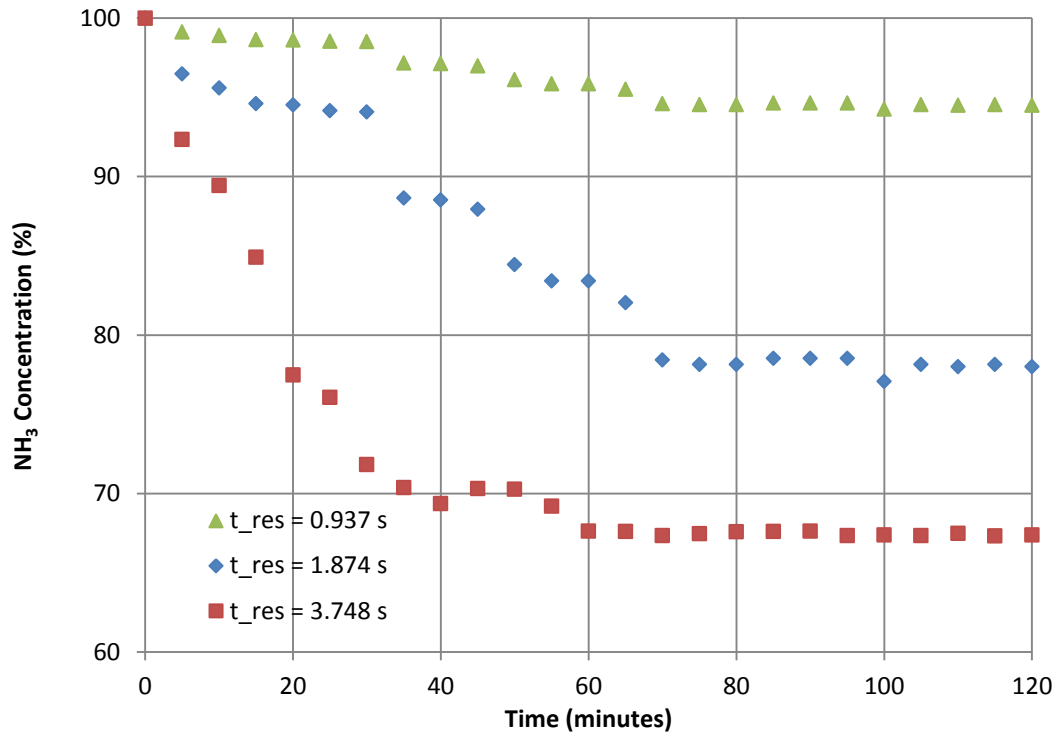


Figure 5.22:  $\text{NH}_3$  concentration vs. time for  $500^\circ\text{C}$ , 5.0 bar and three residence times.

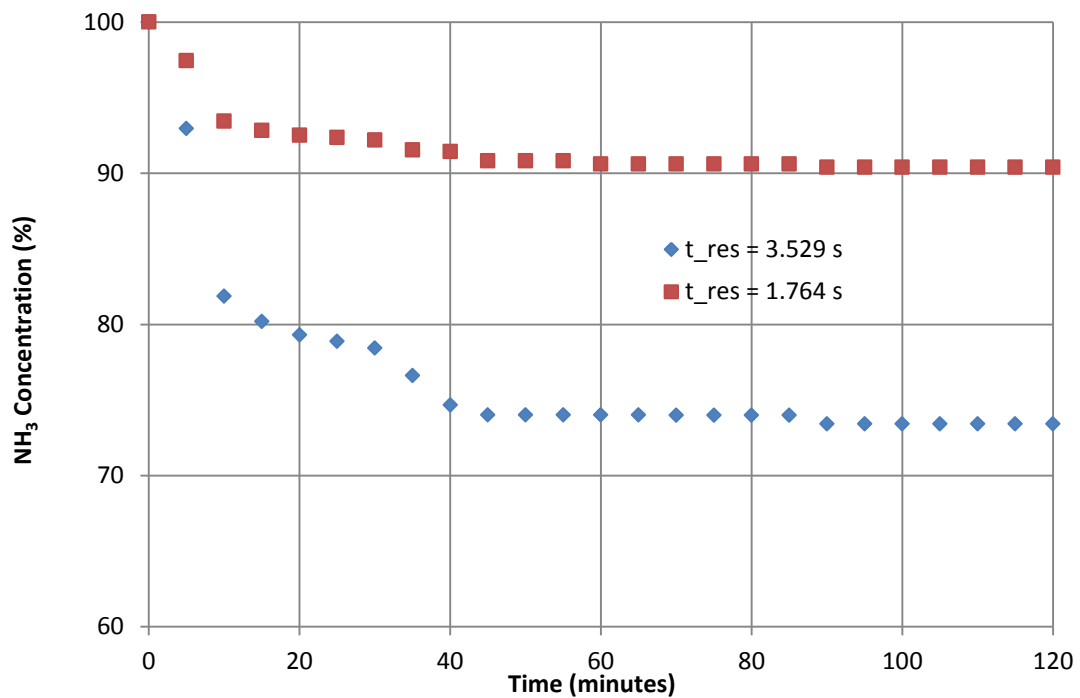


Figure 5.23:  $\text{NH}_3$  concentration vs. time for  $400^\circ\text{C}$ , 10.0 bar and two residence times.

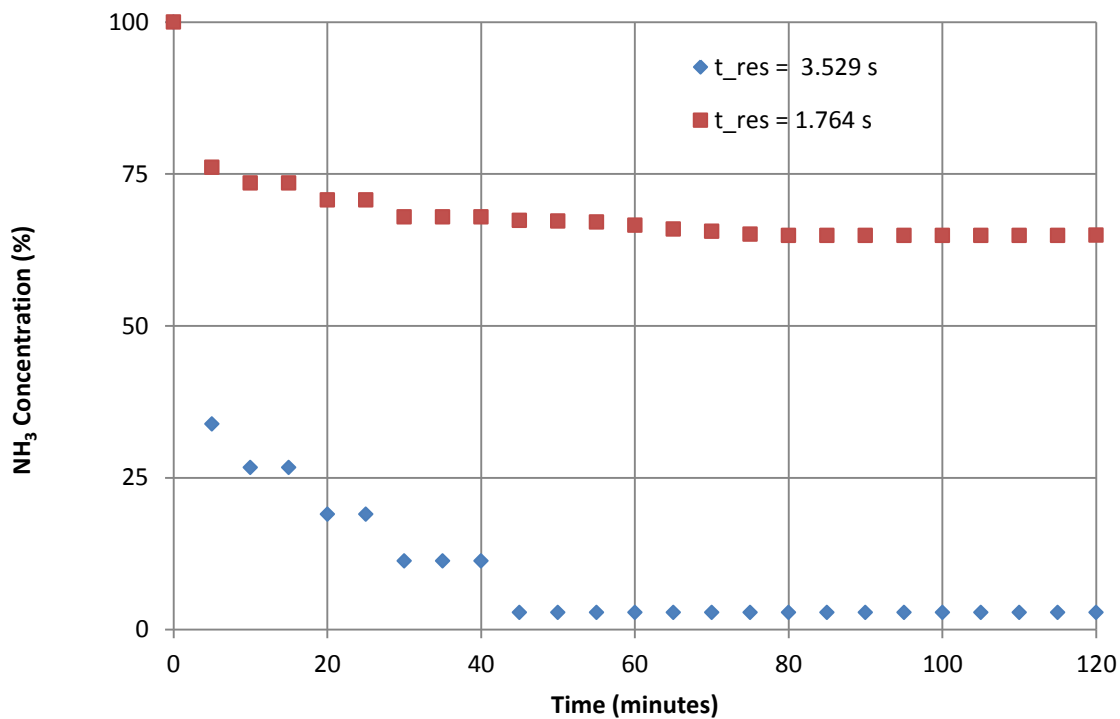


Figure 5.24: NH<sub>3</sub> concentration vs. time for 500°C, 10.0 bar and two residence times.

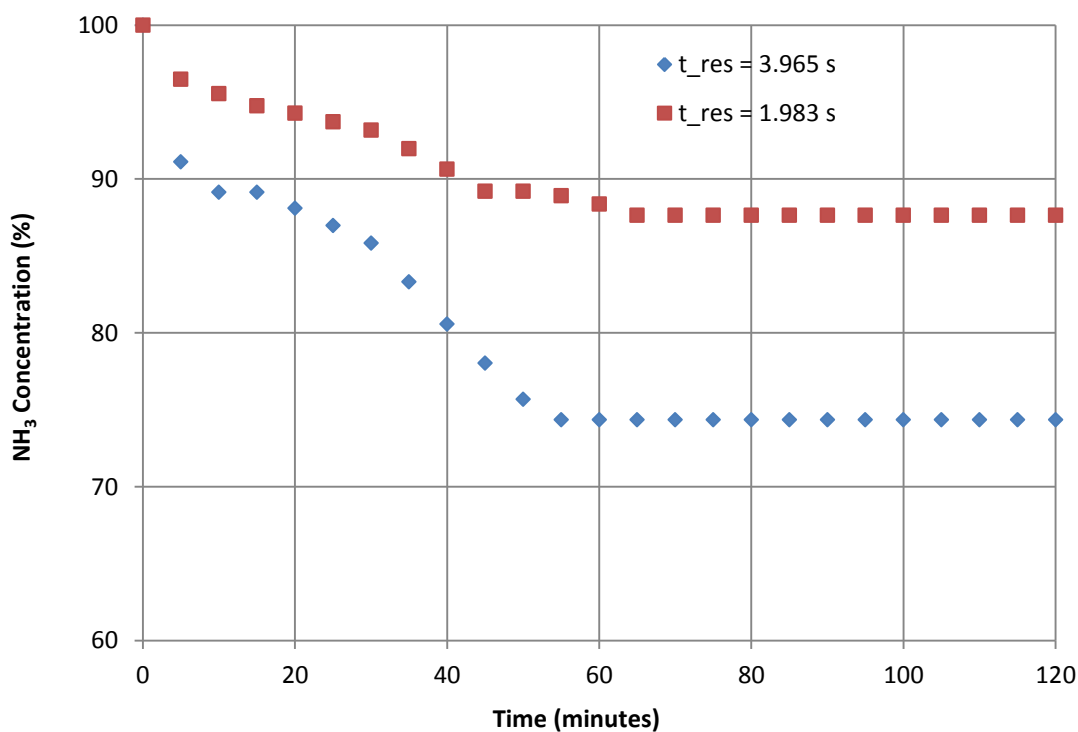


Figure 5.25: NH<sub>3</sub> concentration vs. time for 400°C, 20.0 bar and two residence times.

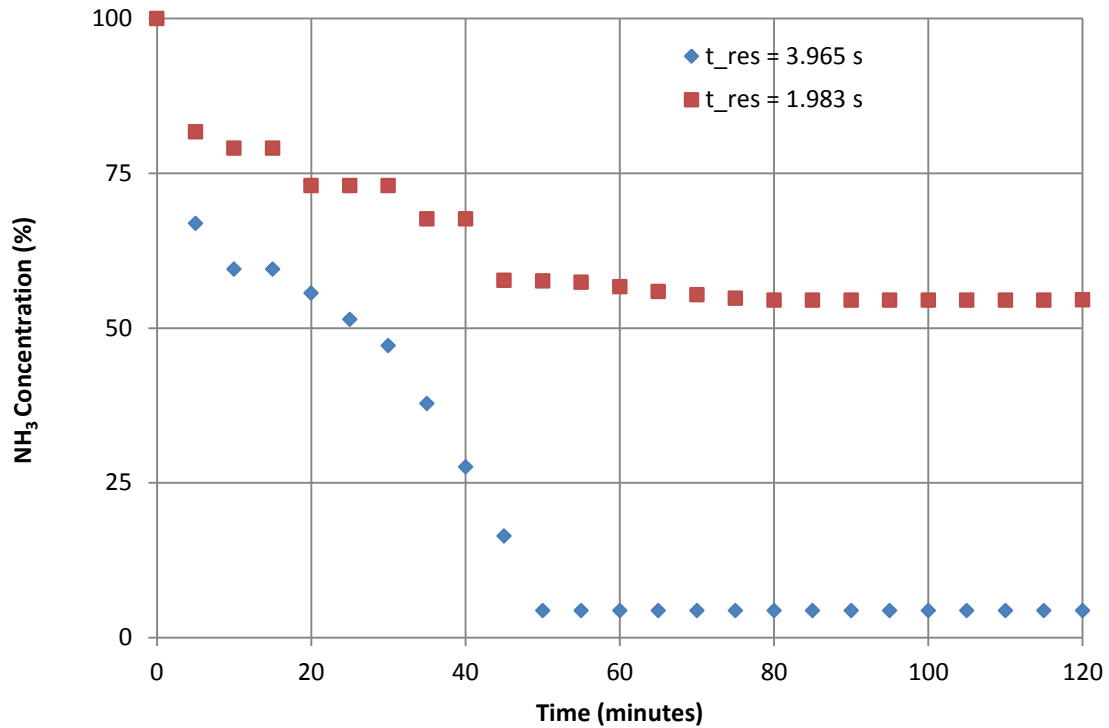


Figure 5.26: NH<sub>3</sub> concentration vs. time for 500°C, 20.0 bar and two residence times.

Figures 5.21 through 5.26 illustrate the transient ammonia conversion for the experimental conditions investigated. Figures 5.24 and 5.26 correlate particularly well with Figure 3.12 and illustrate that high temperature and pressure cause the reaction to move as far towards equilibrium as possible and minimizes the reactant concentration in the product stream. The transient ammonia concentration in the raffinate stream was found to decrease exponentially with time and reach a minimum value after anywhere between 40 to 60 minutes. This illustrates a shorter “warm up” time for a reactor operating at higher pressures and temperatures. The existence of a transient period before the onset of steady state is due to unsteady heat transfer between the reacting flow and the hot reactor walls. When the heat transfer to the reacting flow has reached a state of quasi-equilibrium, then steady state occurs. When the residence time was increased by increasing the ammonia inlet pressure, the time required to reach the minimum ammonia concentration in the raffinate stream was observed to be less and the negative concentration – time gradient was steeper. The effect of increased temperature was also found to result similar behaviour. This information illustrated that the thermodynamics of the ammonia decomposition reaction favoured high temperature and pressure in a membrane reactor [15 – 20].

## 5.4 Results for Transient Ammonia Conversion Efficiency

The transient ammonia conversion percentage is closely tied to but inversely related to the transient ammonia concentration in the raffinate stream. The following equation was found in the literature [44]. It is given as follows:

$$\eta_{NH_3}(t) = \frac{[1 - C_{NH_3,out}(t)]}{C_{NH_3,in}(t)} = 100 * \left(1 - \frac{C_{NH_3,out}(t)}{C_{NH_3,in}(t)}\right) \quad (5.2)$$

The above equation requires only two variables; the inlet and outlet ammonia concentrations, respectively. The outlet ammonia concentrations can be obtained by using the measured values for the raffinate steam with the balanced chemical equation. Figures 5.27 through 5.32 present the ammonia conversion profiles as a function of time for the experimental conditions investigated.

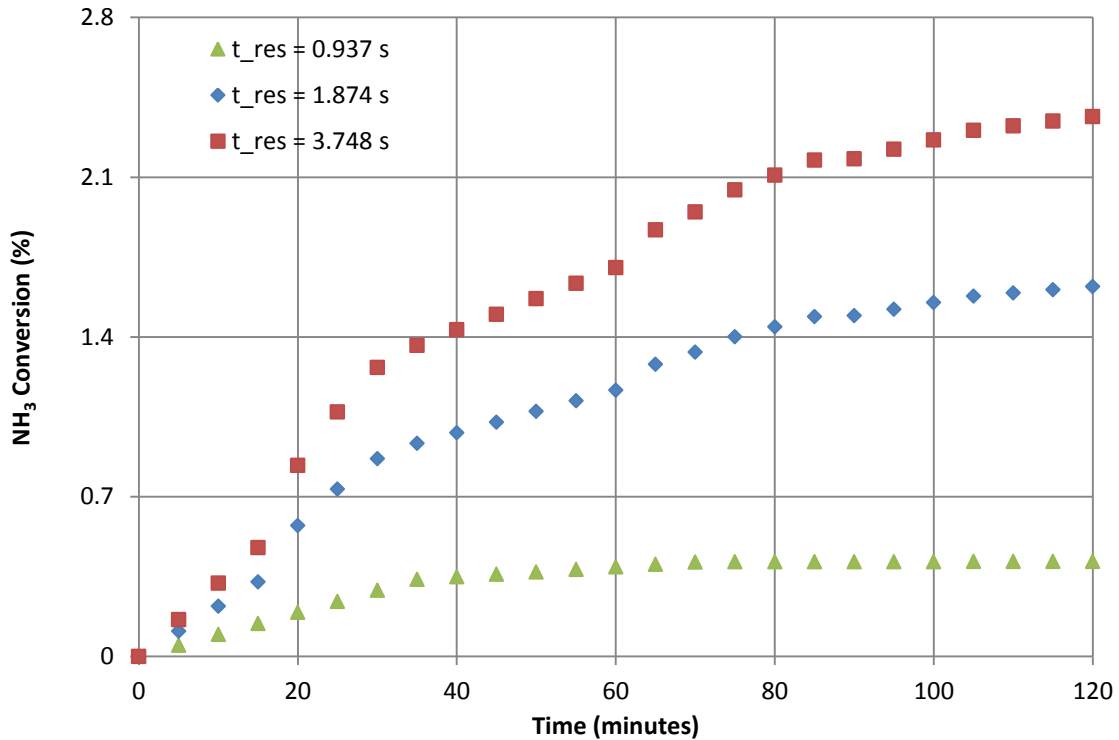


Figure 5.27: NH<sub>3</sub> conversion vs. time for 400°C and 5.0 bar for three residence times.

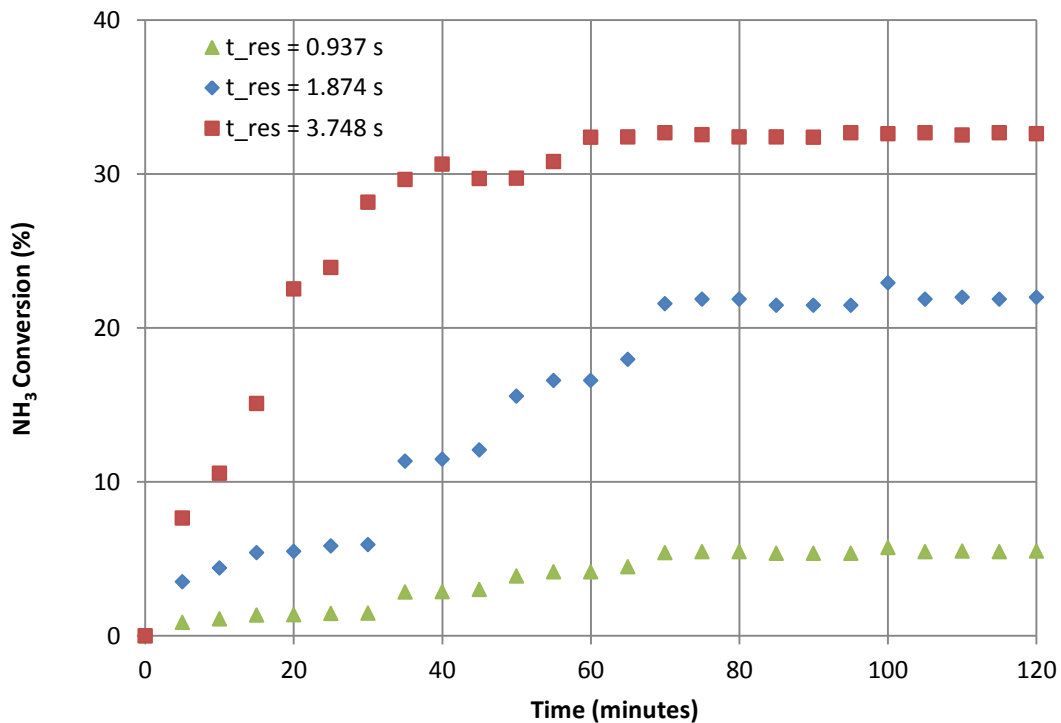


Figure 5.28:  $\text{NH}_3$  conversion vs. time for  $500^\circ\text{C}$  and 5.0 bar for three residence times.

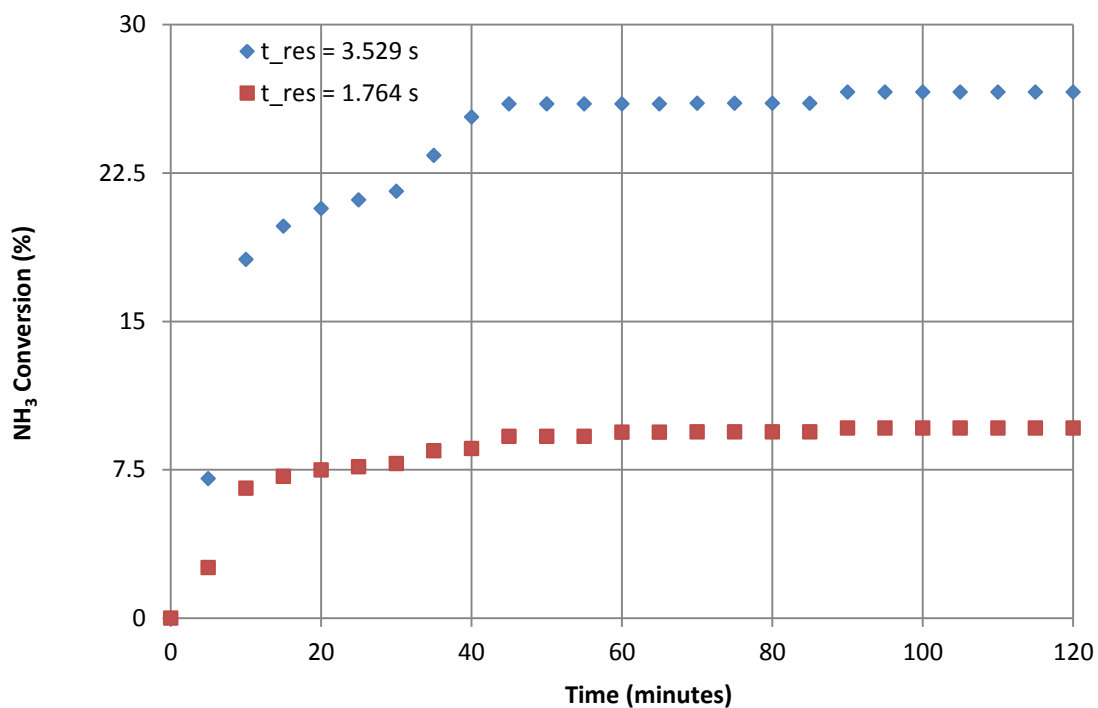


Figure 5.29:  $\text{NH}_3$  conversion vs. time for  $400^\circ\text{C}$  and 10.0 bar for two residence times.

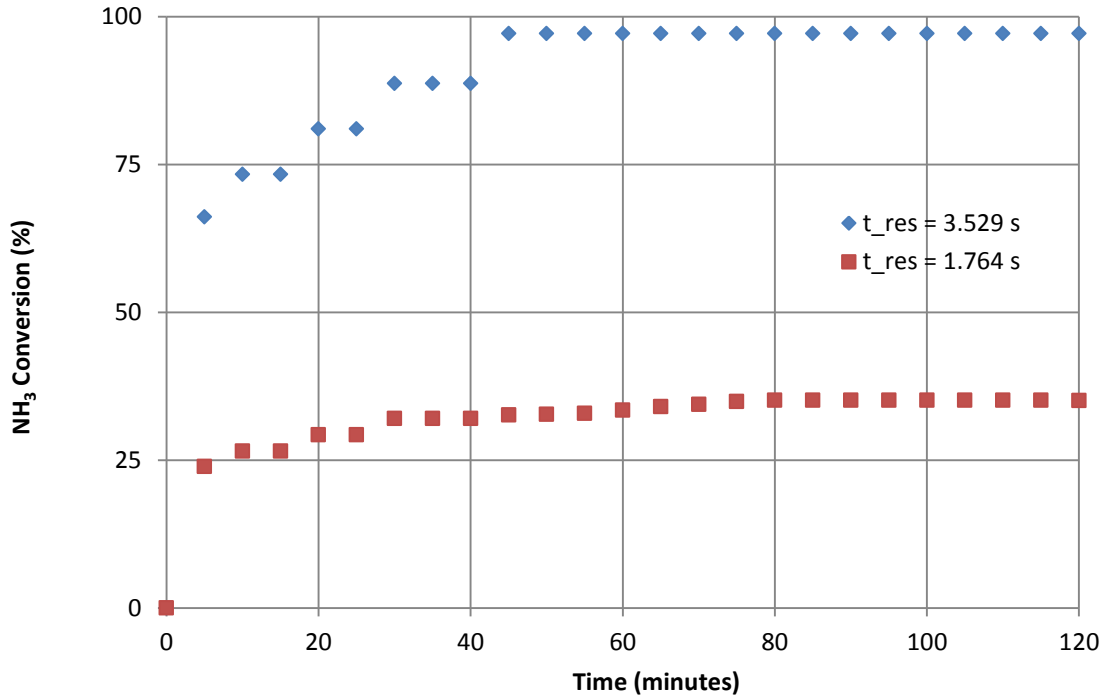


Figure 5.30: NH<sub>3</sub> conversion vs. time for 500°C and 10.0 bar for two residence times.

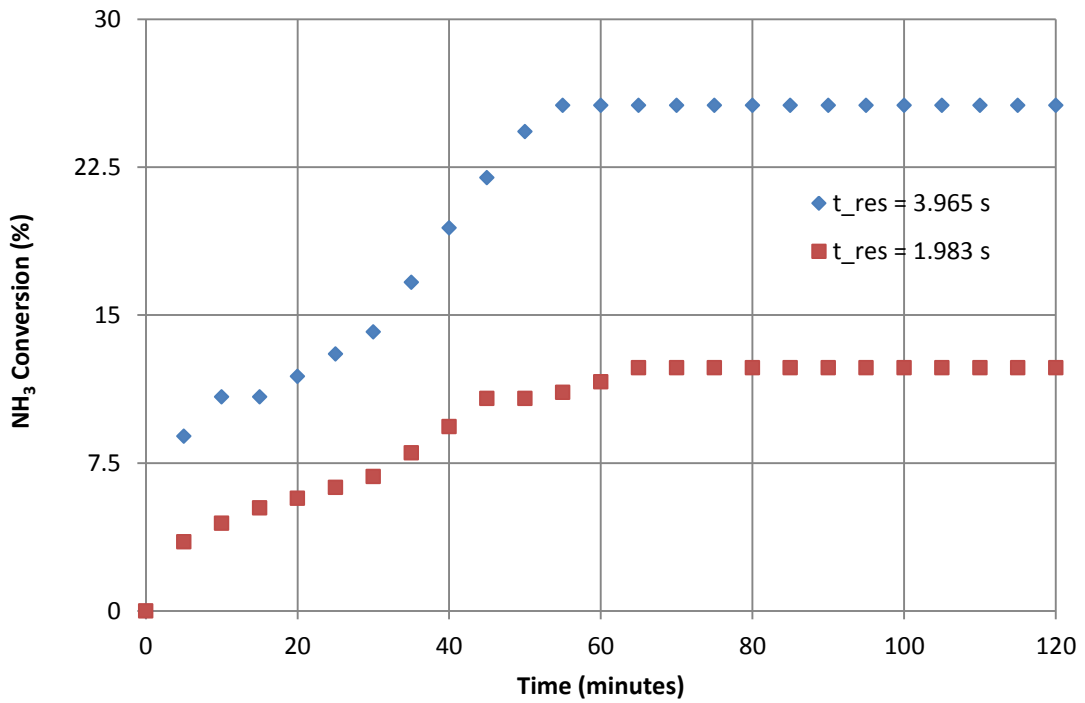


Figure 5.31: NH<sub>3</sub> conversion vs. time for 400°C and 20.0 bar for two residence times.

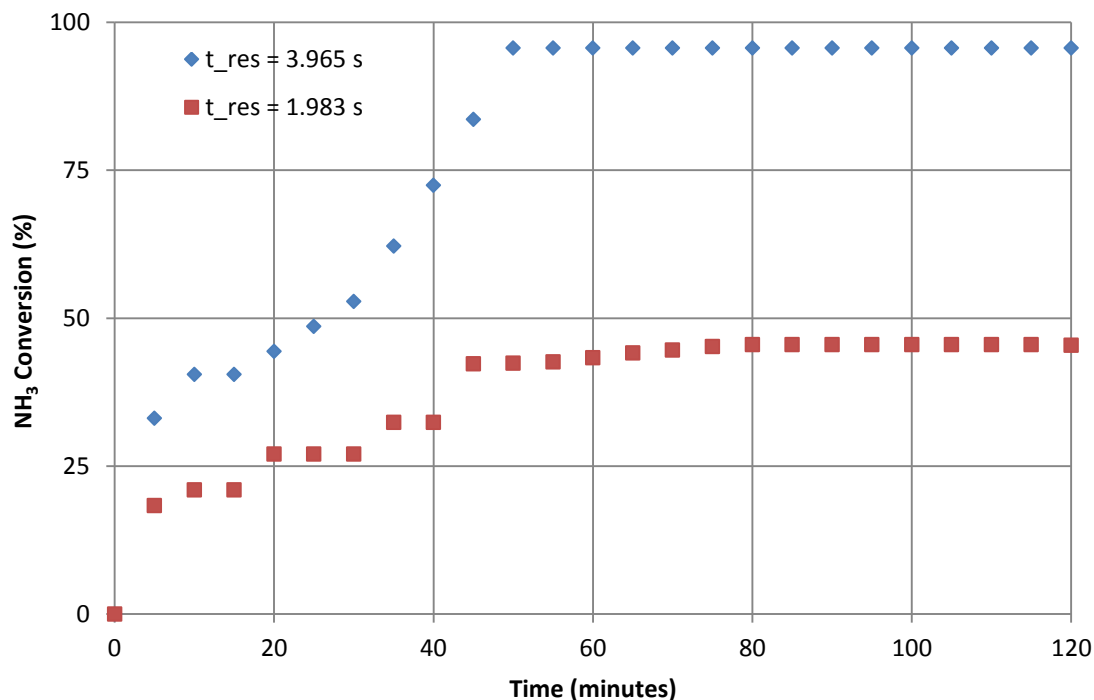


Figure 5.32: NH<sub>3</sub> conversion vs. time for 500°C and 20.0 bar for two residence times.

Figures 5.27 through 5.32 display the results for transient ammonia conversion for the experimental conditions investigated in this thesis work. Once again, an increase in temperature, pressure, and residence time were found to result in large increases in ammonia conversion. When the experimental runs with a pressure of 5.0 bar and a residence time of 1.874 seconds but increasing the operating temperature from 400.0°C to 500.0°C, the ammonia conversion increased by a factor of approximately 13.75. When this was repeated with a pressure of 10.0 bar an increase in ammonia conversion by a factor of approximately 3.5 was observed. When this was repeated again with a pressure of 20.0 bar, an increase in ammonia conversion of approximately 1.7 was observed. That being said, the nature of chemical equilibrium does not allow for 100.0% ammonia conversion. However, the experiments conducted in this thesis work obtained maximum ammonia conversions of approximately 97.18% and 95.64% at 500.0°C, for 10.0 bar and 20.0 bar, respectively. Also, Figures 5.30 and 5.32 compare well with the predicted results in Figure 3.12. This further shows that high temperature, pressure, and residence time pushes the ammonia decomposition further towards equilibrium via hydrogen removal. This was in good agreement with [12, 20, 29, 41] and illustrated the benefits of membrane reactors as in [12, 15].

## 5.5 Results for Transient Ammonia Decomposition Rate

The results for the empirical ammonia decomposition rate were derived from the mass balance on the hydrogen production rate. A stoichiometric mass ratio of approximately  $0.178\text{H}_2 : 1.0\text{NH}_3$  of hydrogen to ammonia was applied to the hydrogen production rate to determine the minimum ammonia decomposition rate. Figures 5.33 through 5.38 display the results from the experimental conditions studied.

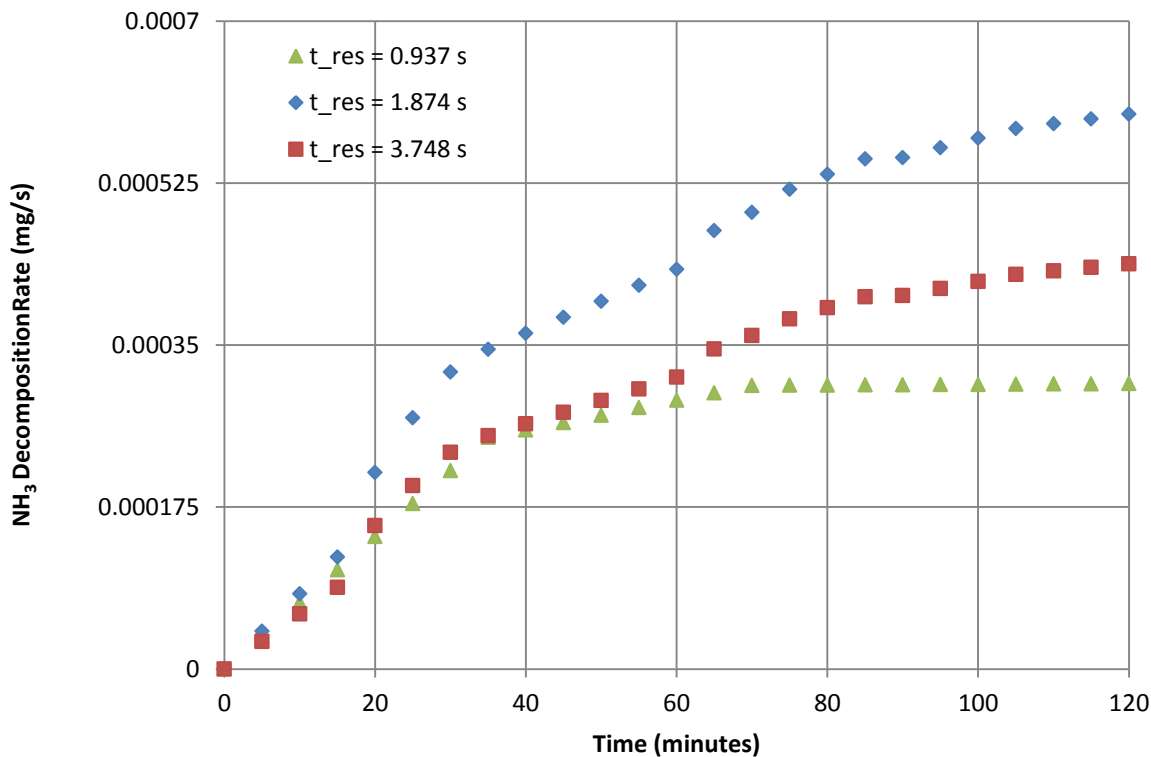


Figure 5.33:  $\text{NH}_3$  decomposition rate vs. time for  $400^\circ\text{C}$  and 5.0 bar for three residence times.

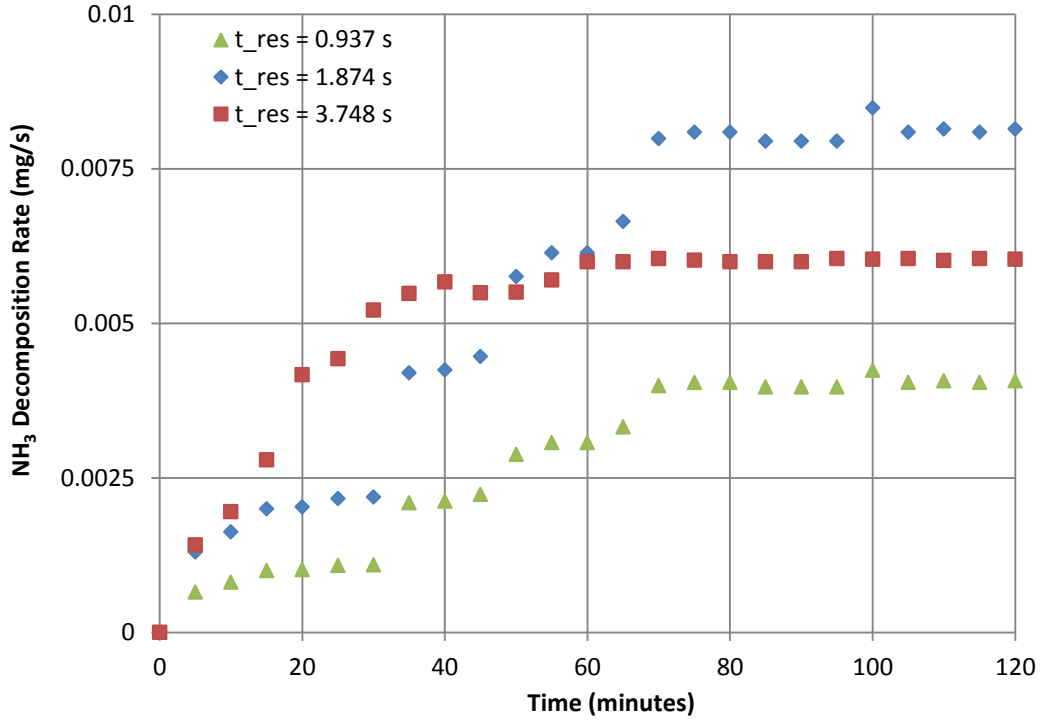


Figure 5.34:  $\text{NH}_3$  decomposition rate vs. time for  $500^\circ\text{C}$  and 5.0 bar for three residence times.

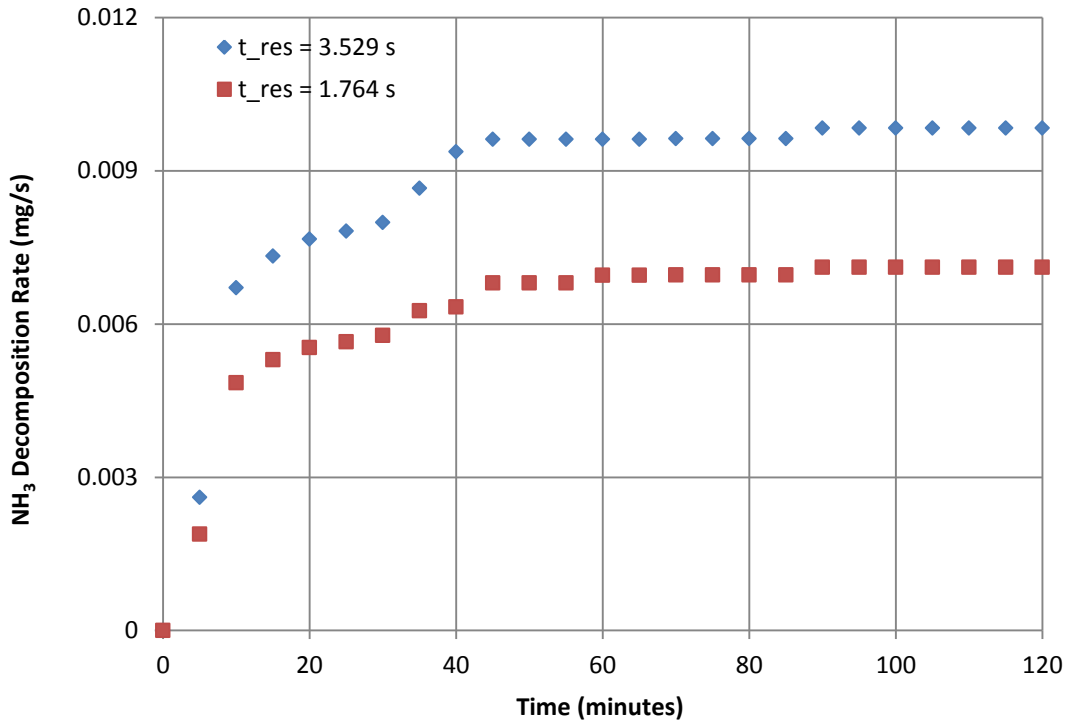


Figure 5.35:  $\text{NH}_3$  decomposition rate vs. time for  $400^\circ\text{C}$  and 10.0 bar for two residence times.

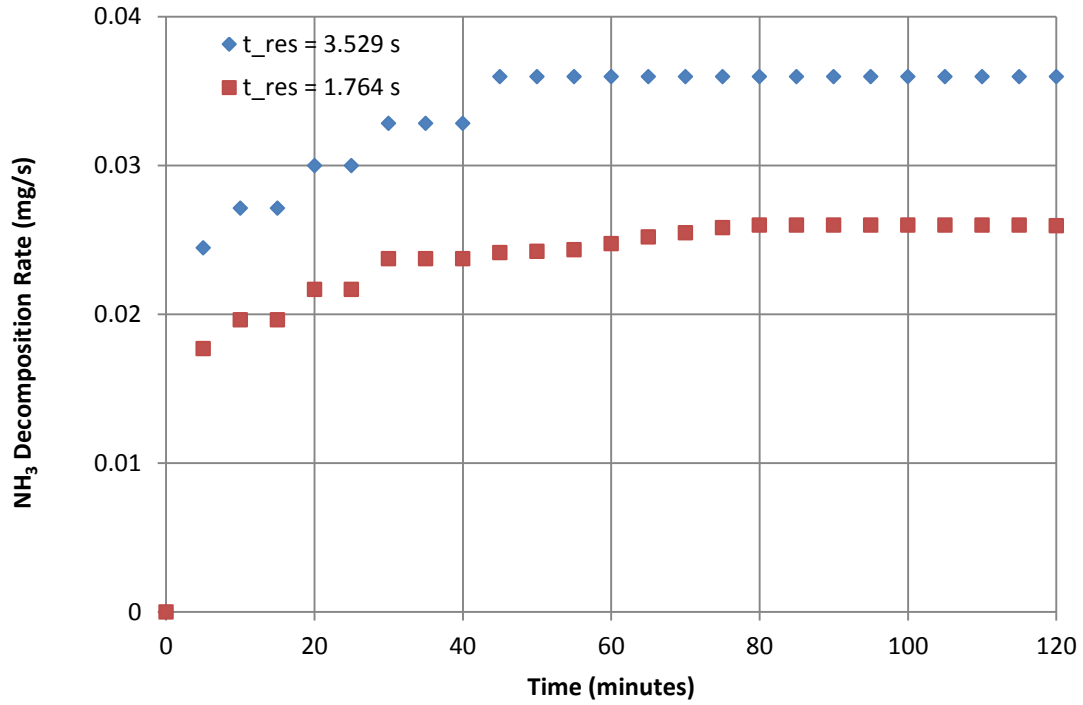


Figure 5.36: NH<sub>3</sub> decomposition rate vs. time for 500°C and 10.0 bar for two residence times.

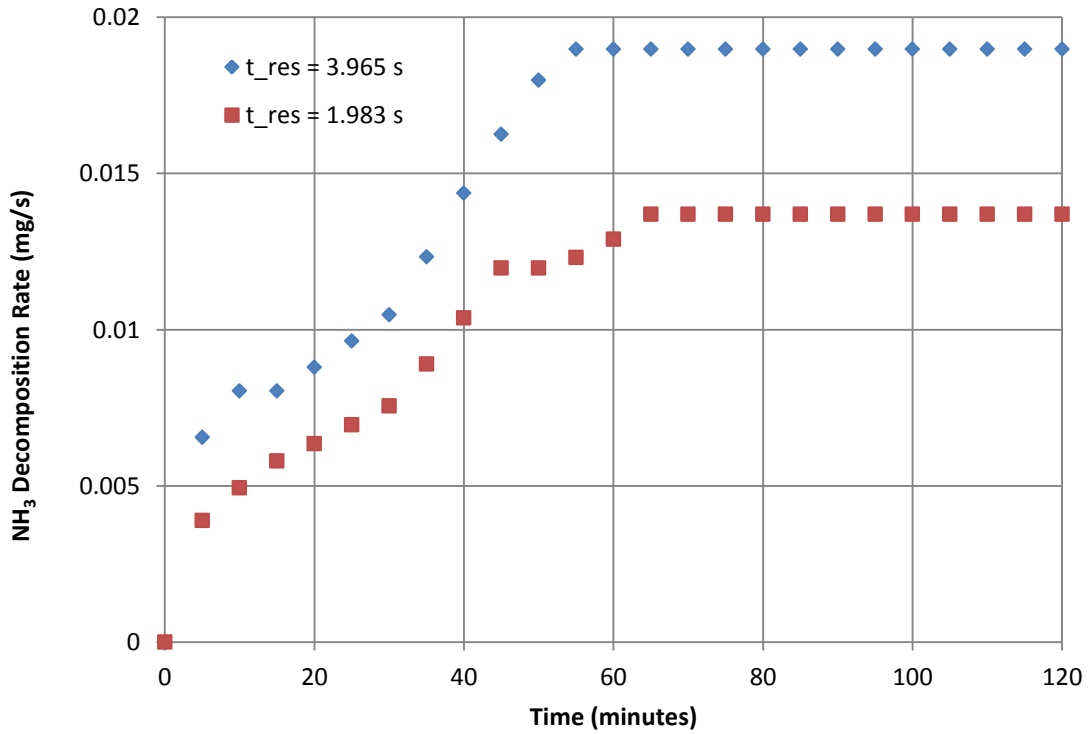


Figure 5.37: NH<sub>3</sub> decomposition rate vs. time for 400°C and 20.0 bar for two residence times.

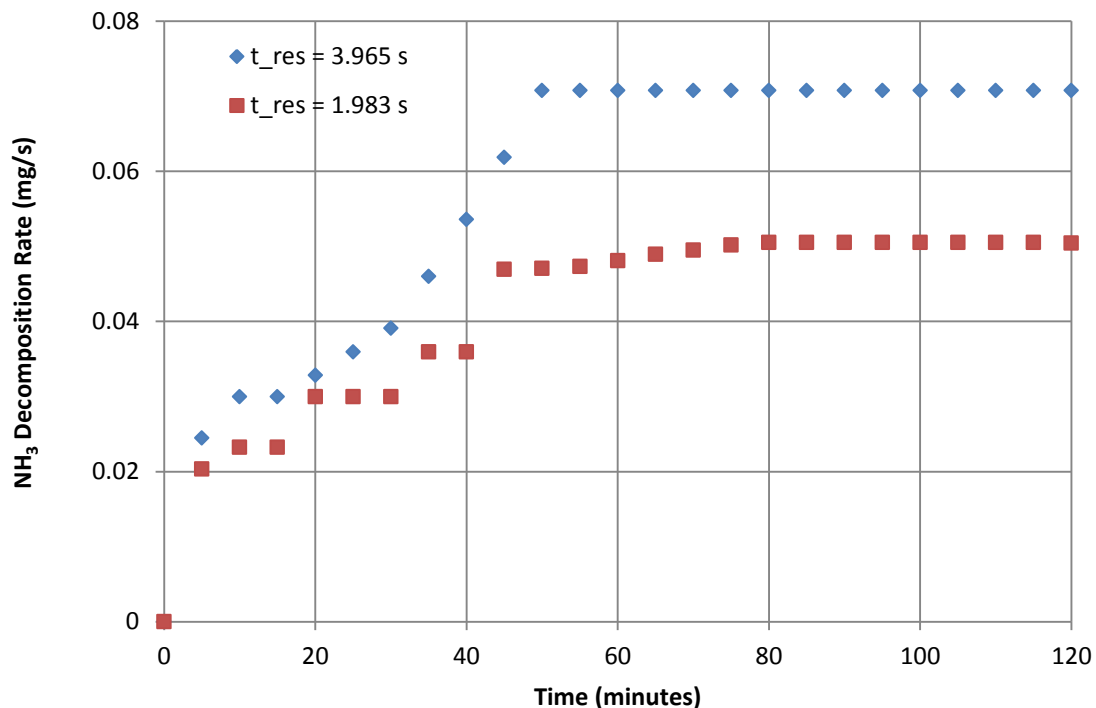


Figure 5.38: NH<sub>3</sub> decomposition rate vs. time for 500°C and 20.0 bar for two residence times.

Figures 5.33 through 5.38 display the transient ammonia decomposition rate for the experimental conditions investigated. The transient decomposition rate was determined from the hydrogen production rate as previously mentioned. It was found that the ammonia decomposition rate increased with both an increase in temperature, pressure and residence time. This was to be expected due to the increases in both hydrogen production and ammonia conversion. This was determined to be by extension, and can also be seen in [11,12,15,16]. The increase in decomposition rate was determined to be for the same reasons as the increase in hydrogen production, ammonia conversion and energy ratio. The reaction rate was found to increase with temperature and residence time. For example, at 5.0 bar and a residence time of 1.764s the reaction rate increased by a factor of roughly 13.0 when the temperature was increased from 400.0°C to 500.0°C. When this had been repeated at an operating pressure of 10.0 bar, the reaction rate increased by a factor of only 3.7 but was increased by a factor of roughly 12.0 with a doubling of the operating pressure. Similar behaviour was observed when the residence times were doubled. Also, the reaction rate was observed to increase with an increase of operating pressure. Interestingly enough, when the residence time was doubled, the effect of doubling pressure translated into a doubling of reaction rate.

## 5.6 Commentary on Transient Behaviour

In hindsight, the reactor's performance during the experimental work had been observed to have two types of behaviour. This can be divided into two sections.

- transient ( $d[\ ]/dt \neq 0$ ): “warm up”;
- steady state ( $d[\ ]/dt = 0$ ): “operational”.

If a system such as the one shown in Figure 5.46 was to be built, then the “warm” up should be minimized in order to maximize hydrogen production as quickly as possible. Using hydrogen production data and ammonia concentration data at 10.0 bar and 20.0 bar to generate a small graph that illustrates the effect of residence time on threshold time.

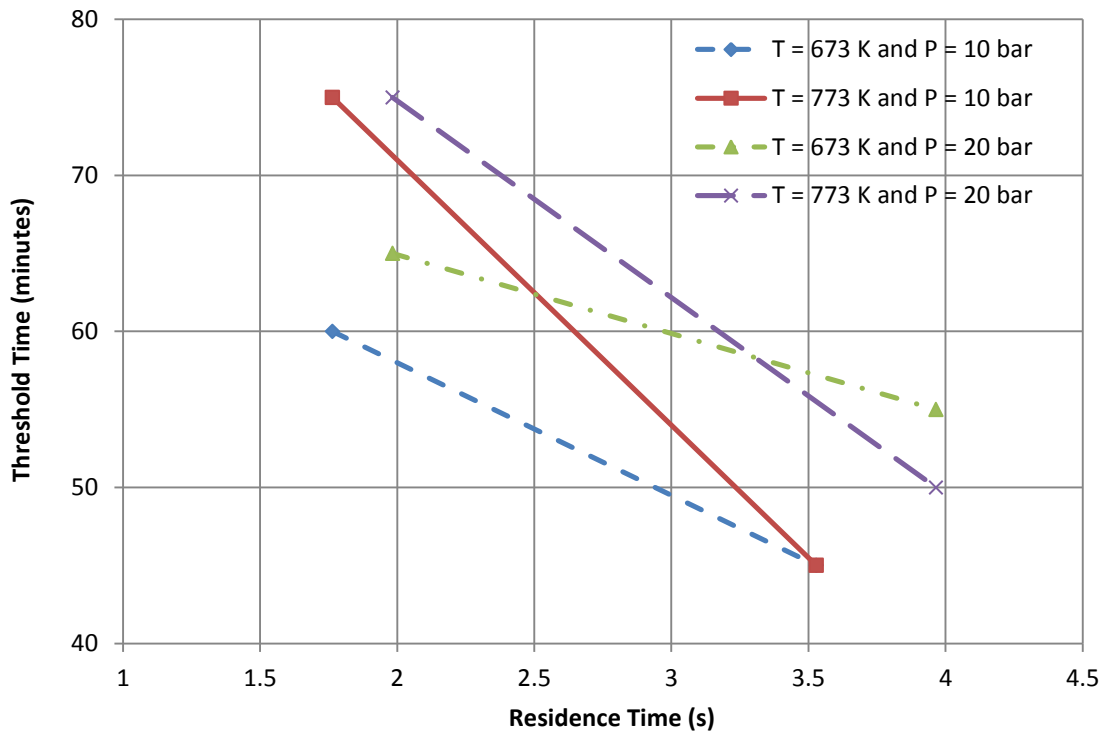


Figure 5.39: The effect of residence time, pressure and temperature on threshold time.

Figure 5.39 illustrates the positive effect of increasing residence time, pressure, and temperature on threshold time. It can clearly be seen that threshold time decreases as residence time increases. This is due to the decrease in heat transfer rate to the flow due to the slower flow which allows for greater hydrogen production at a lower threshold time. The lower temperature also shortened the threshold time due to a decrease in heat transfer rate as well. However, this decrease in heat transfer was due to a smaller temperature difference between the reactor and the

environment at  $\sim 22^{\circ}\text{C}$ . Due to these facts, one potential method to reduce the threshold time even further would be to slowly increase the ammonia flow into the reactor as opposed to allowing it all to flow at a constant rate from the beginning. In an automotive or industrial application, a mass flow controller with a gentle ramp function to slowly increase ammonia feed flow over time could potentially work.

### 5.7 Results for Catalyst Surface Morphology

In this section, the results displaying changes in catalyst surface morphology due to being exposed to reacting ammonia at high temperatures ( $400.0^{\circ}\text{C} - 500.0^{\circ}\text{C}$ ) and pressures ( $5.0 - 20.0$  bar). Figures 5.40 through 5.42 show the unexposed catalyst particles at different magnifications whereas Figures 5.43 through 5.45 show the catalyst particles after exposure to reacting ammonia.

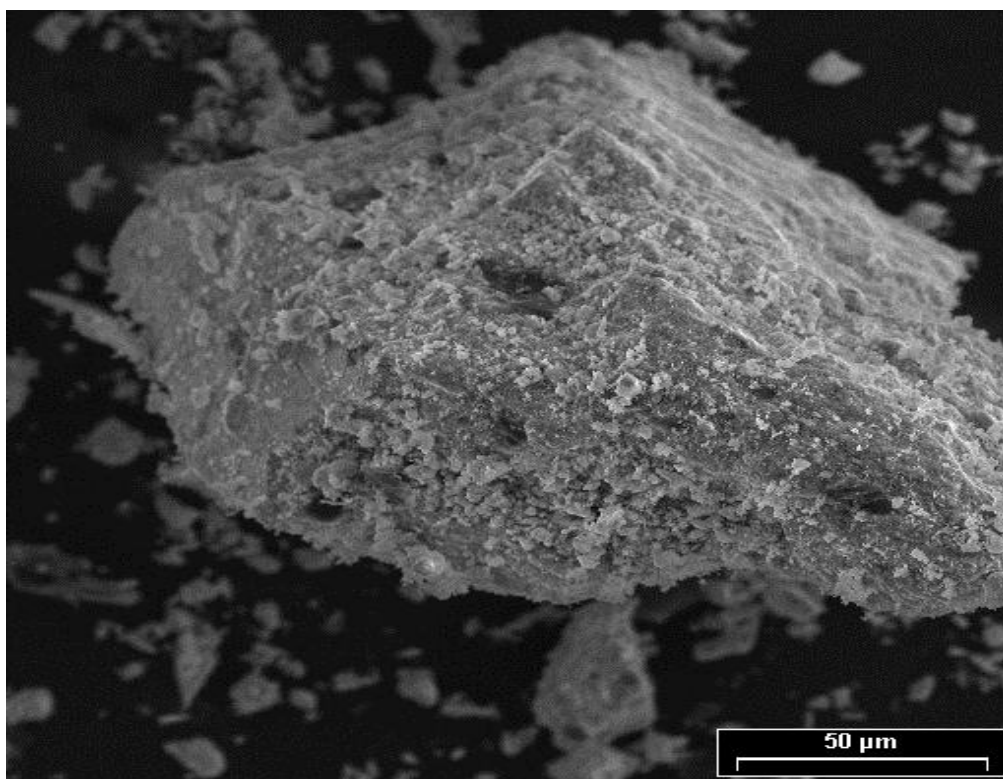


Figure 5.40 Magnified SEM image of an unexposed  $\text{Ni}_2\text{O}_3$  catalyst particle ( $50\ \mu\text{m}$ ).

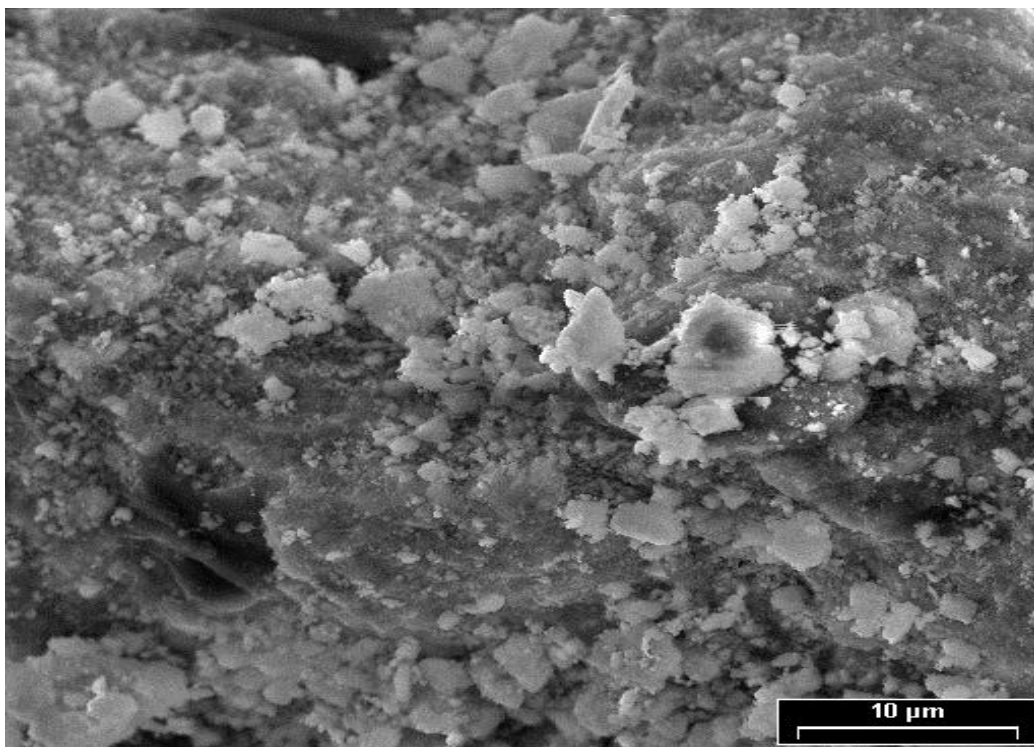


Figure 5.41: Magnified SEM image of an unexposed  $\text{Ni}_2\text{O}_3$  catalyst particle (10  $\mu\text{m}$ ).

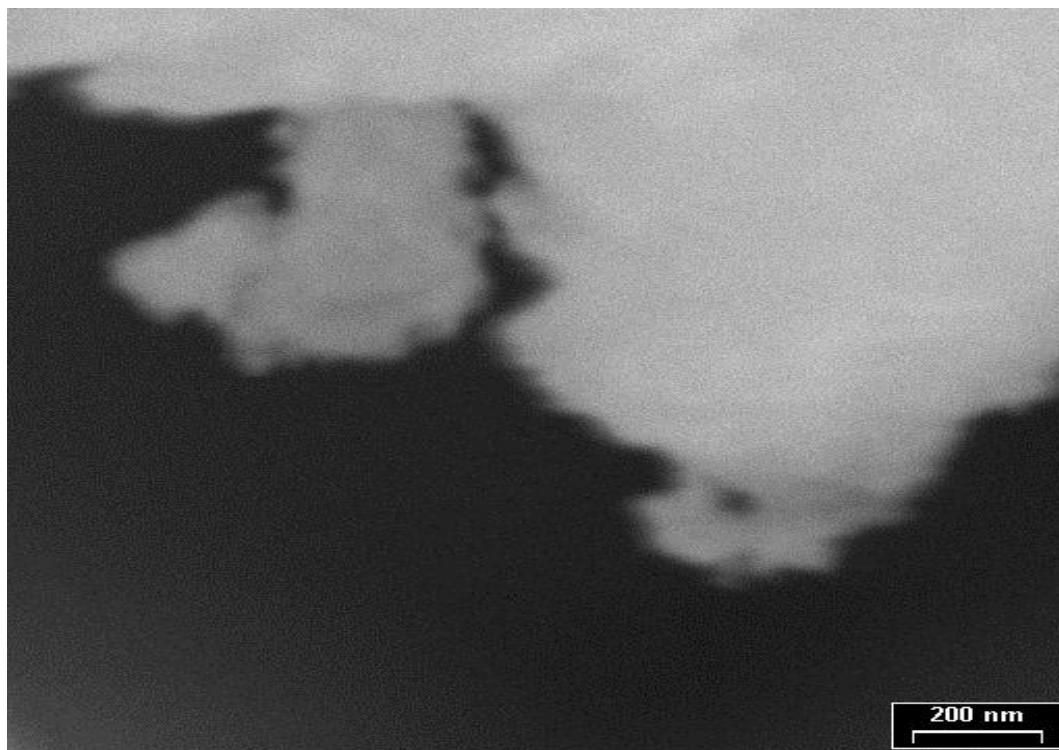


Figure 5.42: Magnified SEM image of an unexposed  $\text{Ni}_2\text{O}_3$  catalyst particle (200 nm).

The SEM images of a catalyst particle are shown in Figures 5.39 through 5.41. The jagged looking edges are a common physical characteristic of metal oxides. Also, these extensions cause the effective surface area and residence time for a catalytic reaction to increase [31]. When these are combined with the nature of a catalyst the overall reaction rate increases compared to the case in which no catalyst is used at all.

After the experiments were finished, the catalyst powder was removed from the reactor and taken to a scanning electron microscope for qualitative analysis. In Figures 5.42 through 5.44, the magnified SEM images of exposed  $\text{Ni}_2\text{O}_3$  catalyst particles are shown.

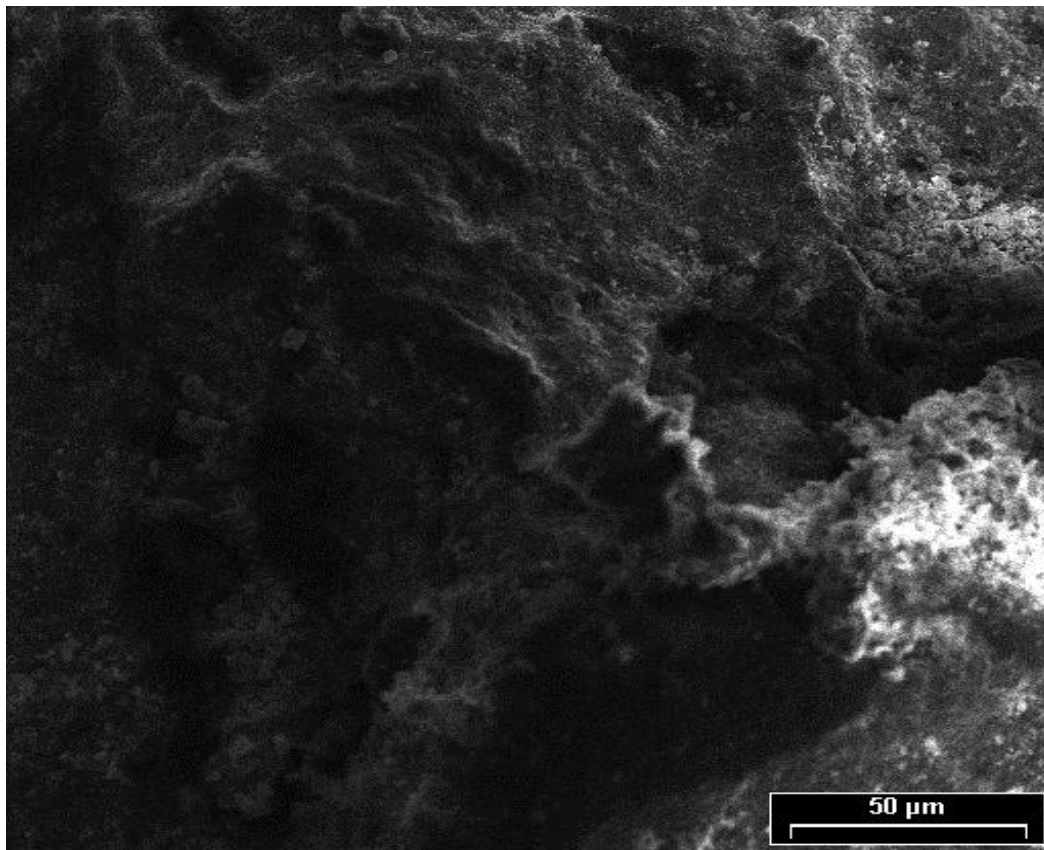


Figure 5.43: Magnified SEM image of an exposed  $\text{Ni}_2\text{O}_3$  catalyst particle (50  $\mu\text{m}$ ).

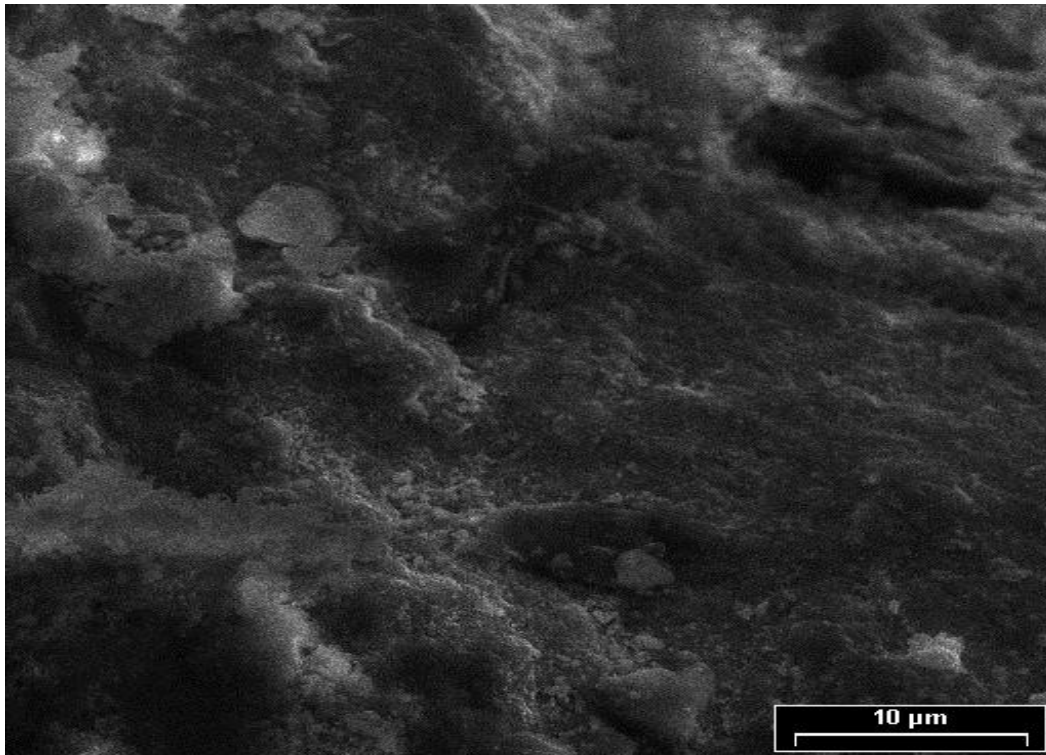


Figure 5.44: Magnified SEM image of an exposed  $\text{Ni}_2\text{O}_3$  catalyst particle (10  $\mu\text{m}$ ).



Figure 5.45: Magnified SEM image of an exposed  $\text{Ni}_2\text{O}_3$  catalyst particle (200 nm).

Figures 5.42 through 5.44 show pictures taken with an SEM of  $\text{Ni}_2\text{O}_3$  catalyst particles that have been exposed to reacting ammonia at temperatures varying from  $400.0^\circ\text{C}$  to  $500.0^\circ\text{C}$  and pressures varying from 5.0 bar to 20.0 bar. Most noticeably, a smoothing of the particle surface can be observed. A phenomenon called Ostwald ripening was determined to be a probable explanation for this. In the presence of ammonia,  $\text{Ni}_2\text{O}_3$  may form a black nickel hydroxide -  $\text{Ni}(\text{OH})_3$  [45], which then in the presence of excessive ammonia may form a bright blue nickel based hexa amine ion. Failed experiments in the beginning had produced a blue liquid which clogged the 65.0mm rotameter in the raffinate stream. This was determined to be  $\text{Ni}(\text{NH}_3)_6^{+2}$  in the liquid phase due to its blue colour and ammonia smell [46]. Due to the reactor temperature being  $400.0^\circ\text{C}$  to  $500.0^\circ\text{C}$ , this must have been in the gas phase initially. Since the reaction is taking place on the jagged edges of the particle surface (seen in Figures 5.40 through 5.42) the gas flow may have redistributed the small particles that constitute extensions to the larger catalyst surface via solution. This is known as Ostwald ripening [47] and could potentially account for the smoothing of the particle surface observed in Figures 5.43 through 5.45. Ostwald ripening occurs to increase the stability of a compound by reducing its free energy via dissolution of smaller particles. Another piece of evidence that supports this line of reasoning is the charge interference observed when taking pictures with the SEM. This is generally common for organic materials and/or materials which are not electrically conductive. Nickel hydroxide is a metal salt and by definition would not be electrically conductive. Therefore, there is evidence of nickel hydroxide formation followed by Ostwald ripening that potentially accounts for the observed smoothing of the catalyst surface when exposed to ammonia at the high temperatures and pressures in this thesis work.

## **5.8 Results of Uncertainty Analysis**

In any experimental work there are errors that propagate uncertainties and biases in the data. The reasons for these errors are numerous. A couple reasons were speculated to be the unexpected human errors during the running of an experiment, inherent errors in the experimental methods used and inaccuracies of instrumentation.

The method of Kline and McClintock is mentioned in [48]. It is a function of the experimental error as a plus-minus tolerance and the partial derivative of the equation describing the data. Mathematically, it is expressed as follows:

$$W_r = \sqrt{\sum_i [w_i * \left(\frac{\partial y_i}{\partial x_i}\right)]^2} \quad (5.3)$$

The steady state data points were selected and Eq. 5.3 was applied to determine the uncertainty inherent in the calculated and measured data at steady state. The uncertainty propagation module in EES was used to determine the magnitude and distribution of uncertainties during steady state. Finally, these uncertainties were tabulated and placed in Appendix C for reference.

The sources of uncertainty in this experimental work were determined to be predominantly from the lack of forward control in the process design. The combination of a flow meter and needle valve introduced errors due a human operator. The percentage uncertainty was found to increase greatly with hydrogen production due to the relatively large error (+/- 2.0% - 4.0%) associated with the 65.0mm glass tube flow meters. The highest uncertainty values were found to be associated with ammonia concentration in the raffinate stream (see Appendix C). Due to this, the use of a gas chromatograph with thermal conductivity (GC-TCD) detector to determine transient ammonia concentrations more accurately. Moreover, calibrated digital flow meters should be put in place of the 65.0mm glass tube flow meters to increase accuracy in the future. That being said, the minimum uncertainty values were found to be associated with the ammonia flow rates due to the high accuracy (+/-1.5%) of the FMA-1812 flow meter. While the flow meter was very accurate, controlling the flow with a needle valve was not. That is a significant source of error.

## 5.9 Commentary on Environmental Impacts

While ammonia decomposition emits no CO<sub>2</sub>, it still has an environmental impact. That being said, the main negative environmental impact that can be mentioned of this experimental study is the potential for high ammonia concentrations in the raffinate stream. It has been shown that ammonia decomposition can be quite less than 100% complete and far removed from equilibrium. The highest ammonia concentration was determined to be approximately 99.5% while the lowest ammonia concentration was determined to be approximately 4.2%. These are 995,000 ppm and 42,000 ppm, respectively. These concentrations are very high and could cause environmental damage via dissolving in water, mixing into fresh water and coming into contact with fish, humans, and plant life. Therefore, these high concentrations should be controlled with

better process design that includes ammonia recycling in order to have a closed loop ammonia flow system.

### **5.10 Potential Applications**

The potential applications of this technology are numerous. Two applications of this H<sub>2</sub> generation system from NH<sub>3</sub> could potentially be:

- Hydrogen generation for power generation purposes from a high temperature waste heat source. The waste heat could be supplied from sources such as: gas turbine, SOFC, or diesel power plants. All of the previously mentioned power plants have exhausts at temperatures of or greater than 600°C and would be able to meet the thermal demand of an NH<sub>3</sub> decomposition and separation reactor [49]. For this scenario to be realized, an exhaust gas to reactor heat exchanger must be designed and built to facilitate efficient heat transfer to the reactor.
- As a kind of extension from the first point, a membrane reactor system to produce hydrogen by the thermal decomposition of ammonia could also take place in either large scale marine or rail applications. This is envisioned to be a self – sustaining scenario where a fraction of the hydrogen energy produced would be fed back to decompose additional ammonia to sustain hydrogen production. A major point of interest pertaining to this scenario would be the very high energy ratio of the ammonia decomposition reaction. Thermodynamically, the ammonia decomposition reaction only requires approximately 13.0% - 15.0% of the hydrogen's calorific value. Due to this, if such a reactor system were to be coupled to a large, high efficiency, low speed engine as shown in Figure 5.46, then all the benefits of a hydrogen internal combustion engine as illustrated in [50,51] could be realized without all the hassles of storing gaseous hydrogen onboard.

### **5.11 Potential Design**

A membrane reactor system such as this would be favourable to integrate with either a SOFC or an internal combustion engine with little to no differences between them. Both generate hot exhaust gases that can be used to heat the reactor system and both require pure hydrogen to operate and a membrane reactor produces 99.999% pure hydrogen due to the strict hydrogen

selectivity of a palladium membrane. This last point eliminates the possibility of poisoning the fuel cell.

This section presents a potential design for application in the rail industry. Due to the plentiful space onboard trains, such a physically large design with many components would be best suited to a train. Furthermore, high displacement and low speed engines typically offer relatively low brake specific fuel consumption [52]. This is another point that could support the case of the integration of such a membrane reactor system into a train.

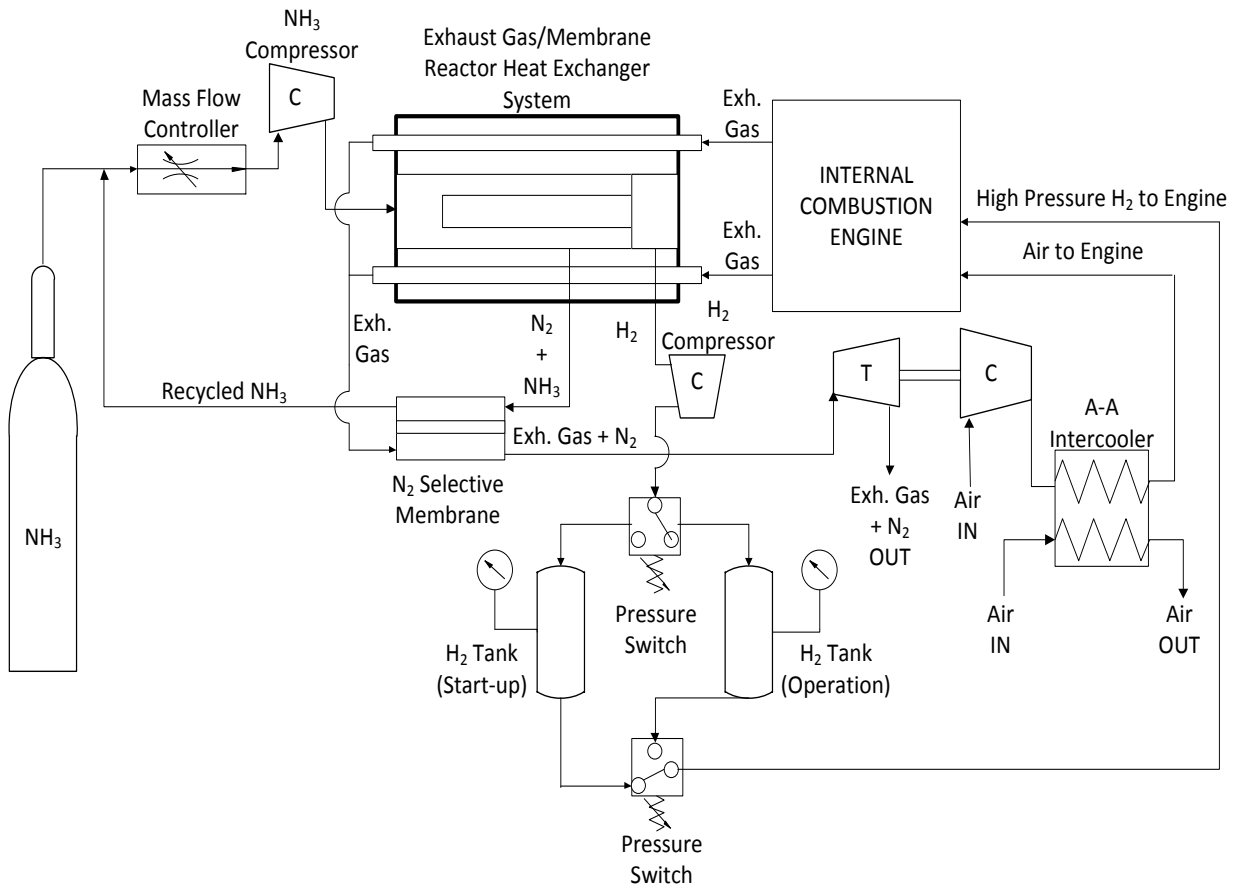


Figure 5.46: Potential design of an onboard  $\text{H}_2$  production system from  $\text{NH}_3$  decomposition for a rail application.

Figure 5.46 is a schematic of a potential design of an onboard hydrogen production system from the thermal decomposition of ammonia. There are a few interesting points to mention about Figure 5.46.

- An ammonia compressor is used to deliver ammonia at the desired operating pressure to the reactor. This would be used in place of the preheater tank/RTE-140 combination illustrated in Figure 4.1.
- Exhaust gases from an ICE, SOFC, and/or gas turbine flow through a heat exchanger in order to provide heat to the membrane reactor. [29]
- A counter current nitrogen selective membrane is used in the raffinate stream to purify and recycle any unreacted ammonia. The exhaust gases from the engine, SOFC, and/or gas turbine are used as a sweep gas to minimize the size of the membrane in the raffinate stream [28].
- Nitrogen recombines with the exhaust gas stream and is expanded in a turbocharger increase the efficiency and power of the ICE [52]. However, a system using a SOFC or gas turbine would probably not use a turbocharger.
- A hydrogen compressor is used to compress produced hydrogen for storage in the two tanks illustrated in 5.46. Another benefit of the hydrogen compressor is the vacuum it draws on the shell side of the reactor to further increase trans – membrane pressure drop and extract more hydrogen.
- The pressure switches are used to control the flow of hydrogen to either the start - up tank to ensure there is enough hydrogen to achieve steady state hydrogen production or the operation tank for when steady state has been reached and excess hydrogen is being produced.

# Chapter 6: Conclusions and Recommendations

## 6.1 Conclusions

The production of hydrogen in a packed bed membrane reactor by the thermal decomposition of ammonia over a  $\text{Ni}_2\text{O}_3$  catalyst was investigated in this thesis work.

The increase in temperature from  $400.0^\circ\text{C}$  to  $500.0^\circ\text{C}$  was determined to increase the activity of the  $\text{Ni}_2\text{O}_3$  catalyst and the Gibb's free energy by a factor of 2.67. Due to these factors, ammonia decomposition was thermodynamically favoured at  $500.0^\circ\text{C}$  more so than at  $400.0^\circ\text{C}$ . This resulted in increased hydrogen production, ammonia conversion, energy/exergy ratio, and energy/exergy efficiency and ammonia decomposition rate.

The increase in operating pressure from 5.0 bar to 20.0 bar effectively increased the hydrogen partial pressure in the reactor and ergo; increased the hydrogen flux through the membrane. The residence time also increased with increased pressure due to the associated increase in ammonia density. These factors had resulted in increased hydrogen production, ammonia conversion, energy/exergy ratio, and energy/exergy efficiency and ammonia decomposition rate. Moreover, an inconsistency in the positive residence time vs. hydrogen production trend was observed with respect to the effect of residence time on hydrogen production rate for the case of 5.0 bar. This was determined to be due to the intermittent production rates observed at 5.0 bar. Hydrogen had to accumulate and be released in 5 minute intervals and the production rate was calculated from the amount of time it took to release the accumulated hydrogen. The hydrogen flux was much less due to a smaller trans – membrane pressure difference caused by an increased hydrogen pressure. The experiments are high pressure were consistent with the hypothesized effect of increasing residence time on hydrogen production rates due to continuous production.

- Hydrogen production ranged from a low of 1.25 mL/min at  $400.0^\circ\text{C}$ , 5.0 bar, and 0.937s to a high of 286.92 mL/min at  $500.0^\circ\text{C}$ , 20.0 bar, and 3.965 s. This lightly undershot the expected production of 300.0 mL/min. Steady hydrogen production took approximately 45.0 minutes to occur. This increase of hydrogen production with temperature was found to be in agreement with published literature and results.

- Energy and exergy ratios of the reaction ranged from a minimum of 0.022 and 0.0036 respectively at 400.0°C, 5.0 bar, and 0.937s to a maximum of 6.77 and 1.08 respectively at 500.0°C, 20.0 bar, and 3.965s. This was a direct consequence of the increased hydrogen production previously mentioned in the above point. This proves that high temperature and high pressure are required to integrate a system like this with an ICE successfully.
- The seemingly random fluctuations in energy and exergy ratio were caused by poor flow control being amplified by a constant.
- The maximum steady state energy and exergy efficiencies of the system were determined to be 16.9% and 20.3%, respectively. The exergy efficiency was determined to be higher due to the thermal exergy term containing an embedded Carnot number term and hydrogen being 97% exergy. This result favourably compares with the literature efficiency results.
- The maximum ammonia conversion was determined to be 95.6% at 500.0°C, 20.0 bar, and 3.965s. This is in good agreement with the literature results and illustrates the benefits of membrane reactors given in the literature.
- The minimum transient ammonia concentration in the raffinate stream was approximately 4.2%. This agrees well with the predicted behaviour in the study.
- Finally, a qualitative investigation into the effects of reacting ammonia high pressure and temperature over a loosely packed bed of Ni<sub>2</sub>O<sub>3</sub> catalyst powder was conducted by analyzing images from a SEM. A “smoothing” effect was observed when the Ni<sub>2</sub>O<sub>3</sub> powder was exposed to decomposing ammonia at the high temperatures and pressures investigated in this thesis work. The most probable for the explanation of this phenomenon was determined to be Ostwald ripening.
- A potential design for the integration of a membrane reactor system to produce hydrogen on demand for a hydrogen internal combustion was presented, explained and discussed.

It is important to note that electrical heating was suited only for the laboratory scale experimental setup and would not be practical in automotive applications. However, a properly designed turbo-generator could supply electricity for a furnace via the expansion of hot exhaust gases at high pressure. If a membrane reactor system as studied here could be heated by hot

exhaust gases, the application of a turbo-generator to generate electricity for heating could potentially reduce the magnitude of the problem associated with the uncontrollable nature of heat transfer via flowing hot combustion gases in a heat exchanger.

## **6.2 Recommendations**

During the course of this thesis work numerous problems were encountered with regards to flow control. During experiments, it had been observed that ammonia flow rate would change without any input/interference by the experimenter and the needle valve had to be constantly adjusted ever so slightly to try and steady the flow rate. This had resulted in relatively high uncertainties and unsteady behaviour during operation. A similar behaviour was noticed with the glass tube flow meters in the raffinate and hydrogen streams. Moreover, it was not possible to meter flows to less than 9.0 mL/min with the mass flow meter and needle valve combination. Some technical recommendations to remedy these problems are as follows:

- Remove the needle valve and flow meter combination and replace it with a mass flow controller. This would improve the controllability of the system and allow for the investigation of higher residence times. Also, it would decrease the fluctuations in ammonia flow rate that caused seemingly random fluctuations in hydrogen output, raffinate output, energy ratio and exergy ratio. Furthermore, for high pressure applications, a needle valve would not be the best choice due to potential damage to the valve's stem and tip.
- Install a back pressure regulator in the raffinate stream where the needle valve used to be. A back pressure regulator installed in the raffinate stream would allow for more consistent reactor pressure control.
- The glass tube flow meters should be removed and replaced with digital flow meters to increase accuracy.

## References

1. Agency, I. E. (2010). *Key World Energy Statistics*. Paris: International Energy Agency.
2. diMario, F., Iacobazzi, A., Infusino, R., & Mattuci, A. (2003). *Socioeconomic Aspects of the Hydrogen Economy Development*. EU Joint Research Centre.
3. Haseli, Y. (2008). *Analysis of Hydrodynamic Transport Phenomena in a Fluidized Bed for Thermochemical Hydrogen Production*. Oshawa: UOIT.
4. Dincer, I. (2002). Technical, Environmental and Exergetic Aspects of Hydrogen Energy Systems. *International Journal of Hydrogen Energy*, 265 - 285.
5. Zamfirescu, C., & Dincer, I. (2008). Using Ammonia as a Sustainable Fuel. *Journal of Power Sources*, 459 - 465.
6. Christensen, H., Johannessen, T., Sorensen, R., & Norskov, J. (2006). Towards an Ammonia Mediated Hydrogen Economy? *Catalysis Today*, 140 - 144.
7. Metkemeijer, R., & Achard, P. (1994). Comparison of Ammonia and Methanol Applied Indirectly in a Hydrogen Fuel Cell. *International Journal of Hydrogen Energy*, 535 - 542.
8. Rahimpour, M., & Asgari, A. (2009). Production of Hydrogen from Purge Gases of Ammonia Plants in a Catalytic Hydrogen Permselective Membrane Reactor. *International Journal of Hydrogen Energy*, 5795 - 5802.
9. Sorensen, R., Nielsen, L., Jensen, S., Hansen, O., Johannessen, T., Quadde, U., et al. (2005). Catalytic Ammonia Decomposition: Miniaturized Production of CO<sub>x</sub> Free Hydrogen for Fuel Cells. *Catalysis Communications*, 229 - 232.
10. Vitse, F., Cooper, M., & Botte, G. (2005). On the use of Ammonia Electrolysis for Hydrogen Production. *Journal of Power Sources*, 18 - 26.
11. Kumar, S., Shankar, S., Shah, P., & Kumar, S. (2006). A Comprehensive Model for Catalytic Membrane Reactors. *International Journal of Chemical Reactor Engineering*, 1 - 29.
12. Kraisuwansarn, N. (1991). *Simulation of a Membrane Reactor for Ammonia Decomposition*. Corvallis: Oregon State University.
13. Gear, C. (1971). The Automatic Integration of Ordinary Differential Equations. *Communications of the ACM*, 176 - 179.

14. Itoh, N., Xu, W., & Haraya, K. (1991). Basic Experimental Study on Palladium Membrane Reactors. *Journal of Membrane Science*, 149 - 155.
15. Buxbaum, R. (1997). Membrane Reactors, Fundamental and Commercial Advantages. E.G: For Methanol Reforming. *15th BCC Membrane Planning Conference*, (pp. 1-7). Newton.
16. Garcia, F., Hua-Ma, Y., Rodriguez-Ramos, I., & Guerrero-Ruiz, A. (2008). High Purity Hydrogen Production by a Low Temperature Catalytic Ammonia Decomposition in a Multifunctional Membrane Reactor. *Catalysis Communications*, 482 - 486.
17. Roy, S., Ray, N., Mukherjee, D., & Sen, S. (1975). *Kinetics and Mechanism of Ammonia Decomposition Over Alumina Supported Nickel Catalysts*. Sindri: The Fertilizer Corporation of India.
18. Tamaru, K. (1987). A "New" General Mechanism of Ammonia Synthesis and Decomposition on Transition Metals. *Accounts of Chemical Research*, 88 - 94.
19. Chellappa, A., Fischer, C., & Thomson, W. (2002). Ammonia Decomposition Kinetics over Ni-Pt/Al<sub>2</sub>O<sub>3</sub> for PEM Fuel Cell Applications. *Applied Catalysis*, 231 - 240.
20. Yin, S., Xu, B., Zhou, X., & Au, C. (2004). A Mini - Review on Ammonia Decomposition Catalysts for On - Site Generation of Hydrogen for Fuel Cell Applications. *Applied Catalysis*, 1 - 9.
21. Schlunder, E. (1968). Heat Transfer in Packed Beds. *Warme und Stoffubertragung Bd.*, 153 - 158.
22. Achenbach, E. (1995). Heat and Flow Characteristics of Packed Beds. *Experimental Thermal and Fluid Science*, 17 - 27.
23. Wen, D., & Ding, Y. (2006). Heat Transfer of Gas Flow Through a Packed Bed. *Chemical Engineering Science*, 3532 - 3542.
24. Gryaznov, V. (2000). Metal Containing Membranes for the Production of Ultrapure Hydrogen and the Recovery of Hydrogen Isotopes. *Separation and Purification Methods*, 171 - 187.
25. Ward, T., & Dao, T. (1999). Model of Hydrogen Permeation Behaviour in Palladium Membranes. *Journal of Membrane Science*, 211 - 231.
26. Morreale, B., Ciocco, M., Enick, R., Morsi, B., Howard, B., Cugini, A., et al. (2003). The Permeability of Hydrogen in Bulk Palladium at Elevated Temperatures and Pressures. *Journal of Membrane Science*, 87 - 97.

27. Al-Raisi, A., & Gardner, T. (2007). *Surface and Fluid Phase Transport Effects on Hydrogen Permeability Through Palladium Based Membranes*. Golden: American Institute of Chemical Engineers.
28. Kluiters, S. (2004). *Status Review on Membrane Systems for Hydrogen Separation*. The Netherlands: E.U.
29. Kim, J., & Kwon, O. (2010). A Micro - Reforming System Integrated with a Heat Recirculating Micro - Combustor to Produce Hydrogen from Ammonia. *International Journal of Hydrogen Energy*, 1 - 10.
30. Kordesch, K., Hacker, V., Fankhauser, R., Faleschnin, & G. (2005). *Patent No. US 6,936,363 B2*. United States.
31. Chorkendorff, I., & Niemantsverdriet, J. (2003). *Concepts of Modern Catalysis and Kinetics*. Weinheim: Wiley.
32. Hellgardt, C., Richardson, D., Russell, P., Mason, G., B.A., B., & Cumming, I. (2007). *Modelling of Tubular Ammonia Decomposition Reactors for Fuel Cell Applications*. London: Imperial College of Science.
33. Spivey, J., & Dooley, K. (2010). *Catalysis*. London: RSC Publishing.
34. Levent, M., Budak, G., & Karabulut, A. (1998). Estimation of Concentration and Temperature Profiles for Methane - Steam Reforming Reaction in a Porous Catalyst. *Fuel Processing Technology*, 251 - 263.
35. Zgierski, M., & Smedarchina, Z. (2003). Auto - Catalytic Effect in Ammonia Disassociation on a Si(100) Surface. A First Principles Model Study. *Europhysics Letters*, 556 - 561.
36. Cullen, M., & Zill, D. (2005). *Differential Equations with Boundary Value Problems*. New York: Wiley.
37. NESLAB, T. . (2000, November 17th). RTE - 140 Refrigerated Bath/Circulator with Analog/Digital Controller. *Instruction and Operation Manual*. Thermo - NESLAB.
38. Cengel, Y. (2006). *Heat and Mass Transfer: A Practical Approach*. New York: McGraw - Hill.
39. Montgomery, D. (2005). *Design and Analysis of Experiments*. Hoboken: Wiley and Sons.
40. Buxbaum, R. (n.d.). *R.E.B Research and Consulting*. Retrieved June 15, 2011, from [http://www.rebresearch.com/membrane\\_reactors.html](http://www.rebresearch.com/membrane_reactors.html)

41. Skodras, G., Kaldis, S., Topis, S., Koutsonikolas, D., Grammelis, P., Sakellaropolous, G. (2006). NH<sub>3</sub> Decomposition and Simultaneous H<sub>2</sub> Separation with a Commercial Pd-Cu-Ag/V Membrane. *Proceedings of the IGEC-2*. IGEC2-141. 1 – 7.
42. Israni, S.I., Nair, B.K.R., Harold, M.P. (2009) Hydrogen Generation and Purification in a Composite Pd Hollow Fiber Membrane Reactor: Experiments and Modeling. *Catalysis Today*, 299 – 311.
43. Rivero, R., Garfias, M. (2006). Standard Chemical Exergy of Elements Updated. *International Journal of Energy*, 3310 – 3326.
44. Chein, R., Chen, Y., Chang, C., & Chung, J. (2010). Numerical Modeling of Hydrogen Production From Ammonia Decomposition for Fuel Cell Applications. *International Journal of Hydrogen Energy*, 589 – 597.
45. Maloney, J. (2008). *Perry's Chemical Engineers Handbook (8th Edition)*. New York: McGraw - Hill.
46. Brown, W. (n.d.). *Doc Brown's Chemistry: Advanced Level Inorganic Chemistry*. Retrieved July 2011, 2011, from <http://www.docbrown.info/page07/transition08Ni.htm>
47. IUPAC. (n.d.). *IUPAC Gold Book*. Retrieved July 11, 2011, from <http://goldbook.iupac.org/O04348.html>
48. Holman, J.P. (2000). *Experimental Methods for Engineers*. New York: McGraw-Hill.
49. El- Wakil, M. (1984). *Powerplant Technology*. New York: McGraw - Hill.
50. Nieminen, J., D'Souza, N., & Dincer, I. (2009). Comparative Combustion Characteristics of Gasoline and Hydrogen Fuelled ICEs. *International Journal of Hydrogen Energy*, 1-10.
51. Nieminen, J., & Dincer, I. (2009). Comparative Exergy Analyses of Gasoline and Hydrogen Fuelled ICEs. *International Journal of Hydrogen Energy*, 1-9.
52. Heywood, J. (1988). *Internal Combustion Engine Fundamentals*. New York: McGraw - Hill.

## **Appendices**

# Appendix A

## Ammonia Decomposition Reaction in EES:

"Dead State Pressure"

$$P_o = 1.0$$

"Temperature Input (Tr = [673,773] K)"

$$T_r = 673$$

"Pressure Input: P = [1,20] bar"

$$P_r = 20.0$$

"Enthalpy of reaction"

$$dH = 0.5 \cdot \text{enthalpy}(N_2, T = T_r) + 1.5 \cdot \text{enthalpy}(H_2, T = T_r) - \text{enthalpy}(NH_3, T = T_r)$$

"Entropy of reaction relative to dead state at P0"

$$dS = (0.5 \cdot \text{entropy}(N_2, T = T_r, P = P_o) + 1.5 \cdot \text{entropy}(H_2, T = T_r, P = P_o)) - \text{entropy}(NH_3, T = T_r, P = P_o)$$

"Entropy of reaction at temperature and pressure"

$$dS_r = (0.5 \cdot \text{entropy}(N_2, T = T_r, P = P_r) + 1.5 \cdot \text{entropy}(H_2, T = T_r, P = P_r)) - \text{entropy}(NH_3, T = T_r, P = P_r)$$

"Equilibrium expression"

$$dG = dH - T_r \cdot dS + R \cdot T_r \cdot \ln(K_{eq} \cdot P_r / P_o)$$

"Equilibrium Condition"

$$dG = -R \cdot T_r \cdot \ln(K_{eq})$$

$$K_{eq} \cdot C_{NH_3} = C_{N_2}^{0.5} \cdot C_{H_2}^{1.5}$$

"Hydrogen Draw: x = [0,1]%"

$$x = 0.92$$

"Total Number of Moles"

$$N_t = 1.5 \cdot x + n - 0.5$$

"Concentration Terms"

$$C_{N_2} = 0.5 / N_t$$

$$C_{H_2} = 1.5 \cdot x / N_t$$

$$C_{NH_3} = (n - 1) / N_t$$

"Sum of all Partial Pressures: Must Equal 1.0 (criteria for true)"

$$E = C_{N2} + C_{NH3} + C_{H2}$$

"Transmembrane Pressure"

$$P_{trans} = (1-x)P_{H2} - 1.0$$

"KINETICS SECTION"

"Partial Pressure Terms"

$$P_{NH3} = C_{NH3}Pr$$

$$P_{N2} = C_{N2}Pr$$

$$P_{H2} = C_{H2}Pr$$

"Sum of all Partial Pressures: Must Equal Pr (criteria for true)"

$$F = P_{NH3} + P_{N2} + P_{H2}$$

"Arrhenius Expression"

"Activation Energy"

$$E_a = 196e3 \text{ [kJ/kmol]}$$

"Pre-exponential factor"

$$k_o = 2.098e6$$

$$A = \exp(-(E_a/TrR\#)) + k_o$$

"Rate equation"

$$r = A*((P_{NH3}/(1-x)P_{H2}^{1.5}) - (P_{N2}^{0.5}/K_{eq})*((1-x)(P_{H2}^{1.5})/(P_{NH3})))$$

## Methanol Reforming Reaction in EES

"Reaction Pressure"

$$P_r = 20.0$$

"Dead State Pressure"

$$P_o = 1.0$$

"Dimensionless Pressure Ratio"

$$p = P_r/P_o$$

"Reaction Temp: limited by EES saying that properties of methanol are only valid up to 570K"

$$T_r = 569$$

"Enthalpy of reaction: CH<sub>3</sub>OH + H<sub>2</sub>O -> CO<sub>2</sub> + 3H<sub>2</sub> "

$$dH = (\text{enthalpy}(\text{CO}_2, T = T_r) + 3 * \text{enthalpy}(\text{H}_2, T = T_r)) - \text{enthalpy}(\text{CH}_3\text{OH}, T = T_r) - \text{enthalpy}(\text{H}_2\text{O}, T = T_r)$$

"Entropy of reaction at dead state: CH<sub>3</sub>OH + H<sub>2</sub>O -> CO<sub>2</sub> + 3H<sub>2</sub>"

$$dS_o = (\text{entropy}(\text{CO}_2, T = T_r, P = P_o) + 3 * \text{entropy}(\text{H}_2, T = T_r, P = P_o)) - (\text{entropy}(\text{CH}_3\text{OH}, T = T_r, P = P_o) + \text{entropy}(\text{H}_2\text{O}, T = T_r, P = P_o))$$

"Entropy of reaction at working temperatures and pressures"

$$dS_r = (\text{entropy}(\text{CO}_2, T = T_r, P = P_r) + 3 * \text{entropy}(\text{H}_2, T = T_r, P = P_r)) - (\text{entropy}(\text{CH}_3\text{OH}, T = T_r, P = P_r) + \text{entropy}(\text{H}_2\text{O}, T = T_r, P = P_r))$$

$$K = k_{eq} * p^2$$

"Pressures"

"Shell Pressure Expression"

$$P_{shell} = 1.0$$

"Transmembrane Pressure"

$$P_{trans} = (1 - x) * P_{H2} - P_{shell}$$

"Concentration Terms"

"Total number of moles"

$$N_t = 2 * n - 1 + 3 * x$$

$$C_{CO2} = 1/N_t$$

$$C_{CH3OH} = (n - 1)/N_t$$

$$C_{H2} = 3 * x / N_t$$

$$C_{H_2O} = (n - 1)/N_t$$

"Partial Pressures"

$$P_{CH_3OH} = C_{CH_3OH} * P_r$$

$$P_{CO_2} = C_{CO_2} * P_r$$

$$P_{H_2O} = C_{H_2O} * P_r$$

$$P_{H_2} = C_{H_2} * P_r$$

"Equilibrium expression"

$$dG = dH - T_r * dS_o + R * T_r * \ln(K)$$

"Equilibrium Condition"

$$dG = -R * T_r * \ln(k_{eq})$$

"Expression for Equilibrium Constants"

$$k_{eq} * (C_{CH_3OH}) * (C_{H_2O}) = (C_{CO_2}) * ((C_{H_2})^3)$$

"Equilibrium Constants"

"Hydrogen draw"

$$x = z$$

"Partial Pressure and Concentration Conservation: must equal  $P_r = 20\text{bar}$  and  $1.0$  for true"

$$E = C_{CO_2} + C_{CH_3OH} + C_{H_2} + C_{H_2O}$$

$$F = P_{CO_2} + P_{CH_3OH} + P_{H_2} + P_{H_2O}$$

"Chemical Rate Equation"

"Activation energy"

$$E_a = 115e3$$

"Pre - exponential factor"

$$k_o = 6.0e8 \text{ [mol/min} * \text{g}_{cat}]$$

"Arrhenius Expression"

$$A = \exp(-E_a / T_r * R) + k_o$$

"rate equation"

$$r = A * (((P_{CH_3OH} * P_{H_2O}) / ((1 - x) * (P_{H_2})^3)) - (P_{CO_2} / (P_{H_2O} * k_{eq})) * (((1 - x) * (P_{H_2})^3)) / (P_{CH_3OH}))$$

## Steam Methane Reforming Reaction in EES

"Reaction Pressure"

$$P_r = 20$$

"Dead State Pressure"

$$P_o = 1.0$$

"Dimensionless Pressure Ratio"

$$p = P_r/P_o$$

"Reaction Temp"

$$T_r = 1173$$

"Enthalpy of reaction: CH<sub>4</sub> + 2H<sub>2</sub>O -> CO<sub>2</sub> + 4H<sub>2</sub> "

$$dH = (\text{enthalpy}(\text{CO}_2, T = T_r) + 4 * \text{enthalpy}(\text{H}_2, T = T_r)) - (\text{enthalpy}(\text{CH}_4, T = T_r) + 2 * \text{enthalpy}(\text{H}_2\text{O}, T = T_r))$$

"Entropy of reaction at dead state: CH<sub>4</sub> + 2H<sub>2</sub>O -> CO<sub>2</sub> + 4H<sub>2</sub>"

$$dS_o = (\text{entropy}(\text{CO}_2, T = T_r, P = P_o) + 4 * \text{entropy}(\text{H}_2, T = T_r, P = P_o)) - (\text{entropy}(\text{CH}_4, T = T_r, P = P_o) + 2 * \text{entropy}(\text{H}_2\text{O}, T = T_r, P = P_o))$$

"Entropy of reaction at working temperatures and pressures"

$$dS_r = (\text{entropy}(\text{CO}_2, T = T_r, P = P_r) + 4 * \text{entropy}(\text{H}_2, T = T_r, P = P_r)) - (\text{entropy}(\text{CH}_4, T = T_r, P = P_r) + 2 * \text{entropy}(\text{H}_2\text{O}, T = T_r, P = P_r))$$

$$K = \exp((dS_r - dS_o)/R\#)$$

"Concentration Terms"

"Total number of moles"

$$N_t = 3 * n - 2 + 4 * x$$

$$C_{\text{CO}_2} = 1/N_t$$

$$C_{\text{CH}_4} = (n - 1)/N_t$$

$$C_{\text{H}_2} = (4 * x)/N_t$$

$$C_{\text{H}_2\text{O}} = (2 * n - 2)/N_t$$

"Partial Pressure Terms"

$$P_{\text{H}_2} = C_{\text{H}_2} * P_r$$

$$P_{\text{CO}_2} = C_{\text{CO}_2} * P_r$$

$$P_{\text{CH}_4} = C_{\text{CH}_4} * P_r$$

$$P_{\text{H}_2\text{O}} = C_{\text{H}_2\text{O}} * P_r$$

### "Pressure Drops"

$$P_{\text{shell}} = 1.0$$

$$P_{\text{tube}} = (1 - x) \cdot P_{\text{H}_2}$$

$$P_{\text{trans}} = P_{\text{tube}} - P_{\text{shell}}$$

### "Equilibrium Constants"

$$k_{\text{eq}} \cdot (C_{\text{CH}_4}) \cdot (C_{\text{H}_2\text{O}})^2 = ((C_{\text{CO}_2}) \cdot (C_{\text{H}_2})^4)$$

### "Gibbs Free Energy"

#### "Equilibrium expression"

$$dG = dH - T_r \cdot dS_o + R \cdot T_r \cdot \ln(k_{\text{eq}} \cdot p^2)$$

#### "Equilibrium Condition"

$$dG = -R \cdot T_r \cdot \ln(k_{\text{eq}})$$

#### "Hydrogen draw"

$$x = 0.901$$

$$E = C_{\text{CO}_2} + C_{\text{CH}_4} + C_{\text{H}_2} + C_{\text{H}_2\text{O}}$$

$$F = P_{\text{CO}_2} + P_{\text{CH}_4} + P_{\text{H}_2} + P_{\text{H}_2\text{O}}$$

#### "Reaction Rate Equation"

#### "Arrhenius Expression"

#### "Activation Energy"

$$E_a = 240 \text{ [kJ/kmol]}$$

#### "Pre-exponential factor"

$$k_o = 4.22e15/3600$$

$$A = \exp(-E_a/T_r \cdot R) + k_o$$

#### "Rate equation"

$$r = A \cdot ((P_{\text{CH}_4} \cdot (P_{\text{H}_2\text{O}})^2) / ((1-x) \cdot P_{\text{H}_2})^4 - (1/k_{\text{eq}}) \cdot (((1-x) \cdot (P_{\text{H}_2})^4) \cdot P_{\text{CO}_2} / (P_{\text{CH}_4}) \cdot (P_{\text{H}_2\text{O}})^2)))$$

## Appendix B

Table B1: 5.0 bar, 400°C, 44 mL/min.

Time (min)	44 ml/min	H <sub>2</sub> Production (mL/min)	H <sub>2</sub> Pressure (bar)	Raf Pressure (bar)	Raf Flow (mL/min)	NH <sub>3</sub> Flow (mL/min)
0	(STOICH)	0	0	0.1	17.1	0
5	(intermittent)	0.145	0	0.1	40.8	40
10		0.290	0.05	0.1	37.8	44.9
15		0.435	0.1	0.1	29.2	44.61
20		0.580	0.1	0.1	26.6	42.84
25		0.725	0.12	0.1	24	45.9
30		0.869	0.15	0.1	24	44.61
35		1.014	0.15	0.1	24	45.62
40		1.047	0.2	0.1	24	48.52
45		1.079	0.2	0.1	24	44.612
50		1.112	0.2	0.1	24	44.23
55		1.144	0.21	0.1	24	48.22
60		1.177	0.21	0.1	24	46.41
65		1.209	0.15	0.1	21.6	45.18
70		1.242	0.21	0.1	21.6	52.3
75		1.242	0.22	0.1	21.6	44.42
80		1.243	0.22	0.1	21.6	44.96
85		1.244	0.25	0.1	21.6	48.5
90		1.245	0.25	0.1	21.6	49.05
95		1.246	0.22	0.1	21.6	47.58
100		1.246	0.22	0.1	21.6	45.78
105		1.247	0.22	0.1	21.6	44.79
110		1.248	0.21	0.1	19.3	43.48
115		1.249	0.21	0.1	19.3	44.3
120		1.250	0.21	0.1	19.3	45.35

Table B2: 5.0 bar, 400°C, 24 mL/min.

Time (min)	24 ml/min	H <sub>2</sub> Production (mL/min)	H <sub>2</sub> Pressure (bar)	Raf Pressure (bar)	Raf Flow (mL/min)	NH <sub>3</sub> Flow (mL/min)
0	(LEAN)	0	0	0	0	0
5	(intermittent)	0.165	0	1.1	4.77	25.34
10		0.330	0.08	1.1	5.71	24.68
15		0.490	0.1	1.1	7	24.96
20		0.860	0.15	1.1	6.96	23.01
25		1.100	0.18	1.1	8.2	24.93
30		1.300	0.21	1.1	8.2	24.174
35		1.400	0.21	1.1	8.2	24.61
40		1.470	0.25	1.1	8.2	23.03
45		1.540	0.25	1.1	11.3	24.36
50		1.610	0.25	1.1	13.2	23.57
55		1.680	0.25	1.1	15	23.25
60		1.750	0.25	1.1	15	24.3
65		1.920	0.29	1.1	15	22.15
70		2.000	0.29	1.1	13.2	23.79
75		2.100	0.30	1.1	15	24.49
80		2.167	0.30	1.1	17.1	23.57
85		2.233	0.30	1.1	17.1	22.52
90		2.240	0.32	1.1	15	25.03
95		2.283	0.35	1.1	17.1	22.71
100		2.325	0.35	1.1	15	30.28
105		2.368	0.40	1.1	17.1	23.85
110		2.388	0.40	1.1	17.1	26.51
115		2.409	0.40	1.1	17.1	25.1
120		2.430	0.44	1.1	15	23.9

Table B3: 5.0 bar, 400°C, 12 mL/min.

Time (min)	12 ml/min	H <sub>2</sub> Production (mL/min)	H <sub>2</sub> Pressure (bar)	Raf Pressure (bar)	Raf Flow (mL/min)	NH <sub>3</sub> Flow (mL/min)
0	(VERY LEAN)	0	0	0	0	0
5	(intermittent)	0.120	0	1.075	2.385	14.366
10		0.241	0.05	1.05	2.855	13.164
15		0.358	0.05	1.05	3.5	14.809
20		0.628	0.11	1.05	3.48	14.018
25		0.803	0.13	1.05	4.1	13.733
30		0.949	0.15	1.05	4.1	11.613
35		1.022	0.15	1.05	4.1	13.258
40		1.073	0.18	1.05	4.1	14.366
45		1.124	0.18	1.05	5.65	13.164
50		1.175	0.18	1.05	6.6	14.809
55		1.226	0.18	1.05	7.5	14.018
60		1.278	0.18	1.05	7.5	13.733
65		1.402	0.21	1.05	7.5	11.613
70		1.460	0.21	1.05	6.6	13.258
75		1.533	0.21	1.05	7.5	12.436
80		1.582	0.21	1.05	8.55	12.657
85		1.630	0.21	1.05	8.55	12.025
90		1.635	0.23	1.05	7.5	11.710
95		1.666	0.25	1.05	8.55	14.049
100		1.697	0.25	1.05	7.5	13.132
105		1.728	0.28	1.05	8.55	12.183
110		1.743	0.28	1.05	8.55	13.735
115		1.759	0.28	1.05	8.55	11.550
120		1.774	0.31	1.05	7.5	11.044

Table B4: 5.0 bar, 500°C, 44 mL/min.

Time (min)	44 ml/min	H <sub>2</sub> Production (mL/min)	H <sub>2</sub> Pressure (bar)	Raf Pressure (bar)	Raf Flow (mL/min)	NH <sub>3</sub> Flow (mL/min)
0	(STOICH)	0	0	0	0	0
5	(intermittent)	2.64	0.05	0.1	26.95	48.6
10		3.3	1.4	0.1	26.95	53
15		4.05	1.55	0.1	13.755	49.36
20		4.11	.575	0.1	13.755	47.9
25		4.385	0.75	0.1	26.95	48.66
30		4.44	0.95	0.1	26.95	48.7
35		8.51	1.05	0.1	26.95	48.14
40		8.6	1.2	0.1	26.95	45.5
45		9.05	1.05	0.1	26.95	53.54
50		11.67	1.05	0.1	26.95	45.66
55		12.445	1.1	0.1	19.775	46.6
60		12.445	1.075	0.1	23.1	45.62
65		13.47	1.2	0.1	23.1	45.62
70		16.185	1.15	0.1	19.775	48.16
75		16.4	1.3	0.1	19.775	45.6
80		16.4	1.4	0.1	17.08	47.96
85		16.1	1.25	0.1	23.1	44.28
90		16.1	1.4	0.1	17.08	49.42
95		16.1	1.4	0.1	17.08	47
100		17.195	1.4	0.1	17.08	47.02
105		16.4	1.45	0.1	17.08	44.34
110		16.5	1.5	0.1	17.08	44.6
115		16.4	1.5	0.1	17.08	48.22
120		16.5	1.5	0.1	17.08	47.02

Table B5: 5.0 bar, 500°C, 24 mL/min.

Time (min)	24 ml/min	H <sub>2</sub> Production (mL/min)	H <sub>2</sub> Pressure (bar)	Raf Pressure (bar)	Raf Flow (mL/min)	NH <sub>3</sub> Flow (mL/min)
0	(LEAN)	0	0	0	0	0
5	(intermittent)	5.28	0.5	0.1	15.4	24.3
10		6.6	0.8	0.1	15.4	26.5
15		8.1	1.1	0.1	7.86	24.68
20		8.22	1.0	0.1	7.86	23.95
25		8.77	1.5	0.1	15.4	24.33
30		8.88	1.9	0.1	15.4	24.35
35		17.02	2.1	0.1	15.4	24.07
40		17.2	2.4	0.1	15.4	22.75
45		18.1	2.1	0.1	15.4	26.77
50		23.34	2.1	0.1	15.4	22.83
55		24.89	2.2	0.1	11.3	23.3
60		24.89	2.15	0.1	13.2	22.81
65		26.94	2.4	0.1	13.2	22.81
70		32.37	2.3	0.1	11.3	24.08
75		32.8	2.6	0.1	11.3	22.8
80		32.8	2.8	0.1	9.76	23.98
85		32.2	2.5	0.1	13.2	22.14
90		32.2	2.8	0.1	9.76	24.71
95		32.2	2.8	0.1	9.76	23.5
100		34.39	2.8	0.1	9.76	23.51
105		32.8	2.9	0.1	9.76	22.17
110		33	3	0.1	9.76	22.3
115		32.8	3	0.1	9.76	24.11
120		33	3	0.1	9.76	23.51

Table B6: 5.0 bar, 500°C, 12 mL/min.

Time (min)	12 ml/min	H <sub>2</sub> Production (mL/min)	H <sub>2</sub> Pressure (bar)	Raf Pressure (bar)	Raf Flow (mL/min)	NH <sub>3</sub> Flow (mL/min)
0	(VERY LEAN)	0	0	0	0	0
5	(intermittent)	5.74	1	0.09	8.2	14.366
10		7.92	1.1	0.09	4.77	13.164
15		11.32	1	0.09	5.71	14.809
20		16.9	2	0.09	5.71	14.018
25		17.95	2.2	0.09	4.77	13.733
30		21.13	1.1	0.09	4.77	11.613
35		22.23	2.2	0.09	4.77	13.258
40		22.98	2.15	0.09	4.77	14.366
45		22.27	2.2	0.09	4.77	13.164
50		22.3	2.4	0.09	5.71	14.809
55		23.11	2.45	0.09	5.71	14.018
60		24.29	2.5	0.09	5.24	13.733
65		24.3	2.5	0.09	5.24	11.613
70		24.5	2.5	0.09	5.24	13.258
75		24.41	2.5	0.09	5.24	12.436
80		24.31	2.5	0.09	5.24	12.657
85		24.3	2.5	0.09	5.24	12.025
90		24.29	2.5	0.09	5.24	11.710
95		24.5	2.5	0.09	5.24	14.049
100		24.46	2.5	0.09	5.24	13.132
105		24.5	2.5	0.09	5.24	12.183
110		24.39	2.5	0.09	5.24	13.735
115		24.51	2.5	0.09	5.24	11.550
120		24.46	2.5	0.09	5.24	11.044

Table B7: 10.0 bar, 400°C, 10.12 mL/min.

Time (min)	10.12 ml/min	H <sub>2</sub> Production (mL/min)	H <sub>2</sub> Pressure (bar)	Raf Pressure (bar)	Raf Flow (mL/min)	NH <sub>3</sub> Flow (mL/min)
0	(LEAN)	0	0	0.15	0	0
5	(intermittent)	10.564	1.1	0.15	68.1	11.019
10		27.19	1.15	0.15	64.4	10.791
15		29.71	1.15	0.15	53.8	10.900
20		31.04	1.2	0.15	79.8	10.821
25		31.69	1.25	0.15	79.8	11.831
30		32.36	1.25	0.15	79.8	10.009
35		35.08	1.3	0.15	79.8	9.930
40		37.99	1.3	0.15	79.8	10.989
45		38.974	1.35	0.15	79.8	9.860
50		38.974	1.35	0.15	79.8	10.346
55		38.974	1.35	0.15	79.8	10.801
60		38.974	1.35	0.15	79.8	10.009
65		38.974	1.35	0.15	79.8	9.999
70		39.011	1.4	0.15	79.8	10.801
75		39.011	1.4	0.15	79.8	10.019
80		39.011	1.4	0.15	79.8	10.880
85		39.011	1.4	0.15	79.8	9.870
90		39.864	1.4	0.15	75.8	10.019
95		39.864	1.4	0.15	75.8	9.910
100		39.864	1.4	0.15	75.8	10.989
105		39.864	1.4	0.15	75.8	11.088
110		39.864	1.4	0.15	75.8	9.999
115		39.864	1.4	0.15	75.8	9.821
120		39.864	1.4	0.15	75.8	9.950

Table B8: 10.0 bar, 400°C, 20.24 mL/min.

Time (min)	20.24 ml/min	H <sub>2</sub> Production (mL/min)	H <sub>2</sub> Pressure (bar)	Raf Pressure (bar)	Raf Flow (mL/min)	NH <sub>3</sub> Flow (mL/min)
0	(STOICH)	0	0	0.1	0	0
5	(intermittent)	7.638	0.5	0.1	49.236	22.368
10		19.658	0.8	0.1	46.561	21.906
15		21.480	0.8	0.1	38.897	22.127
20		22.442	0.8	0.1	57.695	21.966
25		22.912	1.25	0.1	57.695	24.016
30		23.396	1.25	0.1	57.695	20.318
35		25.363	1.3	0.1	57.695	20.157
40		25.679	1.3	0.1	57.695	22.308
45		27.561	1.35	0.1	57.695	20.017
50		27.561	1.35	0.1	57.695	21.001
55		27.561	1.35	0.1	57.695	21.926
60		28.178	1.35	0.1	57.695	20.318
65		28.178	1.35	0.1	57.695	20.298
70		28.205	1.4	0.1	57.695	21.926
75		28.205	1.4	0.1	57.695	20.338
80		28.205	1.4	0.1	57.695	22.087
85		28.205	1.4	0.1	57.695	20.037
90		28.822	1.4	0.1	54.803	20.338
95		28.822	1.4	0.1	54.803	20.117
100		28.822	1.3	0.1	54.803	22.308
105		28.822	1.3	0.1	54.803	22.509
110		28.822	1.3	0.1	54.803	20.298
115		28.822	1.3	0.1	54.803	19.936
120		28.822	1.3	0.1	54.803	20.197

Table B9: 10.0 bar, 500°C, 20.24 mL/min.

Time (min)	20.24 ml/min	H <sub>2</sub> Production (mL/min)	H <sub>2</sub> Pressure (bar)	Raf Pressure (bar)	Raf Flow (mL/min)	NH <sub>3</sub> Flow (mL/min)
0	(STOICH)	0	0	0.11	0	0
5	(sustained)	71.722	1.3	0.11		23.317
10		79.530	0.1	0.11		22.836
15		79.530	0.1	0.11		23.066
20		87.873	0.1	0.11		22.898
25		87.873	0.1	0.11		25.035
30		96.210	0.1	0.11		21.180
35		96.210	0.1	0.11		21.013
40		96.210	0.1	0.11		23.255
45		97.910	0.1	0.11		20.866
50		98.200	0.1	0.11		21.893
55		98.700	0.1	0.13		22.856
60		100.320	0.1	0.11		21.180
65		102.150	0.1	0.11		21.160
70		103.300	0.1	0.12		22.856
75		104.710	0.1	0.12		21.201
80		105.392	0.1	0.11		23.024
85		105.392	0.1	0.11		20.887
90		105.392	0.1	0.11		21.201
95		105.392	0.1	0.12		20.971
100		105.392	0.1	0.12		23.255
105		105.392	0.1	0.11		23.464
110		105.392	0.1	0.12		21.160
115		105.392	0.1	0.12		20.782
120		105.220	0.15	0.12		21.055

\*Raf Flow was obstructed by small amounts blue ammonia- nickel liquid formation. No reliable Raf Data collected.

Table B10: 10.0 bar, 500°C, 10.12 mL/min.

Time (min)	10.12 ml/min	H <sub>2</sub> Production (mL/min)	H <sub>2</sub> Pressure (bar)	Raf Pressure (bar)	Raf Flow (mL/min)	NH <sub>3</sub> Flow (mL/min)
0	(LEAN)	0	0.75	0.1	0	0
5	(sustained)	99.2	0.3	0.1	64.4	11.13
10		110	0.3	0.1	60.8	10.9
15		110	0.3	0.1	60.8	11.01
20		121.54	0.3	0.1	53.8	10.93
25		121.54	0.3	0.1	53.8	11.95
30		133.07	0.3	0.1	53.8	10.11
35		133.07	0.3	0.1	53.8	10.03
40		133.07	0.3	0.1	53.8	11.1
45		145.77	0.3	0.1	53.8	9.96
50		145.77	0.3	0.1	53.8	10.45
55		145.77	0.3	0.1	53.8	10.91
60		145.77	0.3	0.1	53.8	10.11
65		145.77	0.3	0.1	53.8	10.1
70		145.77	0.3	0.1	53.8	10.91
75		145.77	0.3	0.1	53.8	10.12
80		145.77	0.3	0.1	53.8	10.99
85		145.77	0.3	0.1	53.8	9.97
90		145.77	0.3	0.1	53.8	10.12
95		145.77	0.3	0.1	53.8	10.01
100		145.77	0.3	0.1	53.8	11.1
105		145.77	0.3	0.1	53.8	11.2
110		145.77	0.3	0.1	53.8	10.1
115		145.77	0.3	0.1	53.8	9.92
120		145.77	0.3	0.1	53.8	10.05

Table B11: 20.0 bar, 400°C, 9.0 mL/min.

Time (min)	9.0 ml/min	H <sub>2</sub> Production (mL/min)	H <sub>2</sub> Pressure (bar)	Raf Pressure (bar)	Raf Flow (mL/min)	NH <sub>3</sub> Flow (mL/min)
0	(STOICH)	0	0	0	0	0
5	(intermittent)	26.603	1.3	1.1		10.080
10		32.584	1.4	1.1		9.082
15		32.584	1.4	1.1		9.651
20		35.677	1.4	1.1		9.102
25		39.080	1.5	1.1		7.994
30		42.483	1.6	1.1		8.214
35		50.010	1.9	1.1		9.152
40		58.259	2.0	1.05		10.160
45		65.910	2.2	1.05		8.992
50		72.920	2.25	1.05		9.631
55		76.923	0.2	1.05		8.074
60		76.923	0.2	1.05		9.860
65		76.923	0.2	1.05		9.032
70		76.923	0.2	1.1		9.641
75		76.923	0.2	1.1		8.982
80		76.923	0.15	1.1		9.082
85		76.923	0.15	1.1		8.643
90		76.923	0.15	1.1		8.792
95		76.923	0.15	1.1		9.162
100		76.923	0.2	1.1		9.192
105		76.923	0.2	1.1		8.952
110		76.923	0.2	1.1		10.090
115		76.923	0.2	1.1		8.064
120		76.923	0.2	1.1		9.122

\*Raf Flow was obstructed by small amounts blue ammonia- nickel liquid formation. No reliable Raf Data collected.

Table B12: 20.0 bar, 400°C, 18 mL/min.

Time (min)	18 ml/min	H <sub>2</sub> Production (mL/min)	H <sub>2</sub> Pressure (bar)	Raf Pressure (bar)	Raf Flow (mL/min)	NH <sub>3</sub> Flow (mL/min)
0	(RICH)	0	0.75	0.1	0	0
5	(sustained)	15.780	1.1	1.1		19.828
10		20.012	1.15	1.1		17.865
15		23.526	1.15	1.1		18.984
20		25.759	1.2	1.1		17.904
25		28.216	1.2	1.1		15.725
30		30.673	1.2	1.1		16.157
35		36.107	1.2	1.1		18.002
40		42.063	1.5	1.05		19.985
45		48.540	1.7	1.05		17.688
50		48.540	1.7	1.05		18.945
55		49.899	1.8	1.05		15.882
60		52.268	1.9	1.05		19.396
65		55.538	1.9	1.05		17.767
70		55.538	1.9	1.1		18.964
75		55.538	1.9	1.1		17.669
80		55.538	1.9	1.1		17.865
85		55.538	1.9	1.1		17.001
90		55.538	1.0	1.1		17.296
95		55.538	1.0	1.1		18.022
100		55.538	1.0	1.1		18.081
105		55.538	1.0	1.1		17.610
110		55.538	1.1	1.1		19.848
115		55.538	1.1	1.1		15.862
120		55.538	1.0	1.1		17.943

\*Raf Flow was obstructed by small amounts blue ammonia- nickel liquid formation. No reliable Raf Data collected.

Table B13: 20.0 bar, 500°C, 9.0 mL/min.

Time (min)	9.0 ml/min	H <sub>2</sub> Production (mL/min)	H <sub>2</sub> Pressure (bar)	Raf Pressure (bar)	Raf Flow (mL/min)	NH <sub>3</sub> Flow (mL/min)
0	(STOICH)	0	0	0	0	0
5	(sustained)	99.231	0.2	1.05		10.1
10		121.538	0.15	1.05		9.1
15		121.538	0.15	1.05		9.67
20		133.077	0.2	1.05		9.12
25		145.769	0.1	1.05		8.01
30		158.462	0.1	1.05		8.23
35		186.538	0.1	1.05		9.17
40		217.308	0.1	1.05		10.18
45		250.769	0.1	1.05		9.01
50		286.923	0.1	1.05		9.65
55		286.923	0.1	1.05		8.09
60		286.923	0.1	1.05		9.88
65		286.923	0.1	1.05		9.05
70		286.923	0.1	1.05		9.66
75		286.923	0.1	1.05		9
80		286.923	0.1	1.05		9.1
85		286.923	0.1	1.05		8.66
90		286.923	0.1	1.05		8.81
95		286.923	0.1	1.05		9.18
100		286.923	0.1	1.05		9.21
105		286.923	0.1	1.05		8.97
110		286.923	0.1	1.05		10.11
115		286.923	0.1	1.05		8.08
120		286.923	0.1	1.05		9.14

\*Raf Flow was obstructed by small amounts blue ammonia- nickel liquid formation. No reliable Raf Data collected.

Table B14: 20.0 bar, 500°C, 18.0 mL/min.

Time (min)	18.0 ml/min	H <sub>2</sub> Production (mL/min)	H <sub>2</sub> Pressure (bar)	Raf Pressure (bar)	Raf Flow (mL/min)	NH <sub>3</sub> Flow (mL/min)
0	(RICH)	0	0	0	0	0
5	(sustained)	82.441	1.3	1.1		20.008
10		94.267	0.2	1.1		18.027
15		94.267	0.2	1.1		19.156
20		121.522	0.15	1.1		18.067
25		121.522	0.1	1.1		15.868
30		121.522	0.1	1.1		16.304
35		145.770	0.1	1.1		18.166
40		145.770	0.1	1.1		20.167
45		190.225	0.1	1.1		17.849
50		190.789	0.1	1.1		19.117
55		191.760	0.1	1.1		16.026
60		194.907	0.1	1.1		19.572
65		198.463	0.1	1.1		17.928
70		200.697	0.1	1.1		19.136
75		203.437	0.1	1.1		17.829
80		204.761	0.1	1.1		18.027
85		204.761	0.1	1.1		17.155
90		204.761	0.1	1.1		17.453
95		204.761	0.1	1.1		18.186
100		204.761	0.1	1.1		18.245
105		204.761	0.1	1.1		17.770
110		204.761	0.1	1.1		20.028
115		204.761	0.1	1.1		16.006
120		204.427	0.1	1.1		18.106

\*Raf Flow was obstructed by small amounts blue ammonia- nickel liquid formation. No reliable Raf Data collected.

## Appendix C

Table C1: Uncertainty propagation for experiment at 400.0°C, 5.0 bar, and  $t_{res}= 0.937$  s.

Parameter Name	Parameter Value +/- Uncertainty
NH <sub>3</sub> Flow Rate (kg/s)	$1.732 \times 10^{-9} \pm 4.918 \times 10^{-11}$
H <sub>2</sub> Production Rate (mL/min)	1.25 +/- 0.04424
Energy Ratio ( - )	$0.0245 \pm 7.013 \times 10^{-4}$
Exergy Ratio ( - )	$0.003622 \pm 1.037 \times 10^{-4}$
Energy Efficiency (%)	$0.05958 \pm 1.692 \times 10^{-3}$
Exergy Efficiency (%)	$0.09036 \pm 2.567 \times 10^{-3}$
Reaction Rate (kg/s)	$3.083 \times 10^{-10} \pm 8.754 \times 10^{-12}$
NH <sub>3</sub> Concentration (%)	$99.58 \pm 1.18 \times 10^{-2}$

Table C2: Uncertainty propagation for experiment at 400.0°C, 5.0 bar, and  $t_{res}= 1.874$  s.

Parameter Name	Parameter Value +/- Uncertainty
NH <sub>3</sub> Flow Rate (kg/s)	$1.467 \times 10^{-6} \pm 2.205 \times 10^{-8}$
H <sub>2</sub> Production Rate (mL/min)	2.43 +/- 0.1181
Energy Ratio ( - )	$0.0904 \pm 2.261 \times 10^{-3}$
Exergy Ratio ( - )	$0.01337 \pm 3.344 \times 10^{-4}$
Energy Efficiency (%)	$0.1245 \pm 2.495 \times 10^{-3}$
Exergy Efficiency (%)	$0.1992 \pm 4.009 \times 10^{-3}$
Reaction Rate (kg/s)	$5.996 \times 10^{-10} \pm 1.119 \times 10^{-11}$
NH <sub>3</sub> Concentration (%)	$98.38 \pm 3.24 \times 10^{-2}$

Table C3: Uncertainty propagation for experiment at 400.0°C, 5.0 bar, and  $t_{res}= 3.748$  s.

Parameter Name	Parameter Value +/- Uncertainty
NH <sub>3</sub> Flow Rate (kg/s)	$6.779 \times 10^{-7} \pm 2.831 \times 10^{-14}$
H <sub>2</sub> Production Rate (mL/min)	1.77 +/- 0.04425
Energy Ratio ( - )	$0.1428 \pm 2.012 \times 10^{-3}$
Exergy Ratio ( - )	$0.02112 \pm 2.975 \times 10^{-4}$
Energy Efficiency (%)	$0.09517 \pm 1.341 \times 10^{-3}$
Exergy Efficiency (%)	$0.1581 \pm 2.227 \times 10^{-3}$
Reaction Rate (kg/s)	$4.377 \times 10^{-10} \pm 6.166 \times 10^{-12}$
NH <sub>3</sub> Concentration (%)	$97.64 \pm 3.33 \times 10^{-2}$

Table C4: Uncertainty propagation for experiment at 500.0°C, 5.0 bar, and  $t_{res}= 3.748$  s.

Parameter Name	Parameter Value +/- Uncertainty
NH <sub>3</sub> Flow Rate (kg/s)	$6.779 \times 10^{-7} \pm 1.016 \times 10^{-8}$
H <sub>2</sub> Production Rate (mL/min)	24.46 +/- 0.4892
Energy Ratio ( - )	$1.929 \pm 4.824 \times 10^{-2}$
Exergy Ratio ( - )	$0.2912 \pm 7.28 \times 10^{-3}$
Energy Efficiency (%)	$1.312 \pm 2.626 \times 10^{-2}$
Exergy Efficiency (%)	$1.993 \pm 1.936 \times 10^{-3}$
Reaction Rate (kg/s)	$6.035 \times 10^{-9} \pm 1.207 \times 10^{-10}$
NH <sub>3</sub> Concentration (%)	$67.39 \pm 0.6523$

Table C5: Uncertainty propagation for experiment at 500.0°C, 5.0 bar, and  $t_{res}= 1.874$  s.

Parameter Name	Parameter Value +/- Uncertainty
NH <sub>3</sub> Flow Rate (kg/s)	$1.443 \times 10^{-6} \text{ +/- } 2.165 \times 10^{-8}$
H <sub>2</sub> Production Rate (mL/min)	33.0 +/- 0.66
Energy Ratio ( - )	$1.223 \text{ +/- } 3.057 \times 10^{-2}$
Exergy Ratio ( - )	$0.1845 \text{ +/- } 4.613 \times 10^{-3}$
Energy Efficiency (%)	$1.693 \text{ +/- } 3.393 \times 10^{-2}$
Exergy Efficiency (%)	$2.495 \text{ +/- } 5.016 \times 10^{-2}$
Reaction Rate (kg/s)	$8.142 \times 10^{-9} \text{ +/- } 1.628 \times 10^{-10}$
NH <sub>3</sub> Concentration (%)	78.0 +/- 0.44

Table C6: Uncertainty propagation for experiment at 500.0°C, 5.0 bar, and  $t_{res}= 0.937$  s.

Parameter Name	Parameter Value +/- Uncertainty
NH <sub>3</sub> Flow Rate (kg/s)	$2.886 \times 10^{-6} \text{ +/- } 4.329 \times 10^{-8}$
H <sub>2</sub> Production Rate (mL/min)	16.5 +/- 0.33
Energy Ratio ( - )	$0.3057 \text{ +/- } 7.642 \times 10^{-3}$
Exergy Ratio ( - )	$0.04613 \text{ +/- } 1.153 \times 10^{-3}$
Energy Efficiency (%)	$0.7825 \text{ +/- } 1.575 \times 10^{-2}$
Exergy Efficiency (%)	$1.099 \text{ +/- } 2.233 \times 10^{-2}$
Reaction Rate (kg/s)	$4.071 \times 10^{-9} \text{ +/- } 8.142 \times 10^{-11}$
NH <sub>3</sub> Concentration (%)	94.5.0 +/- 0.11

Table C7: Uncertainty propagation for experiment at 400.0°C, 10.0 bar, and  $t_{res} = 3.529$  s.

Parameter Name	Parameter Value +/- Uncertainty
NH <sub>3</sub> Flow Rate (kg/s)	$1.309 \times 10^{-6} \pm 1.964 \times 10^{-8}$
H <sub>2</sub> Production Rate (mL/min)	39.86 +/- 0.7972
Energy Ratio ( - )	$1.662 \pm 4.156 \times 10^{-2}$
Exergy Ratio ( - )	$0.2221 \pm 4.433 \times 10^{-3}$
Energy Efficiency (%)	$2.061 \pm 4.13 \times 10^{-2}$
Exergy Efficiency (%)	$3.32 \pm 6.675 \times 10^{-2}$
Reaction Rate (kg/s)	$9.386 \times 10^{-9} \pm 1.967 \times 10^{-10}$
NH <sub>3</sub> Concentration (%)	73.42 +/- 0.5315

Table C8: Uncertainty propagation for experiment at 400.0°C, 10.0 bar, and  $t_{res} = 1.764$  s.

Parameter Name	Parameter Value +/- Uncertainty
NH <sub>3</sub> Flow Rate (kg/s)	$2.657 \times 10^{-6} \pm 3.986 \times 10^{-8}$
H <sub>2</sub> Production Rate (mL/min)	28.82 +/- 0.5764
Energy Ratio ( - )	$0.592 \pm 1.48 \times 10^{-2}$
Exergy Ratio ( - )	$8.723 \times 10^{-2} \pm 2.181 \times 10^{-3}$
Energy Efficiency (%)	$1.383 \pm 2.782 \times 10^{-2}$
Exergy Efficiency (%)	$2.106 \pm 4.281 \times 10^{-2}$
Reaction Rate (kg/s)	$7.11 \times 10^{-9} \pm 1.422 \times 10^{-10}$
NH <sub>3</sub> Concentration (%)	90.39 +/- 0.1921

Table C9: Uncertainty propagation for experiment at 500.0°C, 10.0 bar, and  $t_{res}= 3.529$  s.

Parameter Name	Parameter Value +/- Uncertainty
NH <sub>3</sub> Flow Rate (kg/s)	$1.322 \times 10^{-6} \pm 1.983 \times 10^{-8}$
H <sub>2</sub> Production Rate (mL/min)	145.8 +/- 2.916
Energy Ratio ( - )	5.986 +/- 0.1474
Exergy Ratio ( - )	$0.8898 \pm 2.225 \times 10^{-2}$
Energy Efficiency (%)	7.532 +/- 0.1509
Exergy Efficiency (%)	11.15 +/- 0.224
Reaction Rate (kg/s)	$3.597 \times 10^{-8} \pm 7.195 \times 10^{-11}$
NH <sub>3</sub> Concentration (%)	2.821 +/- 1.944

Table C10: Uncertainty propagation for experiment at 500.0°C, 10.0 bar, and  $t_{res}= 1.764$  s.

Parameter Name	Parameter Value +/- Uncertainty
NH <sub>3</sub> Flow Rate (kg/s)	$2.77 \times 10^{-6} \pm 4.155 \times 10^{-8}$
H <sub>2</sub> Production Rate (mL/min)	105.2 +/- 2.104
Energy Ratio ( - )	2.032 +/- 0.0508
Exergy Ratio ( - )	$0.3066 \pm 7.666 \times 10^{-3}$
Energy Efficiency (%)	5.021 +/- 0.101
Exergy Efficiency (%)	7.077 +/- 0.1437
Reaction Rate (kg/s)	$2.596 \times 10^{-8} \pm 5.194 \times 10^{-10}$
NH <sub>3</sub> Concentration (%)	64.93 +/- 0.7013

Table C11: Uncertainty propagation for experiment at 400.0°C, 20.0 bar, and  $t_{res}= 3.965$  s.

Parameter Name	Parameter Value +/- Uncertainty
NH <sub>3</sub> Flow Rate (kg/s)	$2.387 \times 10^{-6} \pm 3.581 \times 10^{-8}$
H <sub>2</sub> Production Rate (mL/min)	76.92 +/- 1.583
Energy Ratio ( - )	$1.759 \pm 5.08 \times 10^{-2}$
Exergy Ratio ( - )	$0.2551 \pm 6.377 \times 10^{-3}$
Energy Efficiency (%)	$3.746 \pm 7.526 \times 10^{-2}$
Exergy Efficiency (%)	5.743 +/- 0.1165
Reaction Rate (kg/s)	$1.898 \times 10^{-8} \pm 3.795 \times 10^{-10}$
NH <sub>3</sub> Concentration (%)	74.36 +/- 1.056

Table C12: Uncertainty propagation for experiment at 400.0°C, 20.0 bar, and  $t_{res}= 1.983$  s.

Parameter Name	Parameter Value +/- Uncertainty
NH <sub>3</sub> Flow Rate (kg/s)	$4.695 \times 10^{-6} \pm 7.043 \times 10^{-8}$
H <sub>2</sub> Production Rate (mL/min)	55.54 +/- 1.111
Energy Ratio ( - )	$0.6456 \pm 1.614 \times 10^{-2}$
Exergy Ratio ( - )	$9.513 \times 10^{-2} \pm 2.378 \times 10^{-2}$
Energy Efficiency (%)	$2.405 \pm 4.878 \times 10^{-2}$
Exergy Efficiency (%)	$3.504 \pm 7.059 \times 10^{-2}$
Reaction Rate (kg/s)	$1.37 \times 10^{-8} \pm 2.74 \times 10^{-10}$
NH <sub>3</sub> Concentration (%)	87.66 +/- 0.3073

Table C13: Uncertainty propagation for experiment at 500.0°C, 20.0 bar, and  $t_{res} = 3.965$  s.

Parameter Name	Parameter Value +/- Uncertainty
NH <sub>3</sub> Flow Rate (kg/s)	$2.391 \times 10^{-6} \pm 7.954 \times 10^{-8}$
H <sub>2</sub> Production Rate (mL/min)	286.92 +/- 5.738
Energy Ratio ( - )	6.416 +/- 0.1604
Exergy Ratio ( - )	$0.9695 \pm 2.374 \times 10^{-2}$
Energy Efficiency (%)	13.98 +/- 0.2807
Exergy Efficiency (%)	19.91 +/- 0.4018
Reaction Rate (kg/s)	$7.079 \times 10^{-8} \pm 1.415 \times 10^{-9}$
NH <sub>3</sub> Concentration (%)	4.359 +/- 1.913

Table C14: Uncertainty propagation for experiment at 500.0°C, 20.0 bar, and  $t_{res} = 1.983$  s.

Parameter Name	Parameter Value +/- Uncertainty
NH <sub>3</sub> Flow Rate (kg/s)	$4.737 \times 10^{-6} \pm 5.668 \times 10^{-9}$
H <sub>2</sub> Production Rate (mL/min)	204.4 +/- 4.088
Energy Ratio ( - )	2.308 +/- 0.7715
Exergy Ratio ( - )	0.3415 +/- 0.1142
Energy Efficiency (%)	8.834 +/- 2.954
Exergy Efficiency (%)	11.73 +/- 3.923
Reaction Rate (kg/s)	$5.044 \times 10^{-8} \pm 1.686 \times 10^{-8}$
NH <sub>3</sub> Concentration (%)	54.4 +/- 0.9084